nature methods

Article

https://doi.org/10.1038/s41592-025-02843-8

Kilohertz volumetric imaging of in vivo dynamics using squeezed light field microscopy

Received: 14 November 2024

Accepted: 21 August 2025

Published online: 23 September 2025

Check for updates

Zhaoqiang Wang[1,13], Ruixuan Zhao[1,13], Daniel A. Wagenaar[2], Diego Espino[3], Liron Sheintuch[3], Ohr Benshlomo[1], Wenjun Kang[4], Enbo Zhu[5], Calvin K. Lee[1,6,7,8], William C. Schmidt[1,6,7,8], Aryan Pammar[1], Jing Wang[5], Gerard C. L. Wong[1,6,7,8], Rongguang Liang[4], Peyman Golshani[3,9,10,11,12], Tzung K. Hsiai[5,9] & Liang Gao[1]

Volumetric functional imaging of transient cellular signaling and motion dynamics is often limited by hardware bandwidth and the scarcity of photons under short exposures. To overcome these challenges, we introduce squeezed light field microscopy (SLIM), a computational imaging approach that rapidly captures high-resolution three-dimensional light signals using only a single, low-format camera sensor. SLIM records over 1,000 volumes per second across a 550-µm diameter field of view and 300-µm depth, achieving 3.6-µm lateral and 6-µm axial resolution. Here we demonstrate its utility in blood cell velocimetry within the embryonic zebrafish brain and in freely moving tails undergoing high-frequency swings. Millisecond-scale temporal resolution further enables precise voltage imaging of neural membrane potentials in the leech ganglion and hippocampus of behaving mice. Together, these results establish SLIM as a versatile and robust tool for high-speed volumetric microscopy across diverse biological systems.

High-speed fluorescence microscopy has been playing an indispensable role in revealing the dynamic interplay and functionality among cells in their native environment. With continuous improvements in fluorescent markers, many transient biological processes, such as blood flow[1] and neural action potentials[2–4], become trackable and, thus, demand microscopy with an ever higher spatiotemporal resolution. Traditional three-dimensional (3D) imaging tools, such as confocal microscopy, light-sheet microscopy and two-photon microscopy, heavily rely on scanning to acquire a volumetric image. Despite advancement in beam shaping[5,6], remote refocusing mechanisms[7], detector array[8,9] and detection geometry[10], there persists an inherent trade-off between temporal resolution, the 3D field of view (FOV) and spatial resolution. This constraint marks a notable challenge to obtain optimal performance across a large 3D FOV for robust ultra-fast detection exceeding kilohertz.

Computational imaging mitigates this trade-off by encoding high-dimensional information, such as depth[11], time[12] and spectra[13],

[1]Department of Bioengineering, Henry Samueli School of Engineering and Applied Science, University of California, Los Angeles, Los Angeles, CA, USA. [2]Division of Biology and Biological Engineering, Tianqiao and Chrissy Chen Institute for Neuroscience, California Institute of Technology, Pasadena, CA, USA. [3]Department of Neurology, David Geffen School of Medicine, University of California, Los Angeles, Los Angeles, CA, USA. [4]Wyant College of Optical Science, University of Arizona, Tucson, AZ, USA. [5]Division of Cardiology, Department of Medicine, David Geffen School of Medicine, University of California, Los Angeles, Los Angeles, CA, USA. [6]Department of Chemistry and Biochemistry, University of California, Los Angeles, Los Angeles, CA, USA. [7]California NanoSystems Institute, University of California, Los Angeles, Los Angeles, CA, USA. [8]Department of Microbiology, Immunology, and Molecular Genetics, University of California, Los Angeles, Los Angeles, CA, USA. [9]Greater Los Angeles VA Medical Center, Los Angeles, CA, USA. [10]Semel Institute for Neuroscience and Human Behavior, University of California, Los Angeles, Los Angeles, CA, USA. [11]Integrative Center for Learning and Memory, University of California, Los Angeles, Los Angeles, CA, USA. [12]Intellectual and Developmental Disability Research Center, University of California, Los Angeles, Los Angeles, CA, USA. [13]These authors contributed equally: Zhaoqiang Wang, Ruixuan Zhao. e-mail: gaol@ucla.edu

into two-dimensional (2D) multiplexed camera measurements. Among these techniques, light field microscopy (LFM) excels in various biological applications, including observation of neural activity in freely moving animals[14–16] and visualization of hemodynamics in the brain[17] and heart[18–20]. By simultaneously collecting the spatial and angular information of light rays, LFM enables volumetric reconstruction post hoc from snapshot measurements. Moreover, when combined with advanced deep-learning-based reconstruction algorithms[19–22], LFM can achieve high-resolution imaging at subcellular spatial resolutions.

Without scanning, the sensor bandwidth becomes the primary bottleneck for LFM 3D imaging speed. While scientific complementary metal-oxide semiconductor (sCMOS) sensors typically offer a full frame rate lower than 100 Hz, increasing the imaging speed can be achieved by reading out only selected low-format regions of interest (ROI). However, this approach comes at the cost of sacrificing either the spatial and/or angular components associated with the FOV and axial resolution.

The integration of ultra-high-speed cameras[7,10,23] and event cameras[24] holds promise for providing higher bandwidths to LFM. However, their current limitations in sensitivity and noise performance present challenges, especially for photon-starved applications such as imaging genetically encoded voltage indicators (GEVIs) (see Supplementary Table 1 for a list of camera models and their performance)[7]. Although event camera-based light field imaging has been demonstrated at kilohertz rates, the binary nature of event camera outputs restricts its ability to accurately quantify analog signals, such as subthreshold voltage oscillations. On the other hand, the compressibility of four-dimensional (4D) (two spatial dimensions plus two angular dimensions) light fields has been leveraged for compressive detection. Coded masks[25–27] and random diffusers[28–31] are used to modulate and integrate the spatio-angular components originally recorded by distinct pixels. Sparse nonlocal measurements can also be used across different angular views to acquire light fields with sensors of arbitrary formats[32–34]. Nevertheless, as compressive imaging relies on sparsity prior and optimization algorithms for signal recovery from the sub-Nyquist measurement, the performance is prone to degradation in challenging scenarios. These methods are primarily validated on photographic scenes and biological samples with relatively long exposure times. Their robustness and effectiveness in kilohertz microscopy with extremely low photon budget such as voltage imaging remain elusive.

To address the unmet need for high-speed light field imaging, we present herein squeezed light field microscopy (SLIM), which allows the capture of 3D fluorescent signals at kilohertz volume rates in a highly data-efficient manner. SLIM operates by acquiring an array of rotated 2D subaperture images. An anamorphic relay system applies anisotropic scaling, effectively 'squeezing' the image along one spatial axis. This allows the camera sensor to detect the light field using only a low-format letterbox-shaped ROI. Leveraging the row-by-row read-out architecture of CMOS sensors, SLIM achieves a more than fivefold increase in acquisition rates compared to traditional LFM. Each squeezed subaperture image complements the others, facilitating high-fidelity, robust 3D reconstruction from compressed measurement. By calculating the product of space-bandwidth product and volume rate, SLIM measures ~7.3 gigavoxels per second, placing it among the ultra-fast 3D fluorescent microscopes reported in literature (Supplementary Table 2).

We demonstrated SLIM by capturing the flowing red blood cells (RBCs) in freely swinging tails of embryonic zebrafish at 1,000 volumes per second (vps), ex vivo voltage imaging in dissected leech ganglia at 800 vps and in vivo voltage imaging in the hippocampus of behaving mice at 800 vps. SLIM enables tracking high-speed cellular motion across a 550-μm FOV within a 300-μm depth range. It allows detection of millisecond membrane action potentials and subthreshold oscillations in a 3D space over extended time periods in awake, free-behaving animals. Furthermore, we showcased that the high frame rate of SLIM can be exploited to enhance the axial resolution when combined with multi-layer scanning light-sheet microscopy. This allows for imaging densely labeled structures, previously challenging with LFM, such as contracting myocardium in a zebrafish, at 4,800 frames per second (fps), leading to a volume rate of 300 vps.

Results

Principle and design of SLIM

In a typical SLIM camera (Fig. 1a), the input scene is imaged by a combined system consisting of an array of dove prisms and lenslets (Fig. 1a(i) and Supplementary Fig. 1). Each dove prism within the array is rotated at a distinct angle relative to its optical axis. This arrangement gives rise to an array of perspective images, each rotated at twice the angle of its corresponding dove prism's rotation, all converging at an intermediate image plane situated behind the lenslets. Subsequently, these rotated perspective images are further processed through an anamorphic relay system consisting of two cylindrical doublets with orthogonal optical axes (Fig. 1a and Supplementary Fig. 2). This relay system imparts anisotropic scaling to the image array, where the images experience de-magnification (×0.2) along one spatial axis while preserving the original magnification along the orthogonal direction. Finally, the rescaled image array is acquired by a 2D camera, where we read out only pixel rows that receive light signals (referred to as active read-out ROI in Fig. 1a).

One of the key advantages of using squeezed optical mapping is the improved read-out speed. CMOS sensors are equipped with parallel analog-to-digital converters for each column of pixels, ensuring consistent frame rates regardless of the number of pixel columns being read out. The frame rate is, therefore, solely determined by and inversely proportional to the number of pixel rows being read out[35]. For example, on the Kinetix sCMOS developed by Teledyne, using an ROI of 200 × 3,200 pixels allows SLIM to capture a 19 subaperture image array at 1,326 fps and 7,476 fps in 16-bit and 8-bit mode, respectively. In contrast, the full-frame mode achieves frame rates of only 83 fps (16-bit) and 500 fps (8-bit).

The forward model of SLIM is illustrated in Fig. 1b. Similar to Fourier LFM (FLFM)[15,36–38], SLIM can be conceptualized as a tomographic system, where each subaperture image is essentially a parallel projection of a 3D volume along a line of sight at the subaperture's view angle[39,40]. However, unlike FLFM, where these subaperture images are directly captured by a 2D camera, SLIM applies in-plane rotation and vertical scaling operations to these images before recording.

In the 3D spatial frequency space, the Fourier spectrum of a SLIM subaperture image manifests as a 2D elliptical slice (Fourier slice theorem; Supplementary Note 1). The short axis of this ellipse corresponds to the low-resolution sampling along the squeezing direction. By using an array of subaperture images rotated at complementary angles, SLIM fills in the missing high-frequency information. This process results in a synthesized power spectrum with a bandwidth that approximates that of the original unsqueezed FLFM (Fig. 1c). In addition, the rotation angles of subaperture images are carefully crafted to maximize the horizontal projections of their 3D point spread functions (PSFs) (Supplementary Fig. 3). In other words, when imaging a 3D object, the subaperture images of SLIM exhibit lateral disparity shift due to their view angle difference. While the entire set of rotation angles are sampled uniformly from 0 to 180°, we optimize the angle assignment to each subaperture image to align its disparity shift with the unsqueezed spatial axis (that is, camera pixel row direction), thereby maximizing the samplings of disparity and consequently enhancing the axial resolution (Supplementary Note 1). Using this approach, some subapertures may not receive their optimal angles. We prioritized the subapertures in the outer region, as they display larger disparity shifts than inner ones and contribute more substantially to the axial resolution. This forward model can be further extended to wave optics by using a sum of 2D convolutions between the sample sliced at each depth and the

https://doi.org/10.1038/s41592-025-02843-8

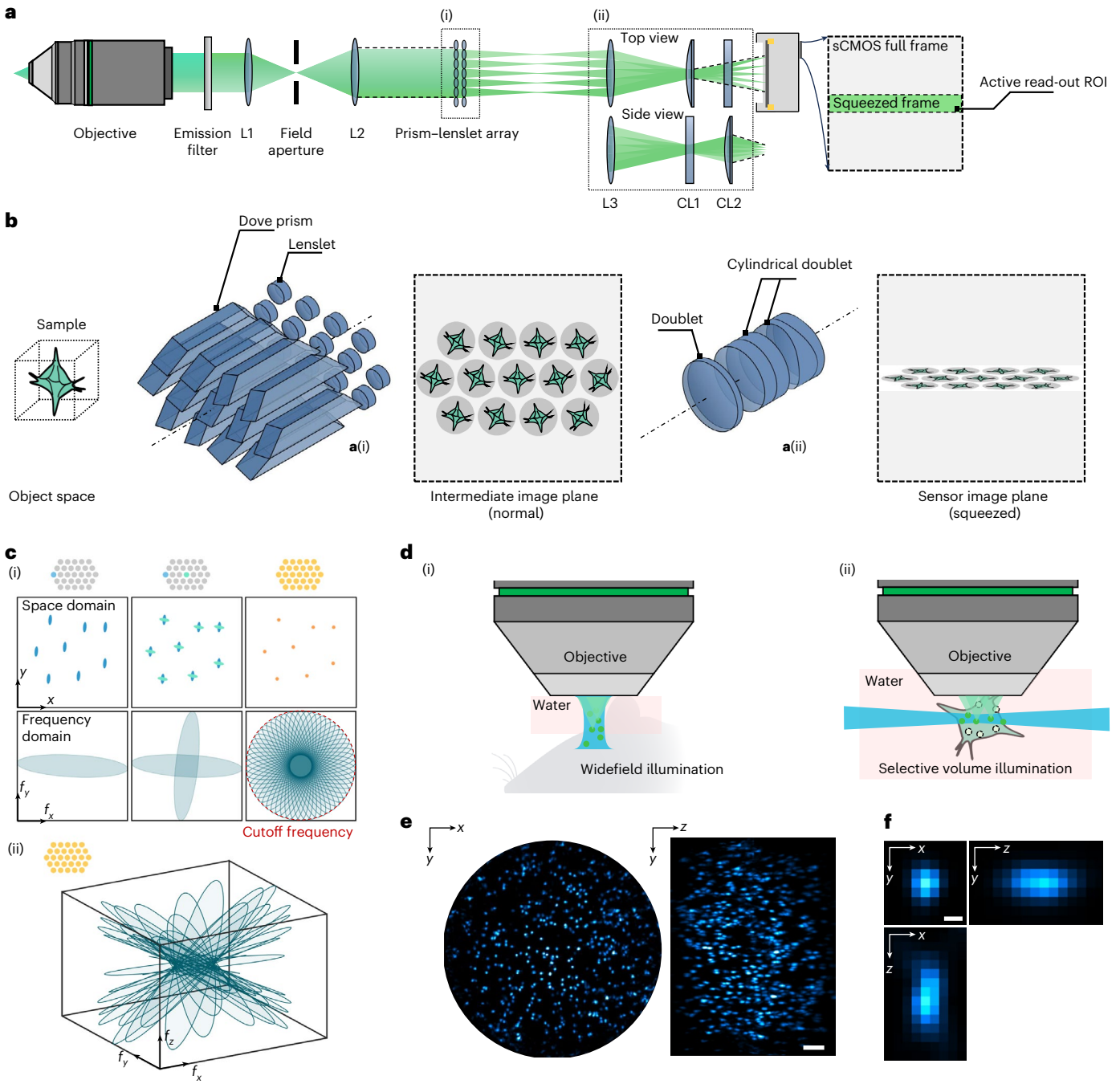

Fig. 1 | Principle of SLIM. a, Schematic of SLIM detection system. L1–L3, achromatic doublet. CL1–CL2, achromatic cylindrical doublet. SLIM records light field at kilohertz frame rates by using a reduced active read-out ROI on the camera. **b**, The optical transformation in SLIM comprises image rotation and squeezing, performed by a dove prism and lenslet array (**a**(i)) and a customized anamorphic relay (**a**(ii)). **c**, (i) Each subaperture, after reversing the squeezing and rotation, gives an image with anisotropic spatial resolution but complementary to others. By merging different subaperture images, SLIM estimates the original features. Three columns show how one, two and all subaperture images reconstruct the final image and spectrum. The red dotted circle denotes the lateral cutoff frequency. (ii) 3D illustration of transfer functions of SLIM by analyzing all subaperture images as geometrical projections. Each gives an elliptical slice in the 3D frequency space, depending on its rotation angle and subaperture location. **d**, SLIM is compatible with different illumination modes. We demonstrated widefield illumination (i) for behaving mice imaging, and selective volume illumination (ii) for zebrafish and leech ganglion imaging. **e**, 3D MIPs of fluorescent beads. Scale bar, 50 µm. **f**, Cross-sections of single bead showing representative PSFs. Scale bar, 3 µm.

corresponding subaperture PSF[40]. Through an iterative deconvolution algorithm, SLIM reconstructs the 3D fluorescence distribution by fusing all subaperture images.

We built two setups to demonstrate SLIM's applications across a wide range of high-speed biological processes (Fig. 1d and Supplementary Figs. 4 and 5). A widefield epi-illumination setup is used for mouse imaging through cranial windows, while a selective volume illumination setup is designed for small animals such as zebrafish larvae and dissected leech ganglia, where the target of interest can be accessed via side illumination. Selective illumination, implemented with either a scanning light sheet or a slit-confined light-emitting diode (LED) (Supplementary Fig. 4a), suppresses

https://doi.org/10.1038/s41592-025-02843-8

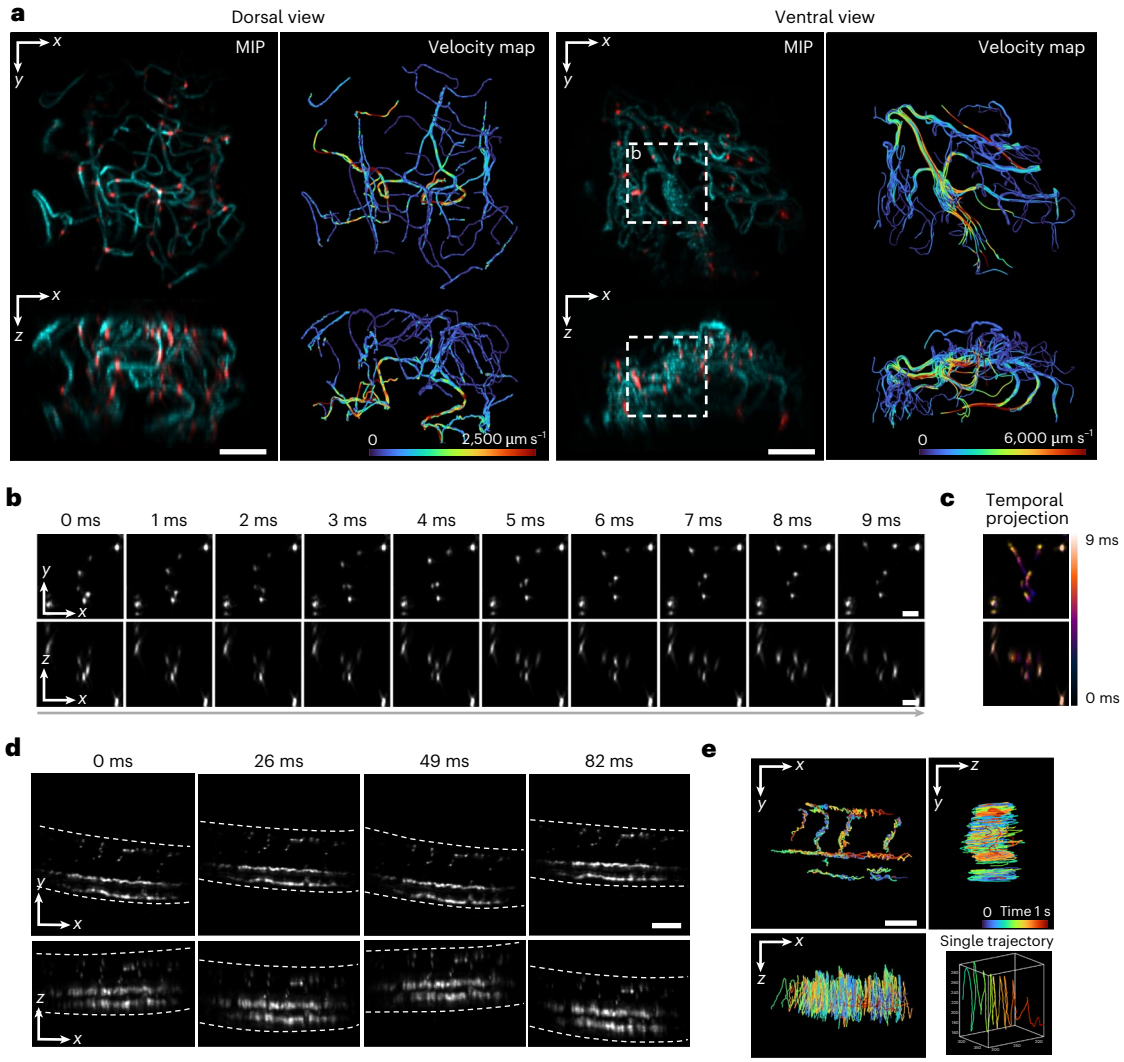

Fig. 2 | 3D imaging of hemodynamics in the embryonic zebrafish brain and tail at 1,000 vps. a, MIPs of flowing blood cells at representative time points (red) and vascular network obtained by combining frames over time (cyan). The velocity maps show overlaid RBC trajectories color-coded by their instantaneous velocity. Two views, the dorsal view and ventral view, are two datasets taken with differently oriented embryos. Scale bars, 100 μm. **b**, Zoom-in time-lapse of the region labeled by the white dashed box in **a**. Scale bars, 30 μm. **c**, Temporal projection color-coded by the time visualizes the motion blur with a lower imaging speed. **d**, MIPs of a free-moving fish tail. Scale bar, 100 um. **e**, RBC trajectories from **d** are color-coded by time. The coordinate system has been rotated so that the *x*–*y* plane shows the RBC movement perpendicular to the tail swing direction. The single trajectory on the bottom right exhibits the compound motion of a single RBC during fish swimming. Scale bar, 100 μm.

fluorescence outside the imaging volume, particularly in scattering tissues (Supplementary Figs. 6 and 7). The LED is preferred for applications requiring high power stability.

Figure 1e,f shows the 3D reconstruction of fluorescent beads of subdiffraction size imaged by SLIM. At a magnification of ×3.6, the imaging volume spans a 3D space of ⌀550 μm × 300 μm (⌀ denotes diameter) with a spatial resolution of 3.6 μm laterally and 6.0 μm axially (Supplementary Fig. 3). SLIM inherits the lenslet array-based optical design of FLFM for snapshot 3D imaging and provides a highly efficient data acquisition strategy for scientific camera sensors. SLIM can record and reconstruct 7.3×10^9 effective voxels per second, making it a powerful optical compression method that enables kilohertz-rate volumetric imaging within the constrained bandwidth of conventional camera sensors.

Imaging of flowing RBCs in an embryonic zebrafish

Experimental characterization of blood flow in living organisms provides valuable insights into local metabolic activity, vascular development and pathological conditions. Using fluorescently labeled blood cells, various imaging methods have been demonstrated in single-cell velocimetry, such as in the larval zebrafish heart[10], tail[41] and mouse brain[1,17]. However, these methods are often limited to 2D imaging or restricted by a limited volumetric frame rate, which hinders the detection of fast flow and necessitates sedation of the animal to reduce motion artifacts. Here, we show that SLIM can be used to capture fast-circulating RBCs in a zebrafish at a kilohertz volumetric rate, both with and without sedation.

We imaged transgenic zebrafish embryos expressing DsRed in RBCs at 3 days postfertilization. We excited the zebrafish brain using light-sheet-synthesized volumetric illumination and recorded fluorescence using SLIM with 19 subaperture images at 1,000 frames per second. The reconstruction reveals the 3D distribution of RBCs and allows for cell tracking over time (Supplementary Fig. 8). Figure 2a shows two separate recordings from the dorsal and ventral view, each visualizing RBCs at representative time points (red) and the vasculature network by maximum intensity projection (MIP) throughout all frames (cyan). The flowing velocity is pulsatile temporally and varies spatially in the aorta and vein (Supplementary Videos 1 and 2). The tracking reveals the

velocity distribution in 3D and highlights vessels with a high-speed flow of up to 6 mm s^{-1} (Fig. 2a). SLIM's kilohertz imaging seizes the transient motion at a millisecond time scale (Fig. 2b), effectively eliminating the motion blur and enabling robust cell tracking that would be compromised at lower imaging rates (Fig. 2c).

We further demonstrated the speed advantage by imaging the free-moving tail of a zebrafish without sedation. The embryo was mounted on a cover glass with its head restrained using agarose while allowing the tail to move freely in the water. SLIM captured high-frequency tail swings without motion blur (Fig. 2d and Supplementary Video 3), maintaining its capability to track individual RBCs and revealing the compound movement composed of oscillation perpendicular to the tail plane and forward progression along the vessels (Fig. 2e). By combining with closed-loop tracking and a translational stage[15], SLIM's high-speed volumetric imaging holds promise for studying hemodynamics under natural conditions during locomotor behavior.

Optical recording of membrane action potentials

The development of voltage imaging has enabled neuroscientists to examine neural dynamics with a high spatiotemporal resolution. However, it has long been a challenge to capture voltage signals in vivo across a large volume due to the extremely fast transients and low signal-to-noise ratio (SNR). With its millisecond temporal resolution, SLIM can precisely detect spike timings across a large 3D neural network, opening avenues for mapping the intricate interaction of neuronal components and elucidating the mechanisms underlying sensory processing and behavioral generation.

As a demonstration, we loaded the voltage-sensitive dye FluoVolt to a dissected ganglion from a medicinal leech[42]. Using SLIM, we recorded the fluorescent signals with 29 subaperture images at 800 Hz under the illumination of an ultra-low-noise LED. Concurrently, we introduced an intracellular microelectrode for simultaneous electrophysiological stimulation and recording (Fig. 3a). Timing and waveforms (Fig. 3b) of neuronal action potentials are adequately sampled from the reconstructed 3D image sequence (Fig. 3c and Supplementary Video 4). We further processed the data by correcting motion drift, manually choosing an area of interest on each cell, and averaging pixels from the corresponding cell membrane (Supplementary Figs. 9 and 10). The resultant time-lapse fluorescence intensities at selected neurons are shown in Fig. 3d. SLIM measurements match the electrophysiological record in quantitative detail (Supplementary Fig. 11), including the reduction of spike amplitude under strong depolarizing current injection.

In a separate experiment, we used a train of electrical pulses to stimulate a dorsal posterior nerve root of midbody ganglion 13 (M13), which mimics a touch to the body wall in an intact leech to elicit fictive swimming[43,44]. Using the SLIM system, we imaged the selected midbody ganglion 10 (M10) (Fig. 3e,f) from the dorsal side at an 800 Hz volume rate under the same illumination conditions as the previous demonstration. The nerve signal was simultaneously recorded through the suction microelectrode, which showed rhythmic dorsal motor neuron bursts characteristic of swimming (Fig. 3h). After manually selecting and averaging a 3D ROI for each cell, the optical fluorescence signals at selected motor neurons (dorsal and ventral inhibitory and excitatory motor neurons DI-1, DE-3 and VE-4) and pressure sensitive cell (P2) are shown in Fig. 3h. The rhythmic activity characteristic of swimming (1 Hz to 1.5 Hz) was clearly observed in all motor neurons, consistent with previous work[42]. To characterize how cells participated in generating the swim rhythm, we calculated the magnitude and phase of coherence for each cell in the swimming oscillation band (Fig. 3g,i) with respect to the extracellular recording. SLIM measurement matches well with oscillatory behavior of neurons, including the overall coherence phase distribution of all cells in dorsal side and four pairs of specific motor neurons, DI-1, DE-3, VI-2 and VE-4, are very regular in their location and indeed overlapped in the measured and predicted phase maps.

Voltage imaging from the hippocampus of behaving mice

We examined the performance of the SLIM system in awake, behaving mice. We monitored neuronal activity in the CA1 of the hippocampus through an implanted cranial window in mice expressing the GEVI pAce[45]. Mice were imaged continuously at 800 Hz for three minutes on a treadmill setup that used an optical rotary encoder to track movement (Fig. 4a). Conventional widefield microscopes suffer from a shallow depth of focus and have difficulty imaging axially distributed neuron population (Fig. 4b). In contrast, SLIM provides volumetric mapping of signals (Supplementary Fig. 12), allowing for simultaneous optical measurement of neurons at different depths (Extended Data Fig. 1). After image reconstruction and motion correction, we extracted membrane-potential traces from multiple neuronal sources exhibiting strong speed-related action potential modulation across the image volume (Fig. 4c). We calculated the relative fluorescence change over the 3-minute recording, both in SNR (Fig. 4d and Supplementary Fig. 13) and in $\Delta F/F_0$ (Fig. 4e), where SLIM's millisecond temporal resolution provided sufficient sampling on the rising and falling slopes of transient spikes (Supplementary Fig. 14). Due to photobleaching (Supplementary Fig. 15), the amplitude of the spike waveform exhibited a gradual decay, but the SNR maintained around five across the entire recording (Fig. 4e). SLIM also detected subtle subthreshold membrane-potential oscillations (Fig. 4d and Extended Data Fig. 2). The observed signals predominantly show prominent frequency components in the 4–10 Hz band, likely originating from theta oscillations commonly found in the hippocampus[46–48] (Fig. 4f and Extended Data Fig. 2). The examination over the inactive neurons and

Fig. 3 | 3D imaging of membrane action potentials and fictive swimming oscillation in medicinal leech ganglia at 800 vps. a, Brightfield snapshot of leech ganglion. Microelectrode is denoted by a dashed circle, which allows for simultaneous stimulation (stim.) and electrophysiological (ephys.) recording. **b**, Average spike waveform. The yellow area marks the standard deviation of waveforms. Orange dots represent temporally sampling points, with an interval of 1.25 ms. **c**, MIP of SLIM reconstruction for voltage dye fluorescent signals. Scale bar, 50 µm. **d**, Recording of stimulation current, electrophysiological read-out and optical measurements of ganglion cells: the impaled cell (top), its contralateral partner that is electrically coupled to it (middle) and an unconnected cell (bottom). Rz indicates Retzius cell and AP indicates anterior pagoda cell. Gray boxes represent the time window when stimulation is injected. A deeper color represents larger stimulation. Spikes are detected and marked as black dots above the traces. (i),(ii) Zoom-ins of signal segments labeled by red and blue lines. **e**, A schematic of the isolated leech nerve cord, consisting of the anterior brain, midbody ganglia (circles) and the posterior brain. The voltage-sensitive dye components were applied to a midbody ganglion (M10). The brightfield reference image of selected ganglion is shown on the right. **f**, x–y cross-section of SLIM reconstruction for voltage dye fluorescent signals of fictive swimming behavior. Scale bar, 50 µm. **g**, Coherence of the optically recorded signals from all cells on the dorsal surface of the ganglion with the swim rhythm. Cells used in **h** are marked. Scale bar, 120 µm. **h**, Selected electrophysiological and voltage-sensitive dye traces of motor neurons during fictive swimming are presented. Top row: extracellular recording from a posterior-segment nerve root; red trace shows the filtered envelope of the extracellular signal. Other rows: voltage-sensitive dye signals from the dorsal surface captured the activity of dorsal and ventral inhibitory and excitatory motor neurons, specifically DI-1, DE-3, VE-4 and pressure sensitive cell P. Blue box visualizes the synchrony of the subthreshold oscillations among neurons. **i**, The polar plot illustrates the coherence between each optical recording and the extracellular recording in the frequency range of 0.8 Hz to 1.1 Hz. The distance from the center represents the coherence magnitude, while the angle indicates the coherence phase. Error bars show confidence intervals, calculated using the multitaper estimate method.

https://doi.org/10.1038/s41592-025-02843-8

background reveals the absence of spikes and subthreshold oscillations, further confirming the fidelity of observed signals. By correlating the time-dependent firing rate of each neuron with locomotion speed, we found that most neurons were positively modulated by locomotion speed (Fig. 4g and Supplementary Fig. 16), consistent with the previous finding[49]. In addition, SLIM's compressed measurement offers an advantage over alternative methods, providing highly efficient data bandwidth (Fig. 4h) and making it more accessible for long-term 3D

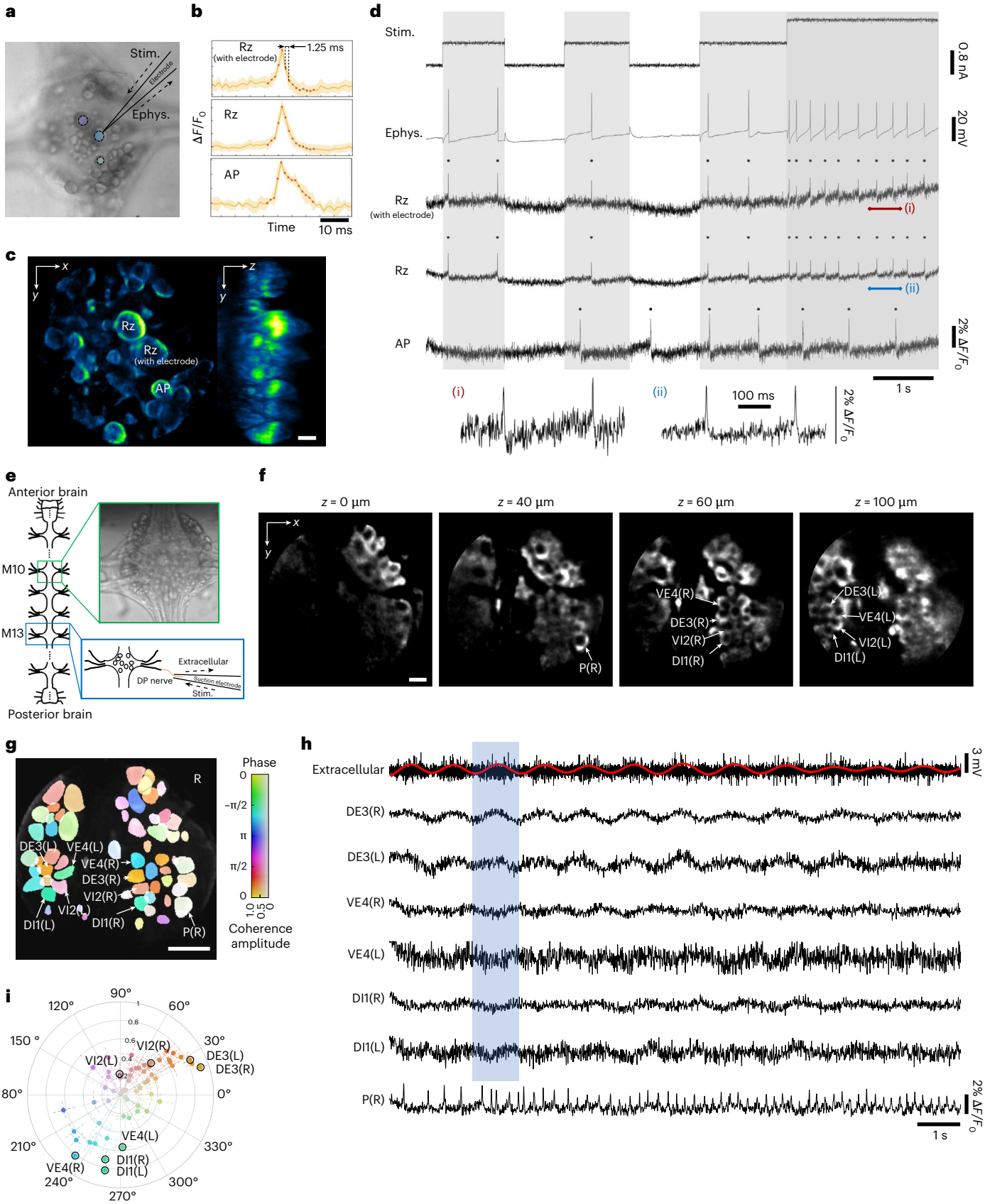

https://doi.org/10.1038/s41592-025-02843-8

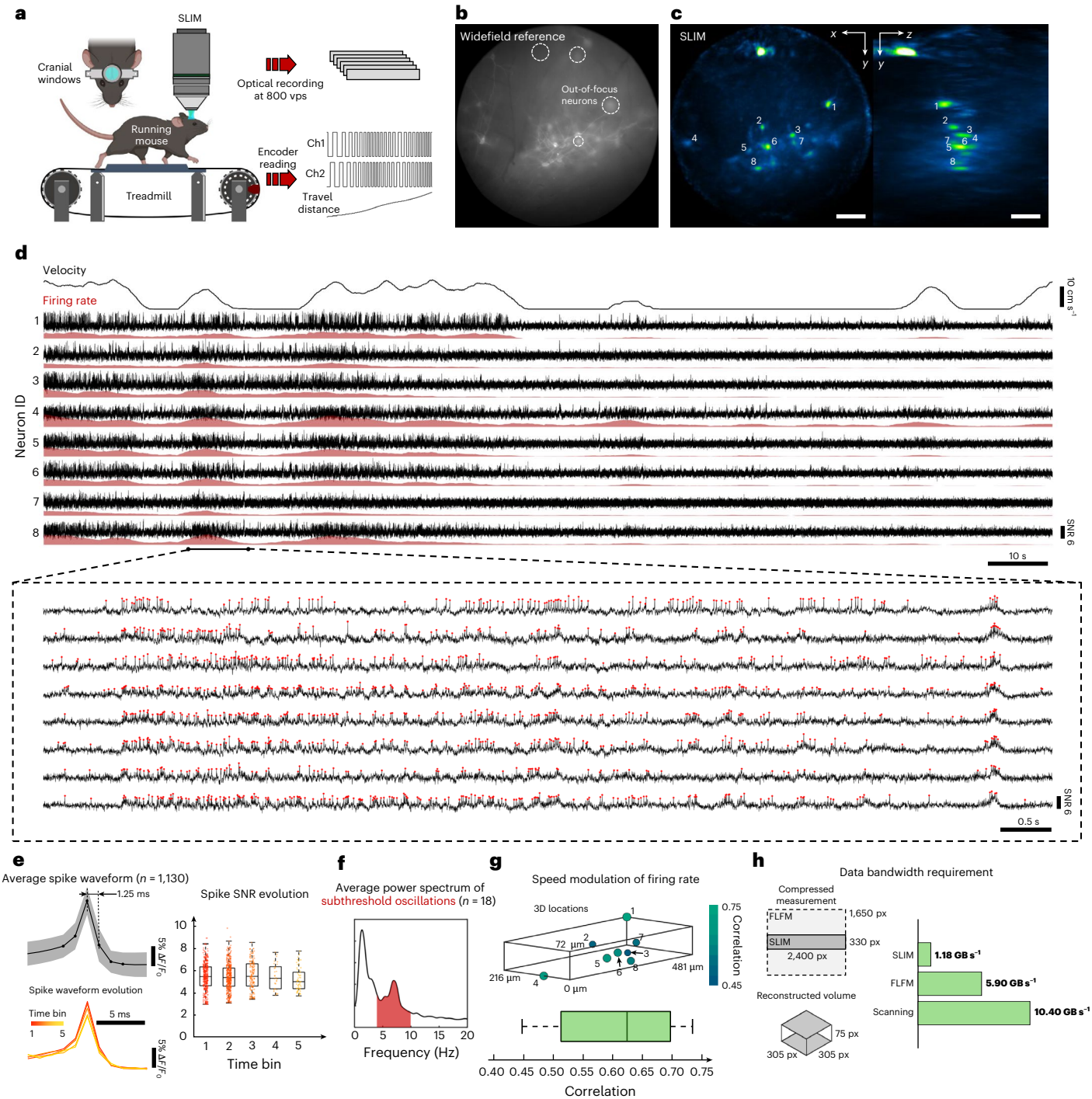

Fig. 4 | 3D voltage imaging of hippocampus in behaving mice at 800 vps. **a**, Schematics of the experiment setup. The animal expressing GEVI is placed on a customized treadmill. SLIM captures volumetric fluorescent signals through cranial windows, while an optical rotary encoder on the treadmill simultaneously records the belt's motion. **b**, Widefield reference camera captures a high-resolution, long-exposure 2D image of the targeted FOV. Dashed circles highlight out-of-focus neurons. **c**, 3D MIP of SLIM reconstruction. Scale bars, 100 µm. **d**, Detrended fluorescent signal traces over a 170-s recording, extracted from neurons labeled in **c**. The top row shows the animal's locomotion velocity. The red-shaded curve represents neuronal firing rates. The inset zooms in on the signals within the 24–34 s window. Red dots represent detected spikes. **e**, Average spike waveform calculated from 1,130 detected spikes in neuron 1. By further dividing the signal trace into five time bins (35 s each), the evolution of waveform can be visualized in box plots (n = 417, 459, 166, 30, 58). The spike SNR is measured as the spike magnitude over the signal's standard deviation within each time bin. Dots represent individual spike measurements. **f**, Average power spectrum of neural signal traces (n = 18). See Extended Data Fig. 2 for signal traces and their individual power spectra. **g**, Pearson correlation between firing rate and locomotion velocity. Top: 3D locations of selected neurons with correlation values encoded by color. Bottom: box plot showing distribution of correlation coefficients of neurons shown in **d** (n = 8). **h**, Data bandwidth required for camera read-out and storage. Raw data size for SLIM, FLFM and scanning-based methods is roughly estimated based on the digital image dimensions (left panel) in 16 bits. Box plots display the median (center line) with upper and lower quartiles (box limits); whiskers represent 1.5 × interquartile range and individual data points represent one sample. px, pixels. Illustrations in **a** created with BioRender.com.

https://doi.org/10.1038/s41592-025-02843-8

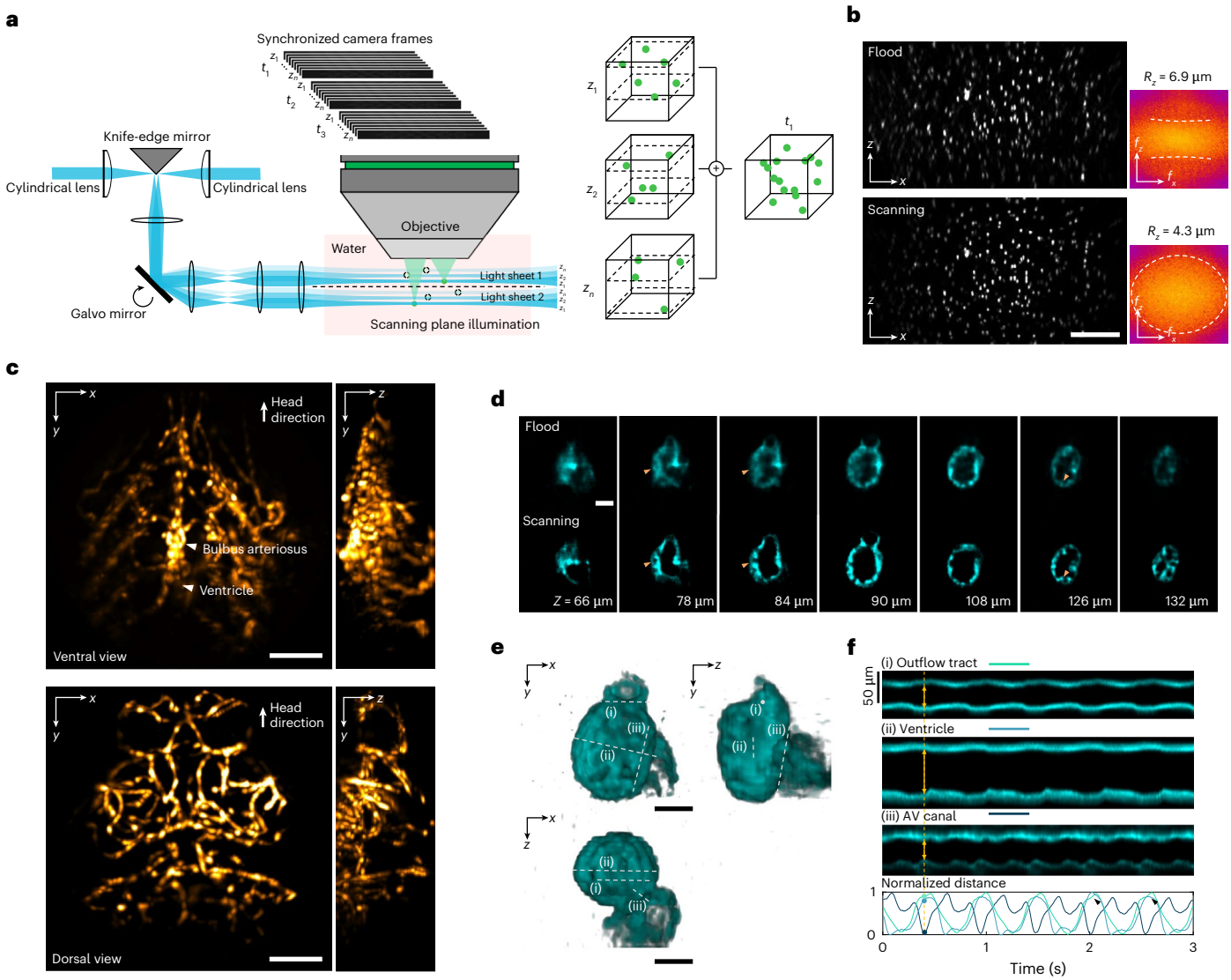

Fig. 5 | 3D imaging of a beating zebrafish heart with multi-plane scanning light-sheet illumination at 300 vps. a, Dual scanning light sheet replaces the flood illumination (that is, illuminating entire sample volume). In synchrony with the light sheet, the camera captures multiple frames at different scanning positions, each reconstructing two layers of the entire volume. By combining all measurements in one scan cycle, a 3D volume is synthesized for that time point. **b**, The *x*–*z* MIPs of fluorescent beads show image contrast and axial resolution. Axial resolution R_z has been quantified by frequency analysis. Scale bar, 100 µm. **c**, The structural images of the vasculature network in an embryonic zebrafish. Scale bars, 100 µm. **d**, Comparison of *x*–*y* cross-section images between scanning light-sheet illumination and flood illumination on cardiomyocytes in the zebrafish heart. The orange arrowheads mark muscle structures. Scale bar, 50 µm. **e**, The 3D rendering of myocardium at a representative time point. Scale bars, 50 µm. **f**, Kymographs calculated by sampling the time-dependent distance of the cavity along the white dashed line in **e**. The black arrowheads indicate the beat-to-beat variance of cardiac contraction. Scale bar, 50 µm.

voltage imaging across large volumes (Supplementary Fig. 17). Overall, SLIM enables 3D voltage imaging in neuron populations distributed across large volumes, with the potential to elucidate network dynamics and interactions among different cell types across layers.

Imaging of a beating embryonic zebrafish heart

Although LFM techniques, including SLIM, offer the ability to numerically refocus to specific depths, they typically lack intrinsic optical sectioning capability. Its application is potentially hindered by the spatial resolution and reconstruction artifacts, and it favors objects with high sparseness[50]. Here, we demonstrated that SLIM can be combined with scanning multi-sheet illumination. The synergy enables high-contrast 3D imaging of densely labeled fluorescent objects.

We constructed a dual-light-sheet illumination module and scanned the beams using a galvo-mirror driven by a sawtooth function. Rather than synchronizing the camera exposure with the entire scan range as in previous experiments, we operated the camera at a higher rate, allowing each frame to capture a subset of depth layers of the fluorescent object (Fig. 5a). This approach suppresses out-of-focus light and improves axial resolution by the thickness of the light sheet, as shown on fluorescent beads and zebrafish vasculature networks (*Tg(flk:mCherry)*) (Fig. 5b,c). On the other hand, SLIM offers an ultra-high frame rate and supports simultaneous multi-plane detection. These features enable SLIM to maintain a high volume rate even within this scanning scheme.

We demonstrated this acquisition scheme by imaging a beating zebrafish heart (*Tg(cmlc2:GFP)*) at 300 vps (Fig. 5d and Supplementary Video 5). This is achieved by scanning the dual-light sheets at 300 Hz, synchronized with camera recording at 4,800 fps (8-bit speed mode). This setup allowed us to reconstruct the heart with 30 planes across 200-µm depth range with the microstructures such as ventricular trabeculation clearly delineated (Fig. 5d,e). The enhanced spatial

resolution and contrast offer the potential for accurate segmentation of the heart chamber's geometry, facilitating cardiac studies, such as regional myocardial contractility analysis[51] and computational fluid dynamics for hemodynamic forces simulation[52]. While current LFM cardiac imaging is mostly demonstrated on sparse markers such as cardiomyocyte nuclei[18,19,21] and blood cells[19,20,53], SLIM with scanning multi-sheet illumination proves effective in resolving the densely labeled muscle tissue. It provides high 3D imaging speed to capture the beating heart in real time and outlines the time-dependent chamber dimension to detect beat-to-beat variations (Fig. 5f).

Discussion

We presented SLIM as a snapshot 3D detection method that addresses the pressing need for high-speed volumetric microscopy operating at kilohertz speeds. SLIM accomplishes this by capturing a condensed representation of the original light field using a compact ROI on the sensor. The sampling strategy is grounded in the principle that the inherent spatio-angular correlation in the light field can be exploited to recover signals from compressive measurement[25,26,28–30,32,54]. As with other compressed sensing approaches, accurate reconstruction in SLIM relies on the assumption of sample sparsity.

SLIM's kilohertz 3D imaging speed, which challenges previous methods and often entails considerable design trade-offs and demanding hardware requirements[9,24], presents opportunities to investigate millisecond-scale dynamics in emerging fields such as voltage imaging. It is adaptable to most CMOS sensors, which generally allow higher frame rates at reduced read-out pixel rows. While we set kilohertz as a milestone for 3D fluorescence microscopy, SLIM has the potential to achieve tens and even hundreds of thousands of volumes per second with current ultra-fast cameras.

Quantum efficiency and read-out noise are critical parameters that determine a sensor's sensitivity in low-light imaging. Unfortunately, these factors degrade notably in the ultra-fast cameras currently available. Another important factor, the full well capacity, is also frequently sacrificed together with bitdepth in trade for frame rate. It becomes a relevant limitation when the fluorescence change ($\Delta F/F_0$) is extremely low (for example, our leech ganglion imaging) and a high pixel brightness is required to provide an acceptable SNR[7]. Moreover, the extended-time imaging in animal behavior study often demands a substantial number of frames to be recorded, which becomes impractical for ultra-fast cameras that rely on limited on-board storage. Although this could be potentially solved by a camera array with a dedicated computer cluster for data handling[55], there are considerable technical and cost challenges in integrating high performance sensors into an array. In contrast, SLIM presents an accessible solution to transform a single commonly used sCMOS into a kilohertz 3D imaging tool.

SLIM offers a snapshot acquisition that effectively addresses the trade-off between the pixel exposure time and volumetric frame rate encountered in conventional scanning-based 3D optical microscopy techniques. This approach provides SLIM with distinct advantages in photon efficiency and SNR, making it particularly beneficial for high-speed imaging of weak fluorescence.

SLIM compresses images only along the vertical axis and redistributes the information to the horizontal axis, which retains full sampling power through image rotation. As a result, SLIM can reconstruct the FOV equivalent to that of a full-sensor FLFM system, achieving comparable spatial resolution provided the sample is sufficiently sparse (see Extended Data Fig. 3 for validation against ground truth). This design is specifically tailored to use a low-format rectangular sensor, marking a fundamental departure from existing compressive light field imaging[25–31,54]. The latter retrieves light fields at the same or lower resolutions than the multiplexed measurement and suffers from a linear reduction in FOV and pixels as it crops the sensor ROI. Moreover, SLIM does not require multiple shots[25] or learning on a sparse basis before reconstruction[27]. It also shows scalability in various ROI sizes. Provided the sample sparsity allows, it can tolerate a narrow sensor size and further increase its space-bandwidth-frame rate product by using faster recording speeds. Moreover, the SLIM strategy could potentially be integrated with anisotropic binning capabilities of CCD image sensors, enabling in-sensor image compression with reconfigurable compression ratios. This would provide SLIM with greater flexibility, allowing it to be optimized for imaging scenes with varying complexity.

SLIM can transform an existing FLFM[15,22,36,50] into a high-speed 3D imager with a substantially higher frame rate. Its performance approximates FLFM when the targeted dynamics exhibit sufficient spatiotemporal sparseness. However, as with all compressive detection systems, SLIM is susceptible to performance degradation when imaging dense signals with complex structures. Moreover, SLIM shares several limitations inherent to conventional FLFM, such as the missing cone problem, compromised spatial resolution, depth-variant performance and limited considerations for tissue scattering and lens aberrations. In addition, our current reconstruction assumes no occlusions in the scene[28,30]. These constraints limit its direct applicability in complex intravital imaging scenarios.

We have shown that multi-sheet scanning offers a solution by trading imaging speed for improved optical sectioning, extending SLIM's applicability to densely labeled tissue imaging. The refocusing capability within a largely extended depth of field makes SLIM compatible with various 3D illumination structures. For large organisms where direct lateral access is limited, oblique illumination microscopy[56] or swept confocally aligned planar excitation microscopy[10] could be potentially used. In addition, the literature presents several strategies to enhance SLIM's performance, such as background rejection by hardware[17] and computation[57], multi-focus optics for extended depth of field[15,58] and sparsity-based resolution enhancement[50,54]. Furthermore, ongoing advancements in data-driven reconstruction algorithms, particularly physics-embedded deep-learning models[20,22], hold promise for addressing the ill-posed inverse problems associated with limited space-bandwidth and compressive detection in SLIM. These developments are expected to enhance SLIM's capabilities and broaden its utility across diverse imaging scenarios.

Finally, although beyond the scope of the current work, SLIM holds promise for extending fast volumetric imaging to other spectral ranges, such as the short-wave infrared region, where large-format image sensors remain challenging to fabricate. In these spectral regions, the inherently pixel-intensive nature of conventional LFM presents logistical hurdles. For instance, InGaAs cameras, widely used for short-wave infrared applications, typically feature limited pixel counts due to manufacturing complexity and high costs, thereby constraining their utility in conventional light field imaging. The SLIM approach, by substantially reducing the required number of camera pixels for 3D reconstruction, offers a compelling solution. It allows high-resolution volumetric imaging to be achieved within the practical and economical pixel budgets of existing short-wave infrared cameras, potentially opening new avenues for deep tissue imaging and biomedical exploration[59,60].

Online content

Any methods, additional references, Nature Portfolio reporting summaries, source data, extended data, supplementary information, acknowledgements, peer review information; details of author contributions and competing interests; and statements of data and code availability are available at https://doi.org/10.1038/s41592-025-02843-8.

References

1. Meng, G. et al. Ultrafast two-photon fluorescence imaging of cerebral blood circulation in the mouse brain in vivo. *Proc. Natl Acad. Sci. USA* **119**, e2117346119 (2022).
2. Abdelfattah, A. S. et al. Bright and photostable chemigenetic indicators for extended in vivo voltage imaging. *Science* **365**, 699–704 (2019).

3. Abdelfattah, A. S. et al. Sensitivity optimization of a rhodopsin-based fluorescent voltage indicator. *Neuron* **111**, 1547–1563.e9 (2023).
4. Hochbaum, D. R. et al. All-optical electrophysiology in mammalian neurons using engineered microbial rhodopsins. *Nat. Methods* **11**, 825–833 (2014).
5. Wu, J. et al. Kilohertz two-photon fluorescence microscopy imaging of neural activity in vivo. *Nat. Methods* **17**, 287–290 (2020).
6. Zhang, T. et al. Kilohertz two-photon brain imaging in awake mice. *Nat. Methods* **16**, 1119–1122 (2019).
7. Wang, Z. et al. Imaging the voltage of neurons distributed across entire brains of larval zebrafish. Preprint at https://doi.org/10.1101/2023.12.15.571964 (2023).
8. Weber, T. D., Moya, M. V., Kılıç, K., Mertz, J. & Economo, M. N. High-speed multiplane confocal microscopy for voltage imaging in densely labeled neuronal populations. *Nat. Neurosci.* **26**, 1642–1650 (2023).
9. Sacconi, L. et al. KHz-rate volumetric voltage imaging of the whole Zebrafish heart. *Biophys. Rep.* **2**, 100046 (2022).
10. Voleti, V. et al. Real-time volumetric microscopy of in vivo dynamics and large-scale samples with SCAPE 2.0. *Nat. Methods* **16**, 1054–1062 (2019).
11. Pavani, S. R. P. et al. Three-dimensional, single-molecule fluorescence imaging beyond the diffraction limit by using a double-helix point spread function. *Proc. Natl Acad. Sci. USA* **106**, 2995–2999 (2009).
12. Llull, P. et al. Coded aperture compressive temporal imaging. *Opt. Express* **21**, 10526–10545 (2013).
13. Wagadarikar, A. A., Pitsianis, N. P., Sun, X. & Brady, D. J. Video rate spectral imaging using a coded aperture snapshot spectral imager. *Opt. Express* **17**, 6368–6388 (2009).
14. Prevedel, R. et al. Simultaneous whole-animal 3D imaging of neuronal activity using light-field microscopy. *Nat. Methods* **11**, 727–730 (2014).
15. Cong, L. et al. Rapid whole brain imaging of neural activity in freely behaving larval zebrafish (*Danio rerio*). *eLife* **6**, e28158 (2017).
16. Skocek, O. et al. High-speed volumetric imaging of neuronal activity in freely moving rodents. *Nat. Methods* **15**, 429–432 (2018).
17. Zhang, Z. et al. Imaging volumetric dynamics at high speed in mouse and zebrafish brain with confocal light field microscopy. *Nat. Biotechnol.* **39**, 74–83 (2021).
18. Wagner, N. et al. Instantaneous isotropic volumetric imaging of fast biological processes. *Nat. Methods* **16**, 497–500 (2019).
19. Wang, Z. et al. Real-time volumetric reconstruction of biological dynamics with light-field microscopy and deep learning. *Nat. Methods* **18**, 551–556 (2021).
20. Lu, Z. et al. Virtual-scanning light-field microscopy for robust snapshot high-resolution volumetric imaging. *Nat. Methods* **20**, 735–746 (2023).
21. Wagner, N. et al. Deep learning-enhanced light-field imaging with continuous validation. *Nat. Methods* **18**, 557–563 (2021).
22. Yi, C. et al. Video-rate 3D imaging of living cells using Fourier view-channel-depth light field microscopy. *Commun. Biol.* **6**, 1259 (2023).
23. Tian, T., Yuan, Y., Mitra, S., Gyongy, I. & Nolan, M. F. Single photon kilohertz frame rate imaging of neural activity. *Adv. Sci.* **9**, 2203018 (2022).
24. Guo, R. et al. EventLFM: event camera integrated Fourier light field microscopy for ultrafast 3D imaging. *Light Sci. Appl.* **13**, 144 (2024).
25. Ashok, A. & Neifeld, M. A. Compressive light field imaging. In *Proc. Three-Dimensional Imaging, Visualization, and Display 2010 and Display Technologies and Applications for Defense, Security, and Avionics IV* Vol. 7690 (eds Bahram, J. et al.) 221–232 (SPIE, 2010).
26. Babacan, S. D. et al. Compressive light field sensing. *IEEE Trans. Image Process.* **21**, 4746–4757 (2012).
27. Marwah, K., Wetzstein, G., Bando, Y. & Raskar, R. Compressive light field photography using overcomplete dictionaries and optimized projections. *ACM Trans. Graph.* **32**, 46:1–46:12 (2013).
28. Antipa, N., Necula, S., Ng, R. & Waller, L. Single-shot diffuser-encoded light field imaging. In *2016 IEEE International Conference on Computational Photography (ICCP)* 1–11 (IEEE, 2016).
29. Liu, F. L., Kuo, G., Antipa, N., Yanny, K. & Waller, L. Fourier diffuserScope: single-shot 3D Fourier light field microscopy with a diffuser. *Opt. Express* **28**, 28969–28986 (2020).
30. Yanny, K. et al. Miniscope3D: optimized single-shot miniature 3D fluorescence microscopy. *Light. Sci. Appl.* **9**, 171 (2020).
31. Antipa, N. et al. DiffuserCam: lensless single-exposure 3D imaging. *Optica* **5**, 1–9 (2018).
32. Feng, X., Ma, Y. & Gao, L. Compact light field photography towards versatile three-dimensional vision. *Nat. Commun.* **13**, 3333 (2022).
33. Feng, X. & Gao, L. Ultrafast light field tomography for snapshot transient and non-line-of-sight imaging. *Nat. Commun.* **12**, 2179 (2021).
34. Wang, Z., Hsiai, T. K. & Gao, L. Augmented light field tomography through parallel spectral encoding. *Optica* **10**, 62–65 (2023).
35. Mandracchia, B. et al. High-speed optical imaging with sCMOS pixel reassignment. *Nat. Commun.* **15**, 4598 (2024).
36. Guo, C. et al. Fourier light-field microscopy. *Opt. Express* **27**, 25573–25594 (2019).
37. Llavador, A., Sola-Pikabea, J., Saavedra, G., Javidi, B. & Martínez-Corral, M. Resolution improvements in integral microscopy with Fourier plane recording. *Opt. Express* **24**, 20792–20798 (2016).
38. Scrofani, G. et al. FIMic: design for ultimate 3D-integral microscopy of in-vivo biological samples. *Biomed. Opt. Express* **9**, 335–346 (2018).
39. Levoy, M., Ng, R., Adams, A., Footer, M. & Horowitz, M. Light field microscopy. *ACM Trans. Graph.* **25**, 924–934 (2006).
40. Broxton, M. et al. Wave optics theory and 3-D deconvolution for the light field microscope. *Opt. Express* **21**, 25418–25439 (2013).
41. Zhou, Y., Zickus, V., Zammit, P., Taylor, J. M. & Harvey, A. R. High-speed extended-volume blood flow measurement using engineered point-spread function. *Biomed. Opt. Express* **9**, 6444–6454 (2018).
42. Tomina, Y. & Wagenaar, D. A. A double-sided microscope to realize whole-ganglion imaging of membrane potential in the medicinal leech. *eLife* **6**, e29839 (2017).
43. Briggman, K. L. & Kristan, W. B. Imaging dedicated and multifunctional neural circuits generating distinct behaviors. *J. Neurosci.* **26**, 10925–10933 (2006).
44. Briggman, K. L., Abarbanel, H. D. I. & Kristan, W. B. Optical imaging of neuronal populations during decision-making. *Science* **307**, 896–901 (2005).
45. Kannan, M. et al. Dual-polarity voltage imaging of the concurrent dynamics of multiple neuron types. *Science* **378**, eabm8797 (2022).
46. Buzsáki, G. Theta oscillations in the hippocampus. *Neuron* **33**, 325–340 (2002).
47. Gu, Z. et al. Hippocampal interneuronal α7 nAChRs modulate theta oscillations in freely moving mice. *Cell Rep.* **31**, 107740 (2020).
48. Taxidis, J. et al. Voltage imaging reveals hippocampal inhibitory dynamics shaping pyramidal memory-encoding sequences. *Nat. Neurosci.* **28**, 1946–1958 (2025).
49. Varga, C., Golshani, P. & Soltesz, I. Frequency-invariant temporal ordering of interneuronal discharges during hippocampal oscillations in awake mice. *Proc. Natl Acad. Sci. USA* **109**, E2726–E2734 (2012).

50. Yoon, Y.-G. et al. Sparse decomposition light-field microscopy for high speed imaging of neuronal activity. *Optica* **7**, 1457–1468 (2020).
51. Wang, Z. et al. A hybrid of light-field and light-sheet imaging to study myocardial function and intracardiac blood flow during zebrafish development. *PLoS Comput. Biol.* **17**, e1009175 (2021).
52. Vedula, V. et al. A method to quantify mechanobiologic forces during zebrafish cardiac development using 4-D light sheet imaging and computational modeling. *PLoS Comput. Biol.* **13**, e1005828 (2017).
53. Zhang, Y. et al. DiLFM: an artifact-suppressed and noise-robust light-field microscopy through dictionary learning. *Light. Sci. Appl.* **10**, 152 (2021).
54. Pégard, N. C. et al. Compressive light-field microscopy for 3D neural activity recording. *Optica* **3**, 517–524 (2016).
55. Lin, X., Wu, J., Zheng, G. & Dai, Q. Camera array based light field microscopy. *Biomed. Opt. Express* **6**, 3179–3189 (2015).
56. Dunsby, C. Optically sectioned imaging by oblique plane microscopy. *Opt. Express* **16**, 20306–20316 (2008).
57. Zhang, Y. et al. Computational optical sectioning with an incoherent multiscale scattering model for light-field microscopy. *Nat. Commun.* **12**, 6391 (2021).
58. Zhang, Y. et al. Multi-focus light-field microscopy for high-speed large-volume imaging. *PhotoniX* **3**, 30 (2022).
59. Li, C., Chen, G., Zhang, Y., Wu, F. & Wang, Q. Advanced fluorescence imaging technology in the near-infrared-II window for biomedical applications. *J. Am. Chem. Soc.* **142**, 14789–14804 (2020).
60. Miao, Y. et al. Recent progress in fluorescence imaging of the near-infrared II window. *Chem. Bio. Chem.* **19**, 2522–2541 (2018).

Methods

Hardware setup

For SLIM setup using selective volume side illumination, the detection features a ×20 water-dipping objective (N20X-PFH, Olympus XLUMPLFLN ×20, 1.0 numerical aperture (NA)). A 4F relay system (AC508-180-A, AC508-200-A, Thorlabs) forms a conjugate plane of the objective's back pupil, accommodating a customized dove prism and a spherical lenslet array. The dove prism (aperture length 1.3 mm, material H-K9L, fabricated by Changchun Sunday Optics) is positioned anteriorly to the plano-convex lenslet (aperture diameter 1.3 mm, focal length 36 mm, material PMMA, fabricated in-house). Each pair generates a rotated subaperture image with a magnification of ×3.6 and NA of 0.065. In total, 29 pairs are used and securely housed in 3D-printed mechanical holders (refer to Supplementary Fig. 1 for detailed designs of the prism, lenslet and holder). Our anamorphic relay system comprises a spherical achromat doublet (ACT508-250-A, Thorlabs) and two orthogonally oriented cylindrical achromat doublets (ACY254-250-A, ACY254-50-A, Thorlabs). The back focal planes of two cylindrical lenses are colocated, producing an image with an anisotropic scaling factor (Supplementary Fig. 2). A sCMOS camera (Kinetix, Teledyne) captures the final image, with a 320 × 3,200 pixels ROI covering all 29 subaperture images, or a 200 × 3,200 pixels ROI for 19 subaperture images. The maximal read-out speeds for two ROI are 830 fps and 1,326 fps in 16-bit dynamic range mode and 4,790 fps and 7,476 fps in 8-bit speed mode. The 29 subaperture configuration collects around 50% more light than the 19 subaperture one.

The illumination sources include blue and green continuous lasers (MBL-FN-473-500mW and MGL-III-532-300mW, CNI Laser) and an ultra-low-noise blue LED (UHP-T-470SR, Prizmatix). For scanning light-sheet setup, we use a knife-edge mirror (MRAK25-G01, Thorlabs) to combine two beams with adjustable spacing and a galvo-mirror (GVS011, Thorlabs) to scan them together. Planar illumination is formed perpendicular to the detection axis by a cylindrical lens and a dry objective (RMS4X-PF, Olympus ×4, 0.13 NA). We use a sawtooth function to drive the galvo-mirror. In synthetic volume illumination configuration, we block one light-sheet beam. The camera is then triggered at the beginning of the sawtooth waveform and exposed for the entire scan. In scanning plane illumination configuration, we use two light-sheet beams and trigger the camera multiple times during a scan. The static LED setup shares the same illumination objective and perpendicular geometry. We build a Koehler illumination system and use an adjustable slit as a field aperture. The conjugate image of the slit is relayed to the sample, and the slit controls the depth range of the beam. The LED provides ultra-stable illumination power and thus suppresses excitation source noise during our voltage imaging experiments.

For SLIM setup using widefield epi-illumination, we use a ×16 water-dipping objective (×16 Nikon CFI LWD Plan Fluorite Objective, 0.80 NA). The back pupil relay system uses a pair of doublets (AC508-150-A, Thorlabs). The dove prism, lenslet array and anamorphic relay system are identical to the selective volume side-illumination setup. An ultra-low-noise blue LED (UHP-T-470SR, Prizmatix) in a Koehler configuration is used for epi-illumination.

See Supplementary Figs. 4 and 5 for system schematics, Supplementary Table 3 for components list and Supplementary Table 4 for configurations used in different experiments.

Image formation and reconstruction

The light field of the fluorescent sample is acquired by dividing the objective's back pupil with a lenslet array and recording a group of subaperture images. Depending on their subaperture locations, they display disparity, that is the distinct displacement shown by the same signal. After calibrating the displacement at every axial position, the formation of each subaperture image can be modeled as a sum of laterally shifted depth slices. We replace the shifting operator with a convolution with PSF to account for both the diffraction and displacement. A dove prism is a truncated right-angle prism and used to rotate the incident beam. The rotation of the prism around its longitudinal axis causes the beam to rotate at twice the rate of the prism's rotation. By placing a dove prism array in the infinity space between the objective and lenslet array, we apply varying in-plane rotations to subaperture images. Finally, we adopt an anamorphic relay system to introduce anisotropic scaling to the image array: we de-magnify (squeeze) the image in the direction perpendicular to the camera read-out axis while maintaining the original scale in the other direction (Supplementary Fig. 2). This one-axis scaling and the aforementioned in-plane rotation are both directly applied to the 3D fluorescent image in our model.

Given a 3D fluorescence distribution $O(x,y,z)$ and system PSF, the formation of camera measurement $I(x,y,v)$ can be modeled as:

$$I(x,y,v) = \sum_{z}(S \times R(v) \times O(x,y,z)) \bigotimes \mathrm{PSF}(x,y,z,v), \quad (1)$$

where v is the index of subaperture, $\otimes$ represents the 2D convolution, $R(v)$ applies subaperture-dependent rotation from the dove prism and S introduces image scaling from the anamorphic relay system.

The volume reconstruction algorithm was derived from Richardson–Lucy deconvolution[14,15,36,61] (Supplementary Note 2). Based on the forward model (1), the 3D fluorescence distribution $O(x,y,z)$ is iteratively solved from the camera measurements $I(x,y,v)$ and empirical PSFs. The rotation angles and image scaling ratio are precalibrated as known priors in the reconstruction. The measurement patch $I(x,y,v)$ is cropped from the raw sensor image according to the center location of each subaperture image. We experimentally measure the PSFs by imaging a subdiffraction fluorescent bead. The point source is placed in the middle of FOV and axially scanned over a broad 600-µm depth range with a 2-µm step size using a motorized translation stage. The actual axial range and step size in the reconstruction depends on the specific experiments. The PSF is assumed to be spatially invariant within each subaperture image.

With our implementation, each measurement patch $I(x,y,v)$ has a resolution of 301 × 61 pixels. The numbers of channels (v) and axial slices (z) are configured based on the targeted frame rate and depth range and/or step size. For example, with 19 subaperture measurements to reconstruct a volume of 305 × 305 × 151 pixels, the deconvolution takes around 30 s via eight iterations using a desktop computer with a modest graphical processing unit (Nvidia RTX 3070).

Fluorescent beads imaging and resolution characterization

Fluorescent microspheres of 1 µm (F13082, ThermoFisher) were embedded in 1% low-melting agarose and injected into a transparent fluorinated ethylene propylene tube for imaging. To acquire experimental PSFs, the solution was highly diluted to keep only one bead in the FOV. For spatial resolution quantification, the beads were randomly distributed in space, and we measured the full-width at half-maximum of the bead image at various locations in the FOV (Supplementary Fig. 3). We also performed two-point resolving experiments by reconstructing synthetic measurements that added two sequentially captured frames. We translated the bead laterally and axially at varying distances in these two frames. The resolution was then indicated by the resolvable set with the least distance (Supplementary Fig. 3).

Fish husbandry and imaging

Transgenic zebrafish lines *Tg(gata1a:dsRed)*, *Tg(flk:mCherry)* and *Tg(cmlc:GFP)* were used in our experiments for imaging blood cells, endothelial cells and myocardium, respectively. Embryonic fish were maintained at 3 days postfertilization in standard E3 medium, which was supplemented with extra 1-phenyl 2-thiourea (Sigma Aldrich) to inhibit melanogenesis at day one. For brain hemodynamics and cardiac imaging, the larvae were anesthetized with tricaine (3-aminobenzoic acid ethyl ester, Sigma Aldrich) and immobilized in 1% low-melting-point agarose inside a fluorinated ethylene propylene tube

before imaging. For tail experiments, the larvae were first positioned on cover glass before the heads were fixed by 3% low-melting-point agarose. Immediately after the agarose solidified, the sample was immersed in a water chamber. The imaging starts after visually confirming the unconstrained movement of the tail. All the experiments were performed in compliance with and with the approval of a UCLA IACUC protocol.

Blood cell velocimetry

3D cell tracking was performed by ImageJ and the plugin Trackmate[62,63]. We used the difference of Gaussian blob detector and the linear assignment problem tracker for all experiments. The spot positions and trajectory properties were exported to MATLAB for further analysis and visualization. We removed the local oscillation from the tracking result by fitting a center line of each trajectory with a smooth spline. The tangential velocity was calculated by projecting the cell displacement in adjacent frames onto the center line. The trajectories were then color-coded by the tangential velocity to display the blood flow speed along the vessels. The tracking accuracy was quantified by imaging static fluorescent beads (Supplementary Fig. 8)

Leech sample preparation

Medicinal leeches (*Hirudo verbana*) obtained from leech.com were housed in artificial pond water maintained at 15 °C. Detailed dissection procedures have been described before[42,64]. Briefly, an adult leech was anesthetized in ice-cold leech saline and an individual segmental ganglion (M10 or M11) was dissected out. The ganglion was pinned down ventral side up on a rectangular-shaped flat substrate made of polydimethylsiloxane (Sylgard 184, Dow Corning). After removing the sheath that covers the ganglion, a voltage-sensitive dye[65] (FluoVolt, F10488, ThermoFisher) was bath-loaded using a peristaltic pump. The sample was placed under the detection objective of the SLIM system for imaging. In swim experiments, the entire nervous system was dissected out, except for the cephalic ganglia. Segmental ganglion M10 or M11 was desheathed as before. In addition, the dorsal posterior nerves (DP1) of ganglion M13 or M14 were exposed for extracellular stimulation and recording with a suction electrode. Nerve stimulation in these caudal ganglia is a well-established method for eliciting fictive swimming.

Leech ganglion electrophysiology and imaging

Glass microelectrodes (20–50 MΩ) were filled with a recording solution of 3 M potassium acetate and 60 mM potassium chloride. After penetrating the membrane of a cell of interest, small negative holding currents were injected to ensure stability. Intracellular electrophysiology used Neuroprobe amplifiers (Model 1600; A-M systems). Membrane voltage and electrode current were digitized along with the camera trigger signal at 10 kHz using a 16-bit data acquisition board (NI USB-6002; National Instruments). We used the camera triggers as time stamps to align recorded frames with electrophysiological data. Extracellular electrophysiology used a custom-built differential amplifier that allowed for rapid switching between stimulation and recording.

After image reconstruction, we corrected for sample movement by running a 2D registration and demotion between adjacent frames using a modified version of SWiFT-IR[66]. The 3D ROI were then manually defined for each neuron. The optical read-out F_t was calculated by averaging the pixel intensities in the ROI and normalized by the temporal baseline: $F = F_t - F_0/F_0$, where F_0 is the temporal mean value. To detect spikes from the optical signal, we detrended the trace F by subtracting its median-filtered version (window size, 50 ms). It was then binarized by a Schmitt trigger, and a peak detection was performed to locate the voltage spikes.

Coherence analysis method

We used multitaper estimation techniques[67] to calculate the power spectral densities denoted as $S_{opt}(f)$ for the optical signals and $S_{ref}(f)$ for the reference signal, and their coherence, denoted as $C(f)$. The use of multiple tapers ensures a more balanced weighting across all regions of a record, in contrast to the central bias introduced by a single taper. In addition, this approach allows for the estimation of the standard deviation of the spectral estimates within a single trial. The spectral measures are defined by $S_{opt}(f) = \langle V_{opt}(f) V^*_{opt}(f)\rangle_{tapers}$. The brackets denote an average over all trials and tapers, specifically, $\langle V(f) U(f)\rangle_{tapers} = \frac{1}{K}\sum_{k=1}^{K} V^{(k)}(f) U^{(k)}(f)$, where K is the number of tapers. $V^{(k)}(f)$ is the discrete Fourier transform of the product $w^{(k)}(t)V(t)$, which refers to the time-domain optical signal $V(t)$ multiplied by the kth taper $w^{(k)}(t)$. The discrete prolate spheroidal sequences (Slepian sequences) are used as tapers to minimize power leakage between frequency bands. In fictive swimming datasets ($T = 12$ s), we selected extracellular recording as reference signal and used ten tapers ($K = 10$) for spectral coherence analysis. Additional processing steps, including demotion and detrending, were applied before the coherence analysis.

Standard deviations of the coherence are reported as jackknife estimates within single trials[68]. In this method, the variance of a dataset with K independent estimates of a quantity is calculated by sequentially deleting each estimate and computing the variance over the K resulting averages. The 'delete-one' averages of coherence, denoted as $C_j(f)$ where j is the index of the deleted taper, are given by $C_j(f) = \langle V_{opt}(f) V_{ref}(f)\rangle_{tapers\neq j} / \sqrt{S_{opt;j}(f) S_{ref;j}(f)}$, where $S_{opt;j}(f) = \langle V_{opt}(f) V^*_{opt}(f)\rangle_{tapers\neq j}$.

The standard deviation of the magnitude of $C(f)$ is then computed as $\sigma_{mag}(f) = \sqrt{(K-1)/K \sum_{j=1}^{K} |C_j(f) - C(f)|^2}$. The variance estimate for the phase is determined by comparing the relative directions of the delete-one unit vectors. The standard deviation is computed as $\sigma_{phase}(f) = \sqrt{[2(K-1)/K]\,[K - |\sum_{j=1}^{K} C_j(f)/|C_j(f)||}$.

Behaving mouse sample preparation

All experiments were conducted according to the National Institutes of Health (NIH) guidelines and with the approval of the Chancellor's Animal Research Committee of the University of California, Los Angeles. Mice were anesthetized with isoflurane (5% for induction, 1–2% (v/v) for maintenance). The depth of anesthesia was monitored continuously and adjusted when necessary. After induction of anesthesia, the mice were fitted into a stereotaxic frame (Kopf), with their heads secured by blunt ear bars and their noses placed into an anesthesia and ventilation system (David Kopf Instruments). Body temperature was kept at 37 °C with a feedback-controlled heating pad (Harvard Apparatus). Mice were administered 0.05 ml of lidocaine (2%; Akorn) subcutaneously as a local anesthetic before surgery. The surgical incision site was cleaned three times with 10% povidone-iodine and 70% ethanol. After removing the scalp and clearing the skull of connective tissues, we drilled a hole above the virus injection location. Then, we injected GEVIs to the CA1 of the hippocampus, with coordinates mediolateral ±1.8 mm, anteroposterior −2 mm, dorsoventral −1.3 mm from Bregma. One Chrna2$^-$Cre$^+$ male mouse was injected with Cre-dependent GEVI pAce (AAV-DJ-CAG-DIO-pAce-kv2.1; titer, 2.6×10^{12} viral genomes per ml), allowing for imaging of neuron populations expressing nicotinic acetylcholine receptor alpha2, a specific marker for oriens lacunosum-moleculare interneurons[69]. Another wild-type male mouse was injected with a cocktail of the GEVI pAce (AAV9-EF1a-DIO-pAce-Kv-WPRE, titer, 2.1×10^{13} viral genomes per ml) and a principal-cell specific Cre promoter (pAAV1-CamKII-Cre, Addgene, 105558; titer, 1.9×10^{13} viral genomes per ml) allowing for imaging of excitatory pyramidal neurons. After the termination of viral injection, a circular craniotomy (3 mm diameter) was made around the injection site. Dura over the exposed brain surface was removed and the cortical tissue above the dorsal CA1 was carefully aspirated using a 27-gauge blunt needle. Buffered artificial cerebrospinal fluid (7.888 g NaCl, 0.372 g KCl, 1.192 g HEPES, 0.264 g $CaCl_2$, 0.204 g $MgCl_2$ per 1,000 ml Millipore water) was constantly applied throughout the aspiration to

prevent desiccation of the tissue. The aspiration ceased after partial removal of the corpus callosum and bleeding terminated, at which point a 3-mm titanium ring with a glass coverslip attached to its bottom was implanted into the aspirated area and its circular flange was secured to the skull surface using vetbond (3 M). A custom-made lightweight metal head holder (headbar) was attached to the skull posterior to the implant. Cyanoacrylate glue and black dental cement (Ortho-Jet, Lang Dental) were used to seal and cover the exposed skull. During recovery mice were administered carprofen (5 mg per kg of body weight) for 3 days as a systemic analgesic and amoxicillin antibiotic (0.25 mg ml^{-1} in drinking water) through the water supply for 7 days.

Behaving mouse imaging

Mice were imaged at least 3 weeks after surgery on a treadmill setup that used an optical rotary encoder to track movement for three minutes with epochs of locomotion and stationary behaviors. SLIM was configured to image at 800 Hz with a 1,230-µs exposure time for each frame, under a widefield epifluorescence illumination (UHP-T-470SR Prizmatix). The camera was externally triggered. A data acquisition board (NI USB-6002; National Instruments) recorded both the camera trigger signals and the two-channel rotary encoder outputs simultaneously at 10 kHz, allowing for alignment between optical read-out and animal locomotion.

The 3-min raw data from the camera (dynamic range mode, 16 bits) were continuously streamed to the host computer through a PCIe Gen 3x16 interface and saved on four solid-state drives (SSDs) (Samsung 970 Pro 1TB) in RAID-0 configuration via a controller (HighPoint SSD7101A-1). We also tested direct streaming to a single M.2 NVMe SSD (Samsung 970 Pro 1 TB). Both storage configurations enabled nonmissing-frame recording at 800 Hz for up to 10 min, thanks to SLIM's compressed data load. However, performance may decline after repeated acquisitions without sufficient intervals for SSD cache recovery. In addition, extended continuous recording is limited by fluorescence photobleaching (Supplementary Fig. 15). See Supplementary Table 4 for the illumination power in mice imaging experiments.

Each raw measurement contained 29 subaperture images, and we reconstructed a 3D volume with an axial range from −296 µm to 296 µm at a step size of 8 µm by eight iterations. The resulted image stack had a resolution of 305 × 305 × 75 pixels and took around 1 s on average after distributing the entire time sequence (~3 min, 144,000 frames) to 24 parallel workers (Parallel Computing Toolbox, MATLAB) in our workstations (graphical processing units: Nvidia RTX 2080, 3070 and 3090).

Similar to leech ganglion experiments, we corrected sample movement by SWiFT-IR[66] and manually defined 3D ROI for each neuron candidates. The optical read-out was calculated by averaging the pixels in the ROI and normalized by the temporal mean value. The spikes are detected by detrending the signals with a moving median filter (window size, 125 ms), binarizing by a Schmitt trigger and a peak detection. The signal traces visualized in the figures (Fig. 4, Extended Data Figs. 1 and 2 and Supplementary Fig. 16) used a larger filter window size (1 s) to keep the subthreshold oscillations. We calculated the ratio between the signal and the standard deviation of entire trace to represent the SNR. However, in the analysis of spike waveform evolution, the standard deviations were calculated for each individual time bin (35 s), respectively. The subthreshold oscillations (Extended Data Fig. 2) were analyzed by a band-pass filter (4–10 Hz) on the detrended signal (median filter window size, 1 s). To calculate the firing rate and animal locomotion velocity, we counted the number of spikes and rotary encoder pulses in the same sliding window (window size 5 s).

Image reconstruction with scanning multi-plane illumination

The axial positions of plane illumination during a scan were calibrated using fluorescent beads. For each scanning step, we reconstructed the bead measurement and localized two slices exhibiting the highest image contrasts. In the following imaging experiments, the same slices were sampled from the reconstruction and constituted a new stack with all other scanning steps. During high-speed scans, the sawtooth function that drives the galvo-mirror could suffer from the limited bandwidth of the waveform generator. We removed the measurements at the beginning and/or the end of the scan if repeating abnormalities (that happened at every cycle) were observed during the calibration. For image reconstruction of each scanning step, we treated it as the same reconstruction problem under volumetric illumination.

Reporting summary

Further information on research design is available in the Nature Portfolio Reporting Summary linked to this article.

Data availability

Data underlying the results are publicly available on GitHub at https://github.com/aaronzq/SLIM and via Zenodo at https://doi.org/10.5281/zenodo.15793563 (ref. 70). Source data are provided with this paper.

Code availability

Codes for 3D reconstruction are available on GitHub at https://github.com/aaronzq/SLIM and via Zenodo at https://doi.org/10.5281/zenodo.15793563 (ref. 70) under a BSD-License.

References

61. Biggs, D. S. C. & Andrews, M. Acceleration of iterative image restoration algorithms. *Appl. Opt.* **36**, 1766–1775 (1997).
62. Ershov, D. et al. TrackMate 7: integrating state-of-the-art segmentation algorithms into tracking pipelines. *Nat. Methods* **19**, 829–832 (2022).
63. Tinevez, J.-Y. et al. TrackMate: an open and extensible platform for single-particle tracking. *Methods* **115**, 80–90 (2017).
64. Tomina, Y. & Wagenaar, D. Dual-sided voltage-sensitive dye imaging of leech ganglia. *Bio. Protoc.* **8**, e2751 (2018).
65. Miller, E. W. et al. Optically monitoring voltage in neurons by photo-induced electron transfer through molecular wires. *Proc. Natl Acad. Sci. USA* **109**, 2114–2119 (2012).
66. Wetzel, A. W. et al. Registering large volume serial-section electron microscopy image sets for neural circuit reconstruction using FFT signal whitening. In *Proc. 2016 IEEE Applied Imagery Pattern Recognition Workshop (AIPR)* 1–10 (IEEE, 2016).
67. Thomson, D. J. Spectrum estimation and harmonic analysis. *Proc. IEEE* **70**, 1055–1096 (1982).
68. Thomson, D. J. Jackknifed error estimates for spectra, coherences, and transfer functions. In *Advances in Spectrum Analysis and Array Processing* Vol 1 (ed. Haykin, S. S.) 58–113 (Prentice Hall, 1991).
69. Nichol, H., Amilhon, B., Manseau, F., Badrinarayanan, S. & Williams, S. Electrophysiological and morphological characterization of Chrna2 cells in the subiculum and CA1 of the hippocampus: an optogenetic investigation. *Front. Cell. Neurosci.* **12**, 32 (2018).
70. Wang, Z. Source data for manuscript 'Kilohertz volumetric imaging of in-vivo dynamics using squeezed light field microscopy'. *Zenodo* https://doi.org/10.5281/zenodo.15793563 (2025).

Acknowledgements

We thank Y. Dong and Y. Zhang at UCLA for their assistance in zebrafish experiments. We acknowledge the David Geffen School of Medicine at UCLA for providing the Zebrafish Core Facilities. This work was supported by the following grants: NIH (grant nos. R01HL165318 (L.G.), RF1NS128488 (L.G.), R35GM128761 (L.G.), R01AI102584 (G.C.L.W.), R01HL129727 (T.K.H.), R01HL159970 (T.K.H.) and T32HL144449 (T.K.H.)). W.C.S. was supported by the National Science Foundation Graduate Research Fellowship Program (grant nos. DGE-1650604 and DGE-2034835) and Ruth L. Kirschstein National Research Service Award 'Multidisciplinary Training in Microbial Pathogenesis' (grant no.

T32AI007323). The funders had no role in study design, data collection and analysis, decision to publish or preparation of the paper.

Author contributions

Z.W. and L.G. conceived of the idea. L.G., D.A.W., R.L., G.C.L.W., T.K.H. and P.G. oversaw the project. Z.W. constructed the microscopes and developed the reconstruction algorithm. R.Z., D.A.W. and Z.W. prepared medicinal leech samples and electrophysiology study. D.E. and L.S. performed mouse surgery. Z.W., R.Z., A.P. and J.W. bred the zebrafish. C.K.L. and W.C.S. prepared bacteria samples. W.K. fabricated the lenslet array. Z.W., R.Z., D.A.W., D.E., L.S., O.B. and E.Z. collected the imaging data. Z.W. and R.Z. processed and analyzed the data. Z.W., R.Z. and L.G. wrote the paper. All authors reviewed, edited and consulted on the text.

Competing interests

L.G. has a financial interest in Lift Photonics. However, it was not involved in the research presented in this paper. The other authors declare no competing interests.

Additional information

Extended data is available for this paper at https://doi.org/10.1038/s41592-025-02843-8.

Supplementary information The online version contains supplementary material available at https://doi.org/10.1038/s41592-025-02843-8.

Correspondence and requests for materials should be addressed to Liang Gao.

Peer review information *Nature Methods* thanks Robert Prevedel and the other, anonymous, reviewer(s) for their contribution to the peer review of this work. Peer reviewer reports are available. Primary Handling Editor: Nina Vogt, in collaboration with the *Nature Methods* team.

https://doi.org/10.1038/s41592-025-02843-8

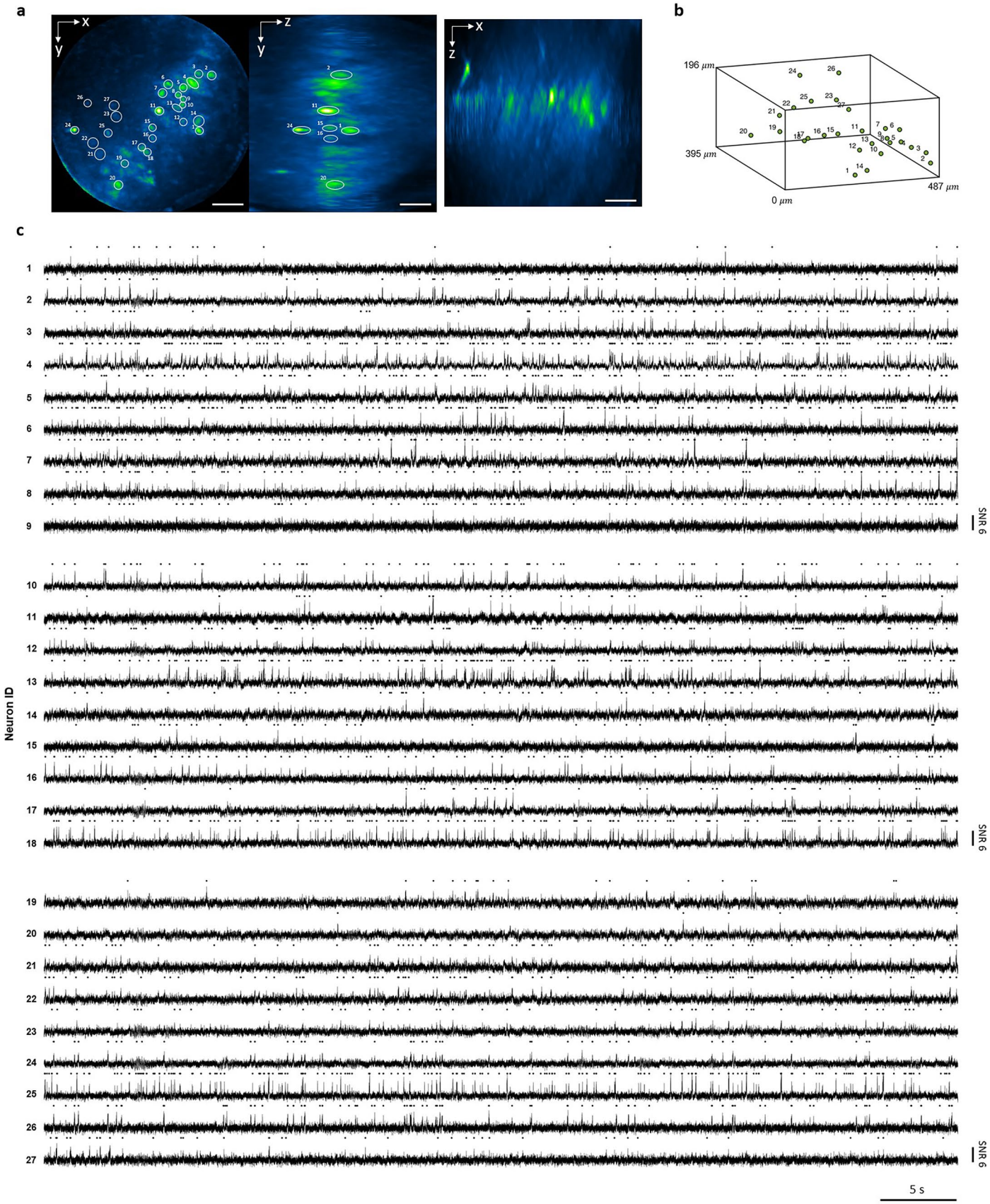

Extended Data Fig. 1 | 3D voltage imaging of hippocampus pyramidal neurons in awake mice. a. MIP of SLIM reconstruction of the 3D located neurons. Neuron indices are partially labeled in y-z view to avoid cluttered markers. Representative result from five FOVs using mice labeled for excitatory pyramidal neurons. Scale bar, 100 μm. **b**. 3D distribution of neuron center locations and their corresponding index. **c**. Detrended signal traces and the detected spikes labeled in black dots.

https://doi.org/10.1038/s41592-025-02843-8

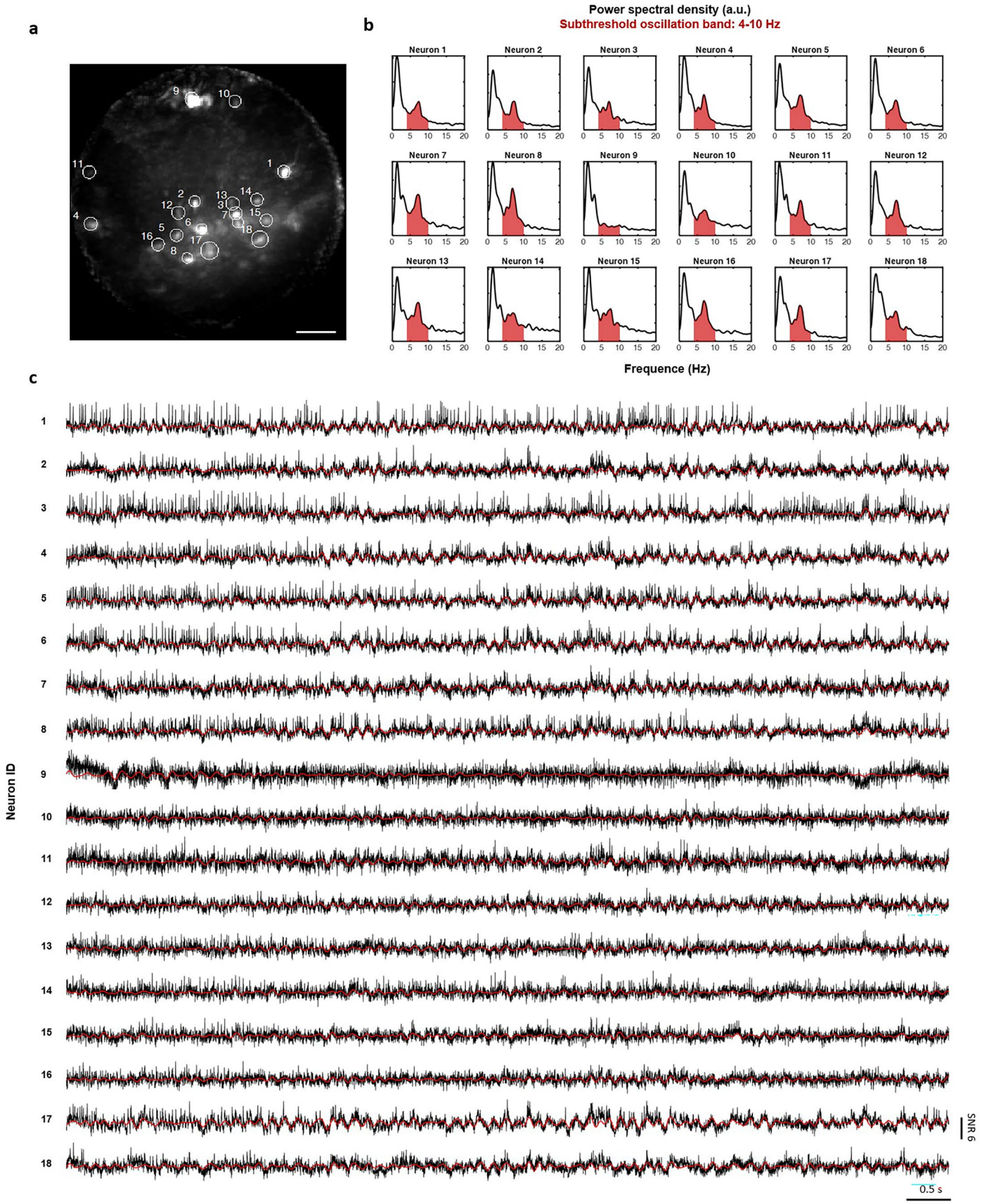

Extended Data Fig. 2 | Observation of subthreshold oscillations in hippocampus interneurons. a. Example MIP of identical dataset used in Fig. 4, with neurons of interest labeled with number. Representative result from nine FOVs conducted using mice labeled for OLM interneurons. Scale bar, 100 µm. **b**. The power spectral densities of 18 neuron traces throughout the entire recording (around three minutes). Red regions denote the frequency band known for theta oscillations. **c**. Raw traces of ten seconds with red lines plot the band-pass filtered signal in 4–10 Hz.

https://doi.org/10.1038/s41592-025-02843-8

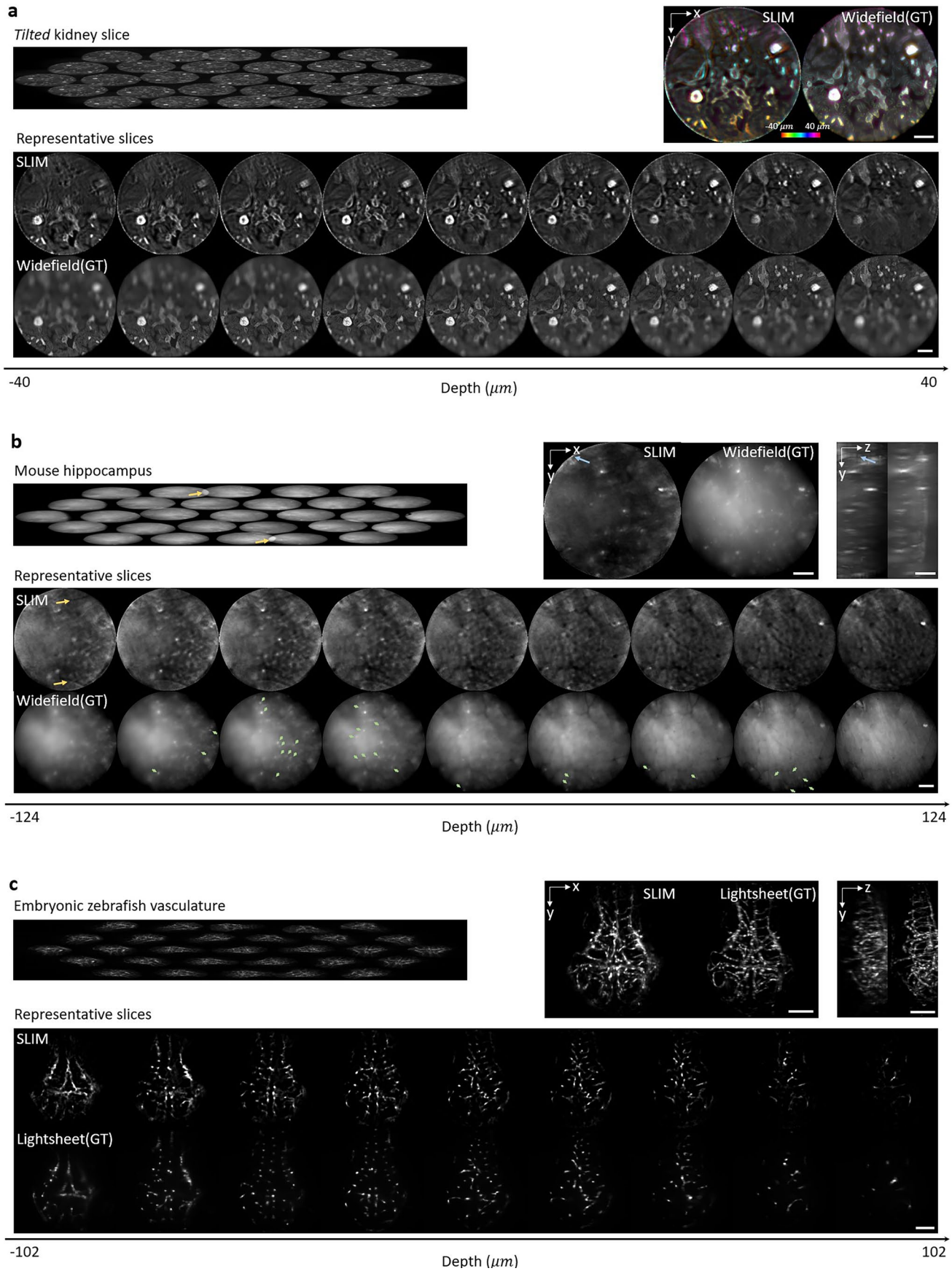

Extended Data Fig. 3 | See next page for caption.

https://doi.org/10.1038/s41592-025-02843-8

Extended Data Fig. 3 | Comparison between SLIM reconstruction and ground truth. High-resolution ground truth images are acquired with a reference camera (sharing same objective with SLIM) under either widefield or light-sheet illumination. Sample is axially scanned with a motorized stage to acquire a z stack. SLIM and ground truth image are acquired sequentially on the same sample. **a**. Tilted mouse kidney slice (FluoCells™ Prepared Slide from ThermoFisher) **b**. Live mouse hippocampus (CA1, excitatory pyramidal neurons). Green arrows denote representative neuron candidates. Yellow arrows mark the overlaps between sub-aperture views (fabrication tolerance of prisms and holder). When sample exhibits a strong background, this overlap could induce reconstruction artefacts. Blue arrows indicate the MIP artifacts due to the bright boundary of circular FOV. **c**. Embryonic zebrafish vasculature (endothelial cells, *Tg(flk:mCherry)*). Scale bar, 100 μm.

nature methods

Supplementary information

https://doi.org/10.1038/s41592-025-02843-8

Kilohertz volumetric imaging of in vivo dynamics using squeezed light field microscopy

In the format provided by the authors and unedited

Content

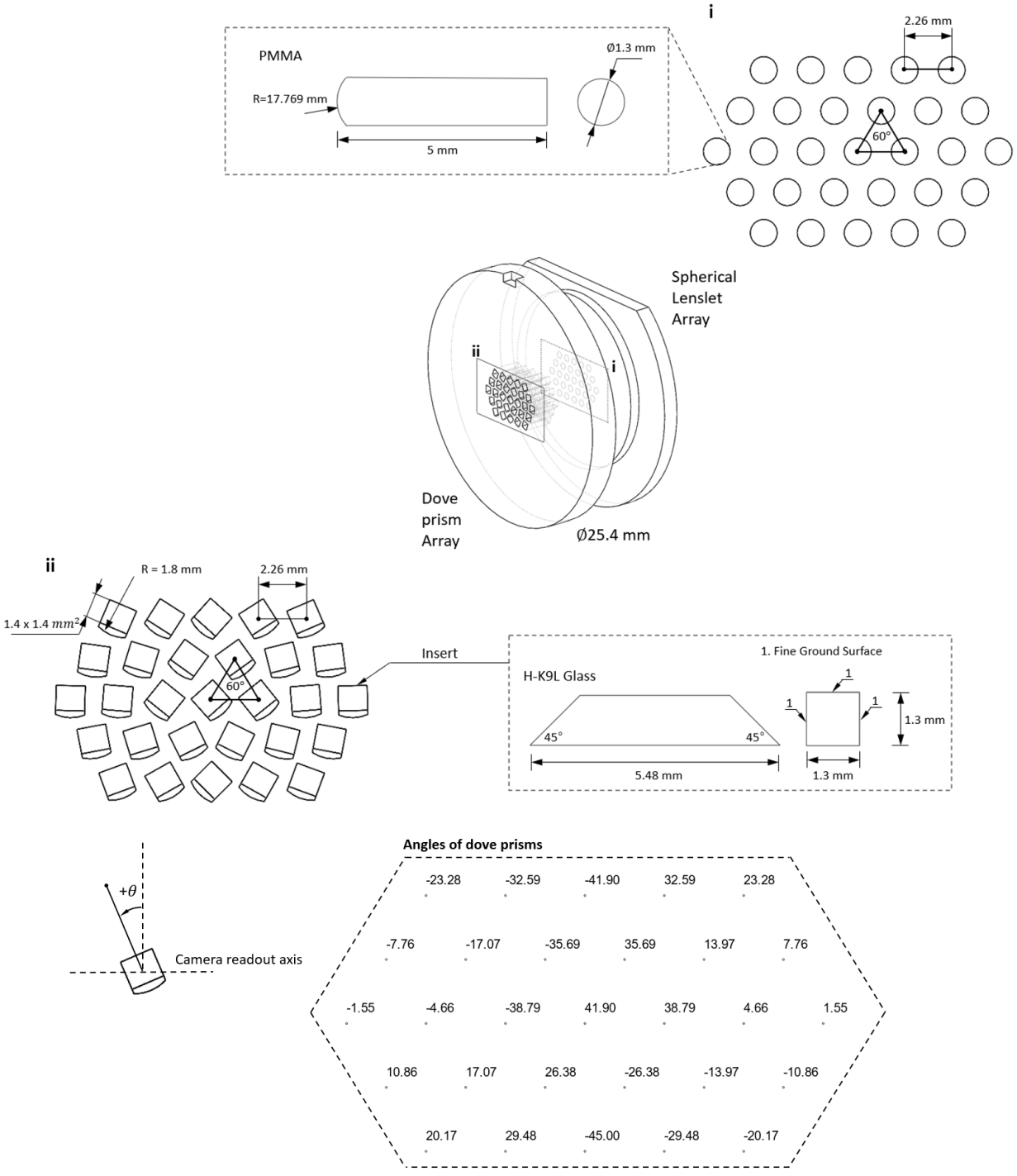

Supplementary Figure 1. Design of lenslet and dove prism array. (**i**) The lenslet array is in-house fabricated on a PMMA substrate. (**ii**) The holder of dove prims, the dove prism, and the angle arrangement of dove prisms.

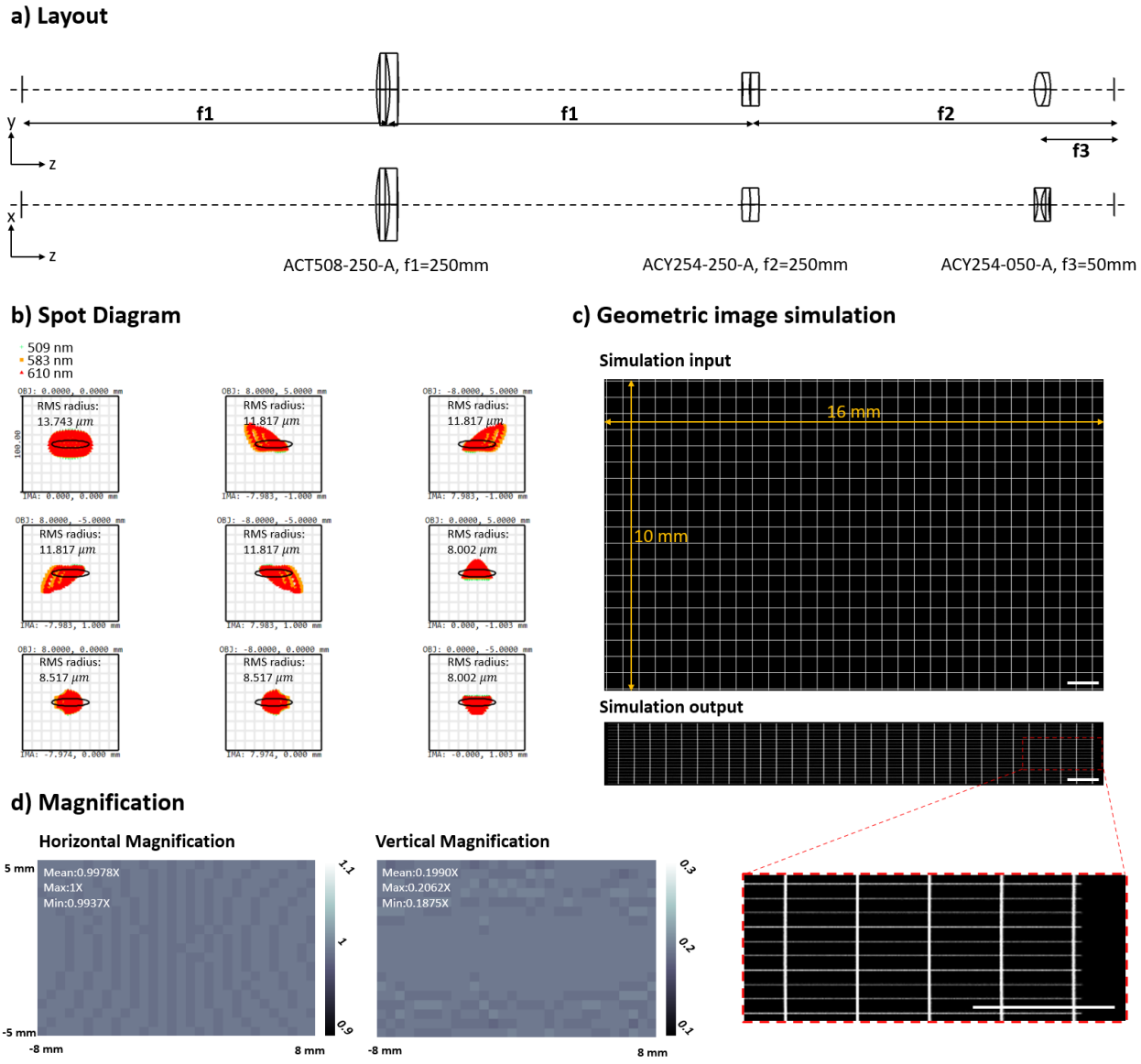

Supplementary Figure 2. Design of anamorphic relay lens. a. Layout of the relay system, consisting of one spherical achromatic doublet and two orthogonally placed cylindrical achromat doublets, where off-the-shelf components (Thorlabs) were used. **b**. Spot diagram shows aberration (within two times the pixel size, 6.5 μm) across the field of view of the lenslet array image (16 mm × 10 mm). **c**. OpticStudio Zemax simulations on an image of a grid. The red dotted box shows the zoom-in picture. Scale bar, 1 mm. **d**. Horizontal and vertical magnification measured from the grid simulation.

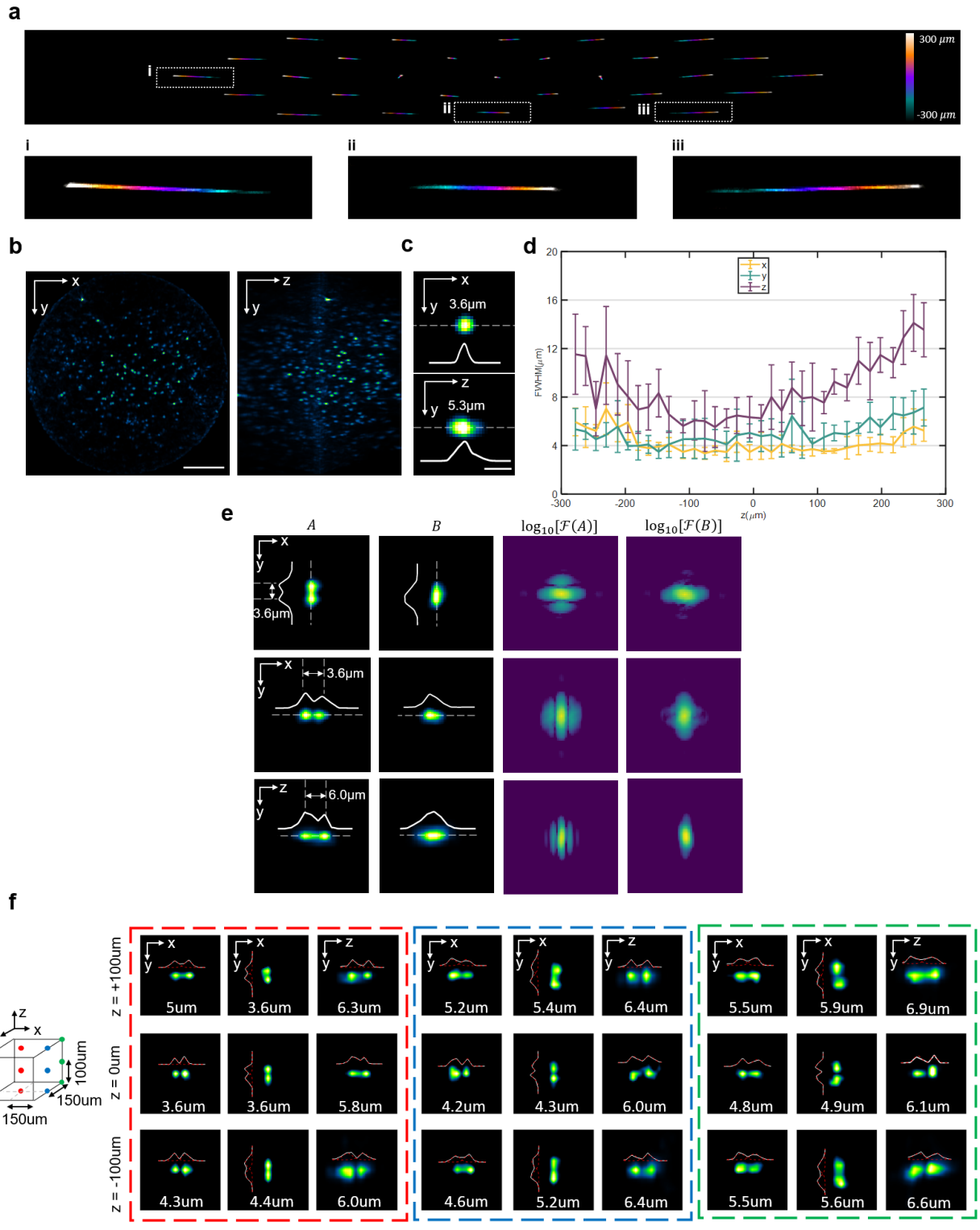

Supplementary Figure 3. Characterization of lateral and axial resolutions of SLIM. a. x-y MIP of the SLIM PSFs with depth color-coded. **b**. fluorescent beads. Scale bar 100 μm. **c**. Individual reconstructed bead in (a) in lateral(x-y) and axial(y-z) dimensions and the corresponding profiles along the dashed lines. Scale bar, 5 μm. **d**.

Average axial (z) and lateral (x,y) FWHM of the beads across the volumes reconstructed by SLIM. Center lines represent means and error bars denote standard deviations. **e**. Analysis of the reconstructed images of two virtually separated beads obtained by SLIM with cross-section profiles along the dashed lines. We imaged the same 1μm bead at two positions, adjusting the interval gradually using a piezo translation stage. By combining the images obtained from these two positions, we created two virtually separated beads with an arbitrary distance. The first and second columns (A and B) are the reconstructed images of resolved beads (A) and unresolved beads (B). The third and fourth columns are the Fourier analysis of the first and second columns using function: $f(x)=\log(|F(x)|)$, where $F(x)$ represents the Fourier transform. **f**. Two virtually separated beads resolution measurements at several different places within the volume. At each lateral location (red, blue, green box), the experiments are repeated at different axial locations (-100, 0, 100 μm). The beads are displaced horizontally, vertically and axially.

a. Selective volume side-illumination setup

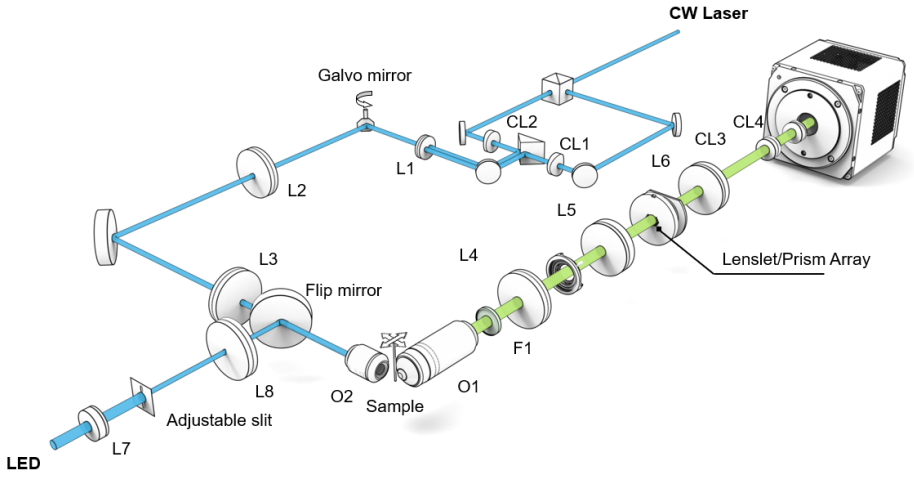

b. Widefield epi-illumination setup

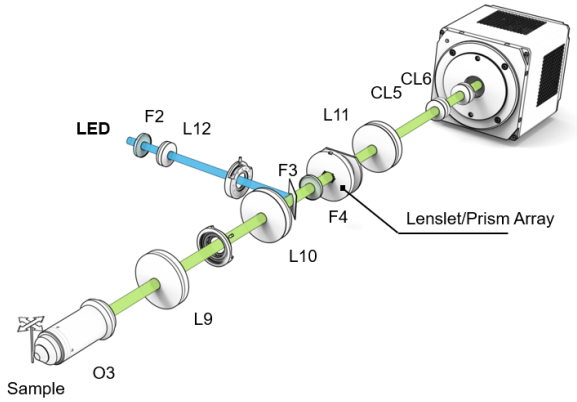

Supplementary Figure 4. Schematics of the SLIM with different illumination systems. L1-L12, lens; CL1-CL6, cylindrical lens. O1-O3, objectives. F1-F4, filters. See **Supplementary Table 3** for details.

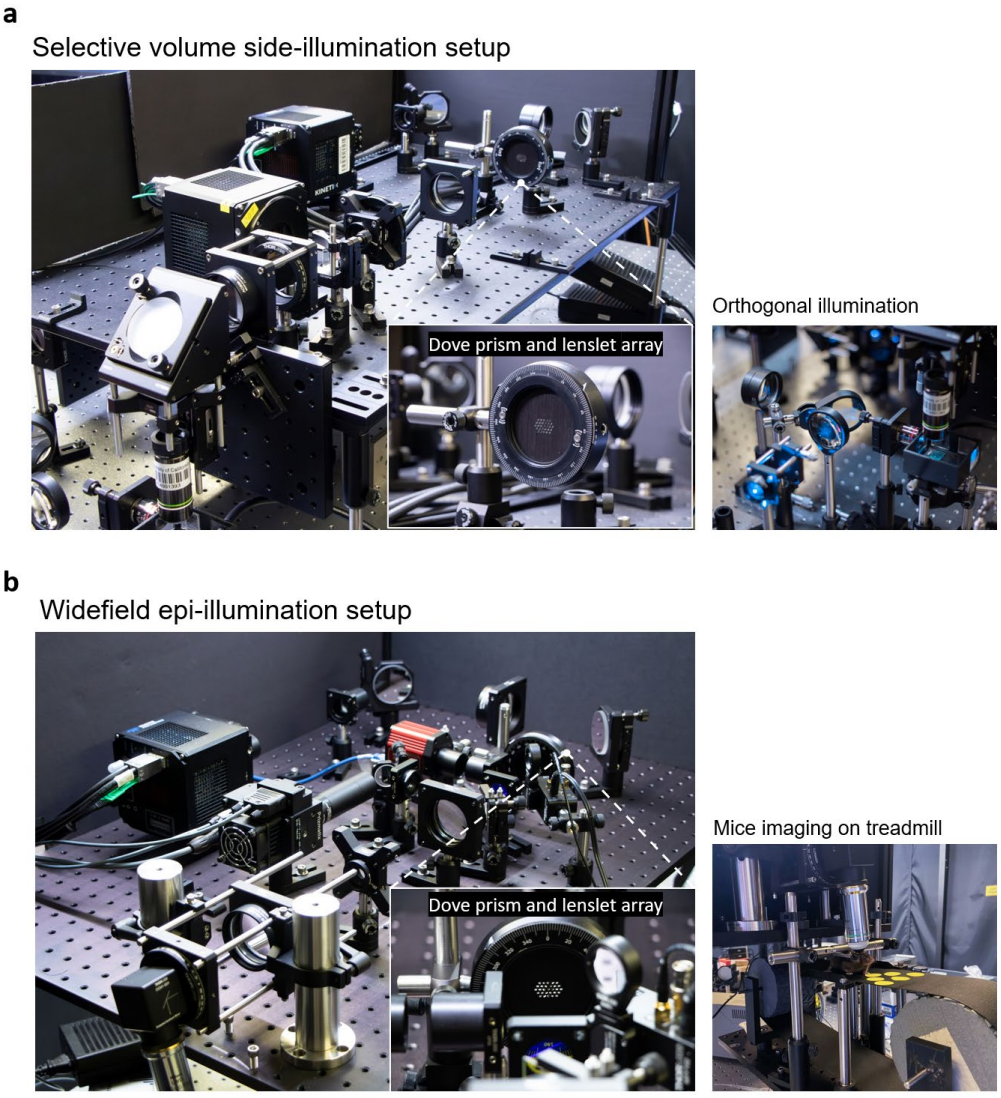

Supplementary Figure 5. Photographs of the setups.

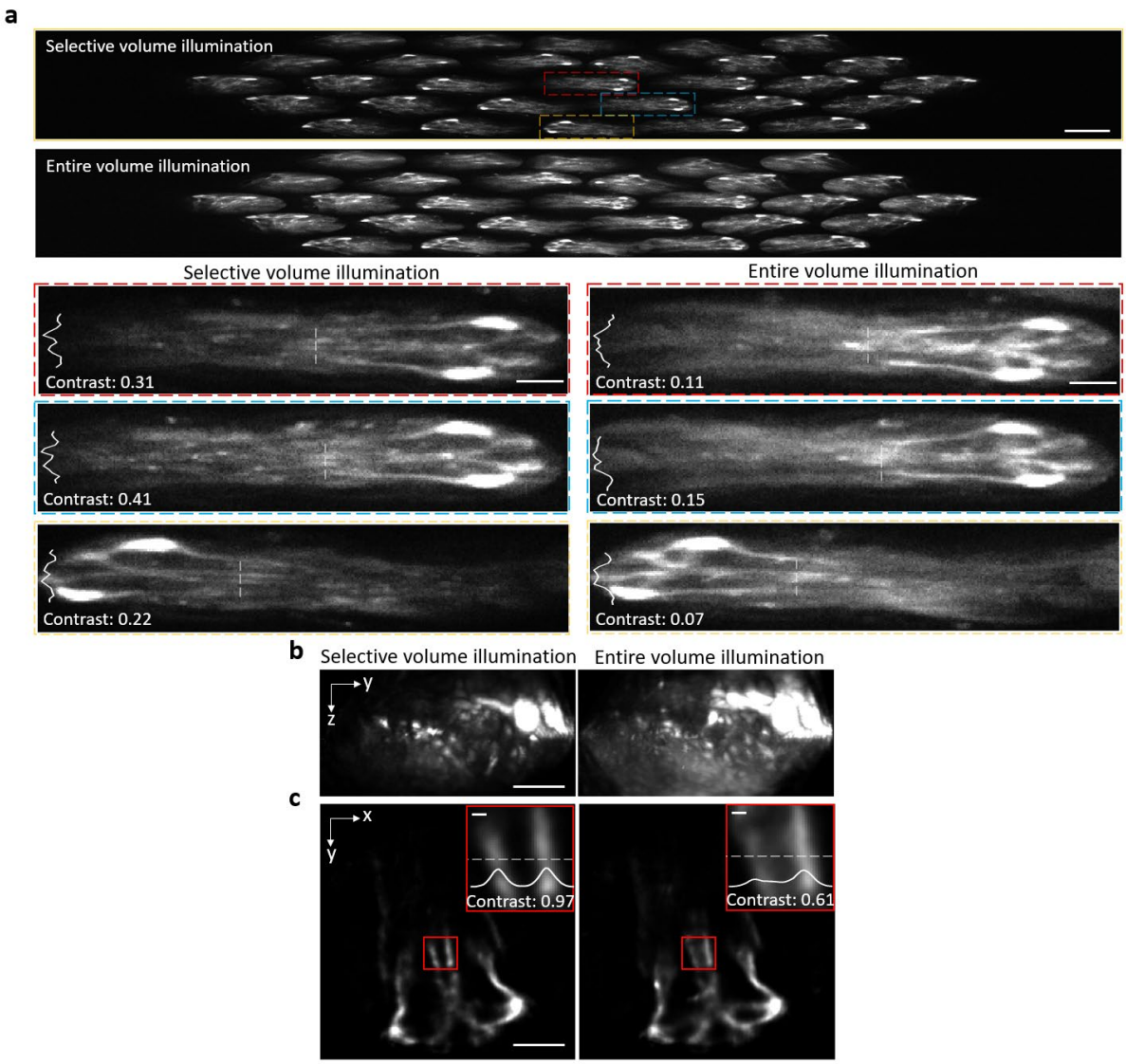

Supplementary Figure 6. Comparisons of image quality of SLIM under different illumination configurations in zebrafish brain. a. Raw measurement of embryonic zebrafish brain under selective volume illumination (1st row) and entire volume illumination (2nd row). Scale bar, 250 μm. The red, blue and orange boxes indicate the zoom-ins of representative views. The line profile contrast is calculated as $(Max - Min)/(Max + Min)$, where Max (Min) is maximum(minimum) value between two peaks. Scale bar, 50 μm. **b.** MIP of SLIM reconstruction for zebrafish brain. Scale bar, 100 μm. **c.** The representative slice of SLIM reconstruction for zebrafish brain. Scale bar, 100 μm. The inset figure shows the zoom-in vascular structure and quantify image quality by line profile contrast. Left: selective volume illumination. Right: entire volume illumination. Scale bar, 10 μm.

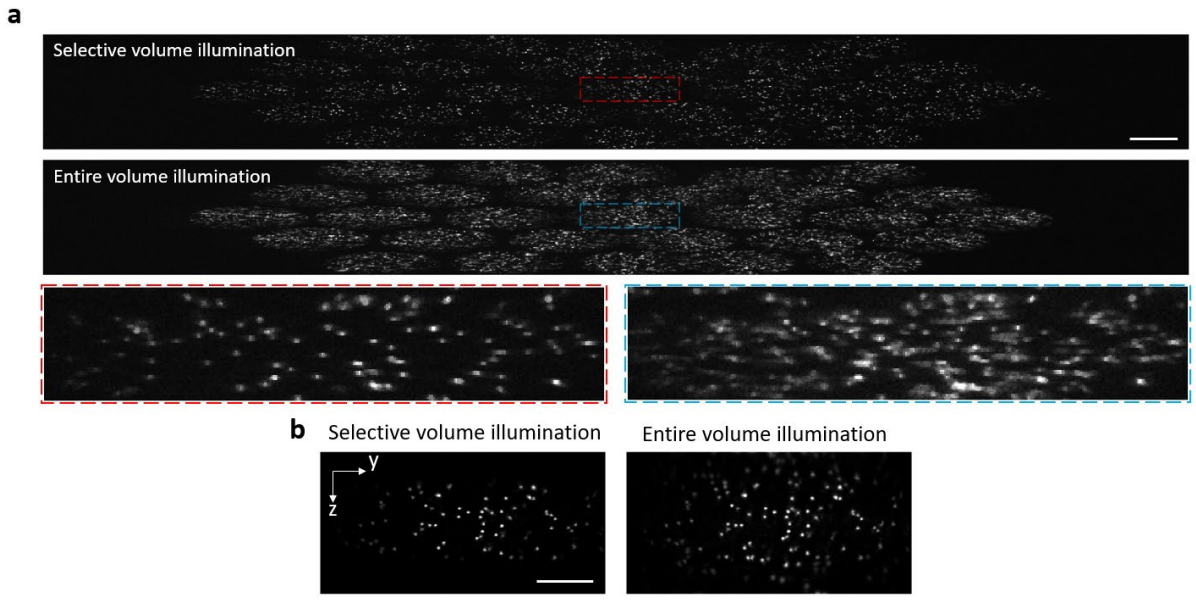

Supplementary Figure 7. Comparisons of image quality of SLIM under different illumination configurations using fluorescent beads. a. Raw measurement of embryonic zebrafish brain under selective volume illumination (1st row) and entire volume illumination (2nd row). The red and blue dashed box indicate the zoom-in of center perspective view. Scale bar, 250 μm. **b.** MIP of SLIM reconstruction of fluorescent beads. Scale bar, 100 μm.

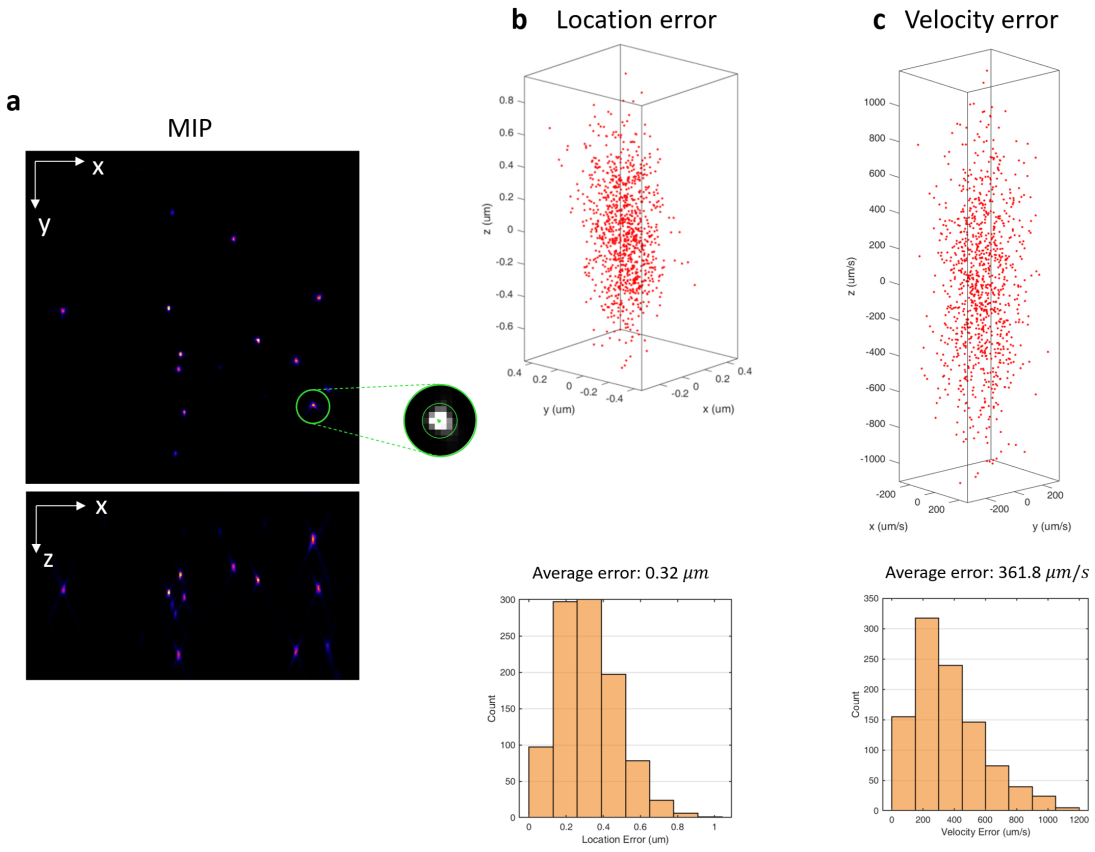

Supplementary Figure 8. Tracking errors quantified by imaging static fluorescent beads at 1,000 vps. a. x-y and x-z MIPs of the reconstruction of the example frame. Beads are assumed to be stationary, and the tracking error is indicated by the tracking difference among different frames (n=1000). These sub-pixel errors potentially come from the reconstruction and tracking algorithms and environment vibration. **b.** Localization variation. Each red dot plots the relative position of the tracking position of one frame to the average position across all frames. **c.** Velocity error caused by the location variation in adjacent frames. The histograms plot the distribution of the Euclidean distance of the error vector.

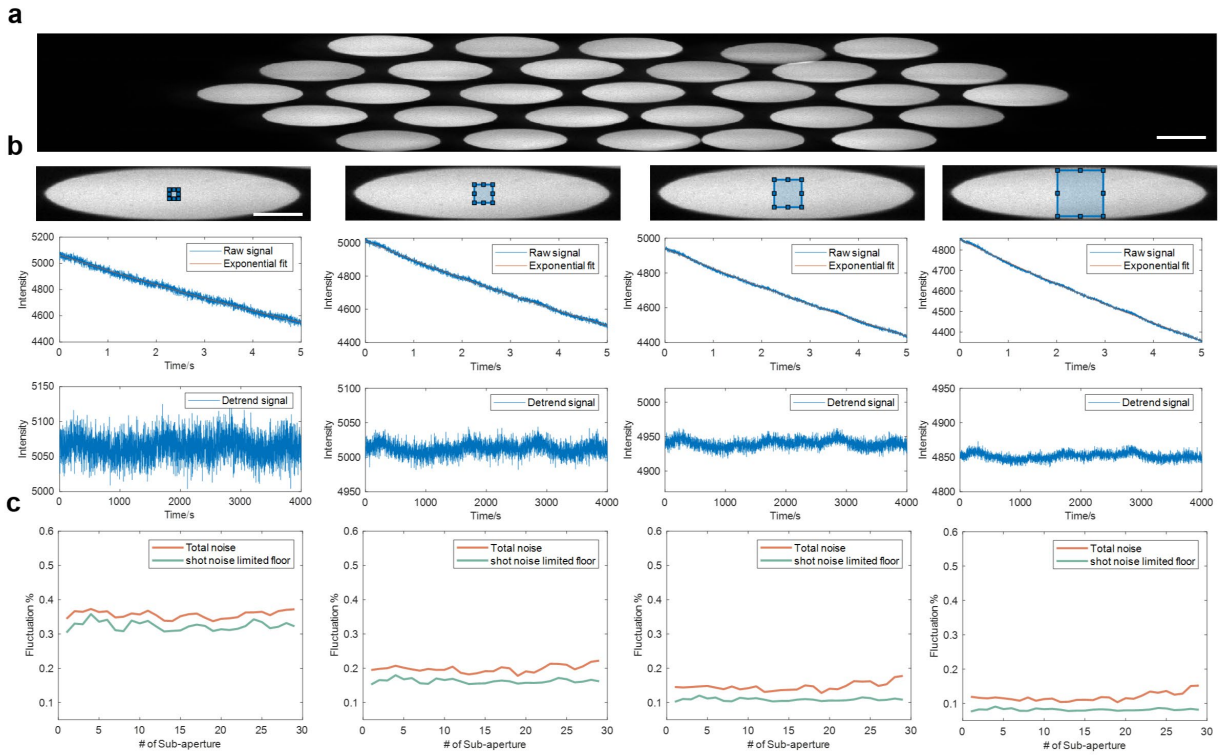

Supplementary Figure 9. Noise characterization in ultra-low-noise LED illumination. a. Raw image of reference fluorescence dye. Scale bar 200 μm. **b.** Central sub-aperture images with various regions of interest (10*10, 20*20, 30*30, 50*50), and the corresponding average time series signal. Scale bar, 100 μm. We assume that the signal of fluorescent dye is uniform across the entire field of view. Photobleaching is observed and detrended by exponential fitting. Both total signal noise $Mean(signal)/std(signal)$ and shot noise $\sqrt{number\ of\ pixel}/\sqrt{Mean(signal)}$ is calculated for different size of ROI. (0.35%/0.31%, 0.19%/0.16%, 0.13%/0.10%, 0.09%/0.064%) **c.** All 29 sub-aperture images with various regions of interest (10*10, 20*20, 30*30, 50*50), and the corresponding fluctuation percentage.

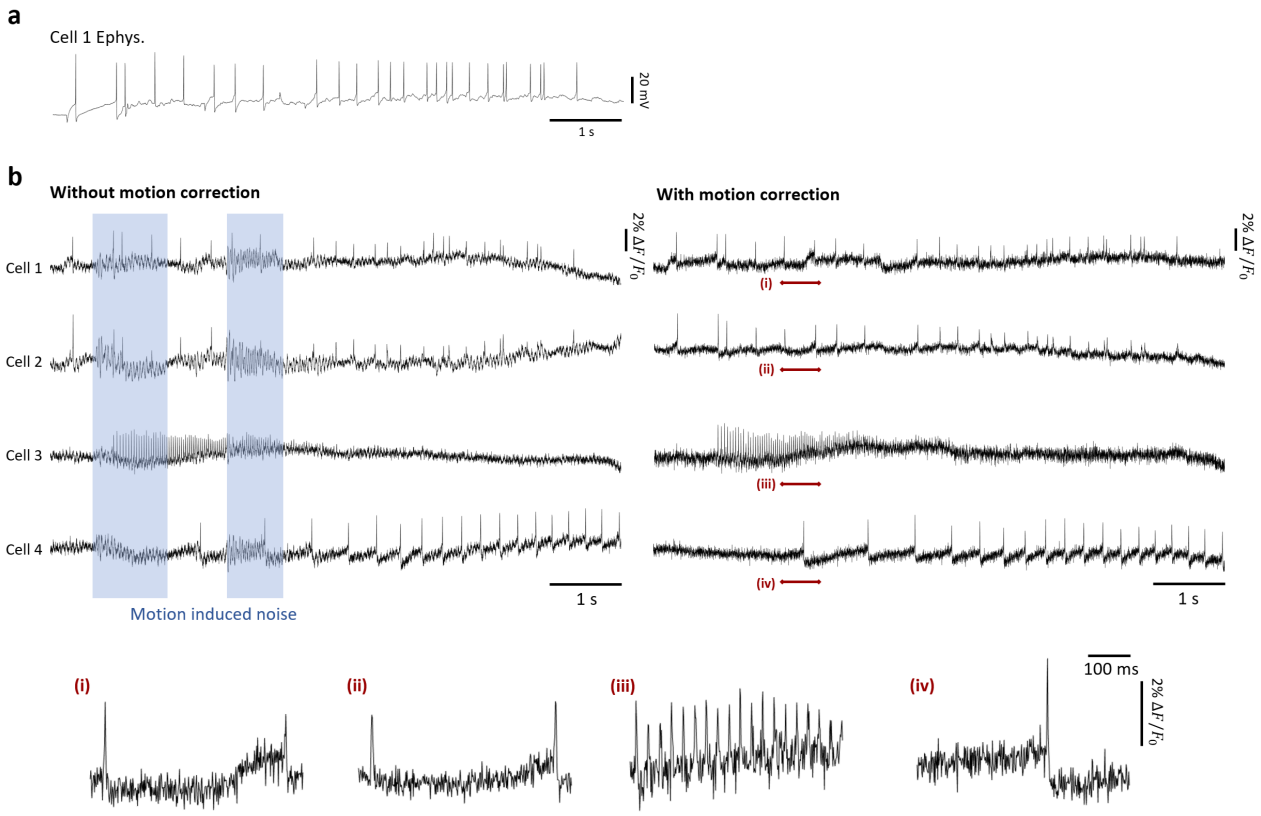

Supplementary Figure 10. Image motion correction for optical recording of membrane action potentials in leech. a. The ground-truth electrophysiological signal provided by electrode on cell 1. **b**. By assuming the sample being static during recording, motion correction has been applied to the image sequence by image registration between adjacent frames. With motion correction, the noise induced by sample/environment vibration can be suppressed. The blue boxes label the example time window when such noise appears severely and affects the detection of voltage spikes. (i-iv) Zoom-in of signal segments labeled by red lines.

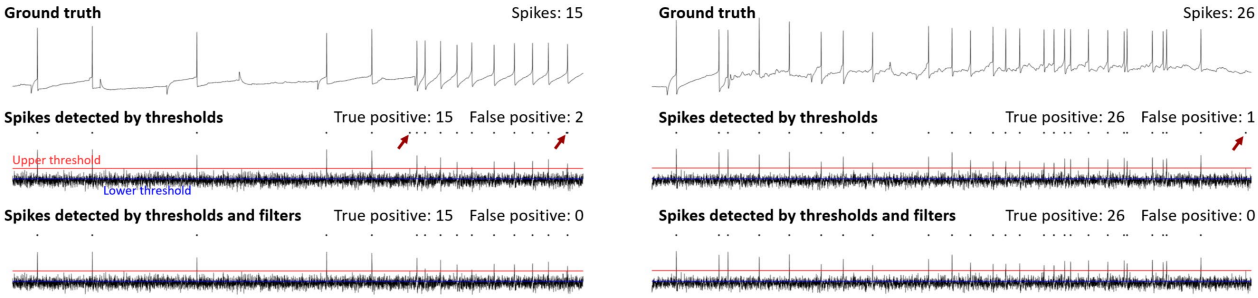

Supplementary Figure 11. Spike detection in leech ganglion. We applied a threshold method (i.e. a Schmitt trigger) to the detrended signal. The upper and lower thresholds were empirically chosen to be 3σ and $\sigma/3$, where σ is the standard deviation of the signal. After we further filtered out false positives by removing spike candidates with duration of only one time point, we achieved high accuracy detecting all action potentials in the electrophysiological ground truth. Above presents two examples of the detection process.

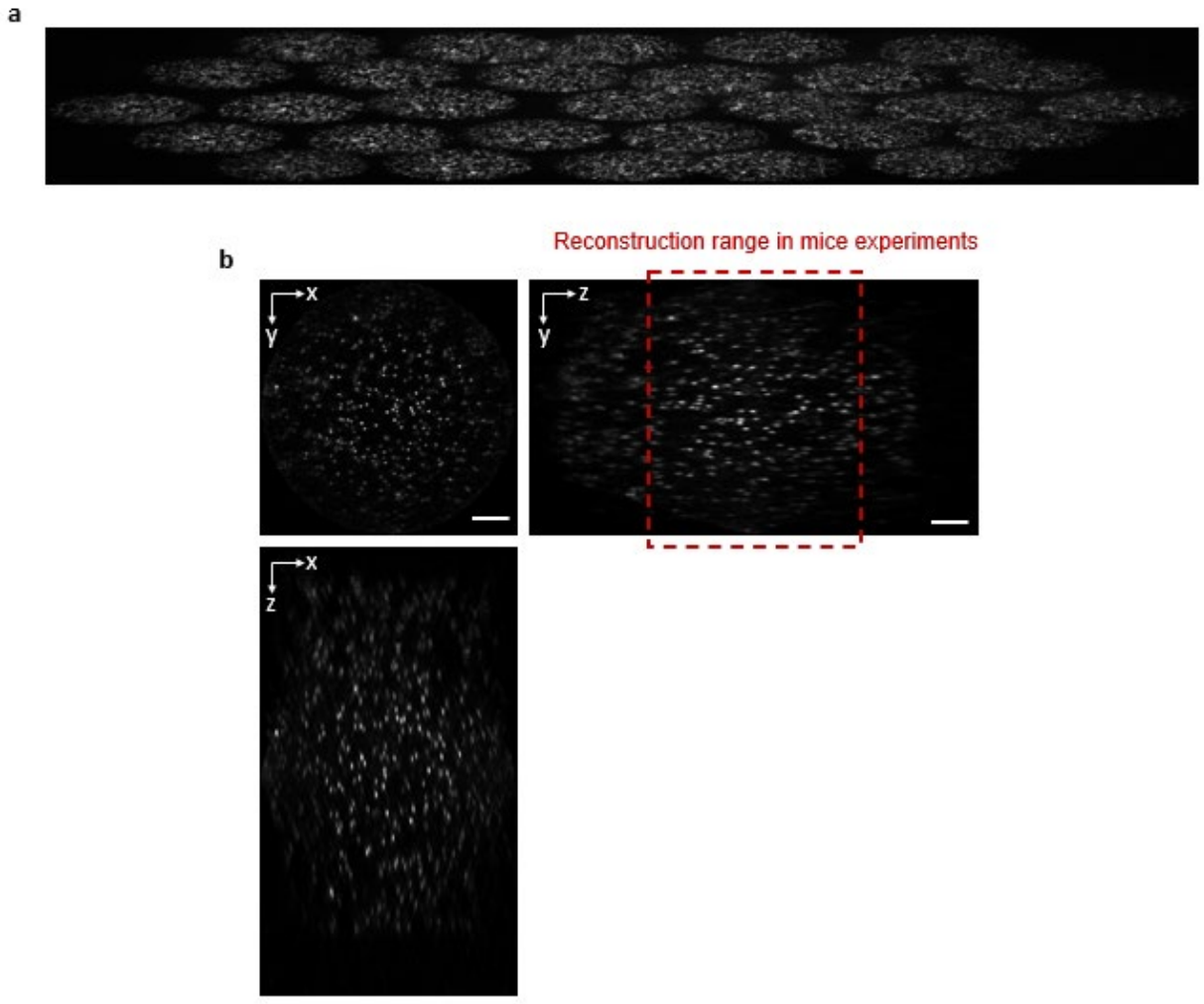

Supplementary Figure 12. Fluorescent beads under mouse imaging setup. a. Raw measurement. ROI is configured to be 330 × 2400 pixels to fit 29 sub-aperture images (each 61 × 305 pixels). **b**. The reconstruction result (305 × 305 × 151 pixels, FOV Ø 688 × 1204 μm) of measurement in **a**. The red dotted box indicated the depth range (-296 ~ 296 μm) used in mouse imaging experiments. Scale bar, 100 μm.

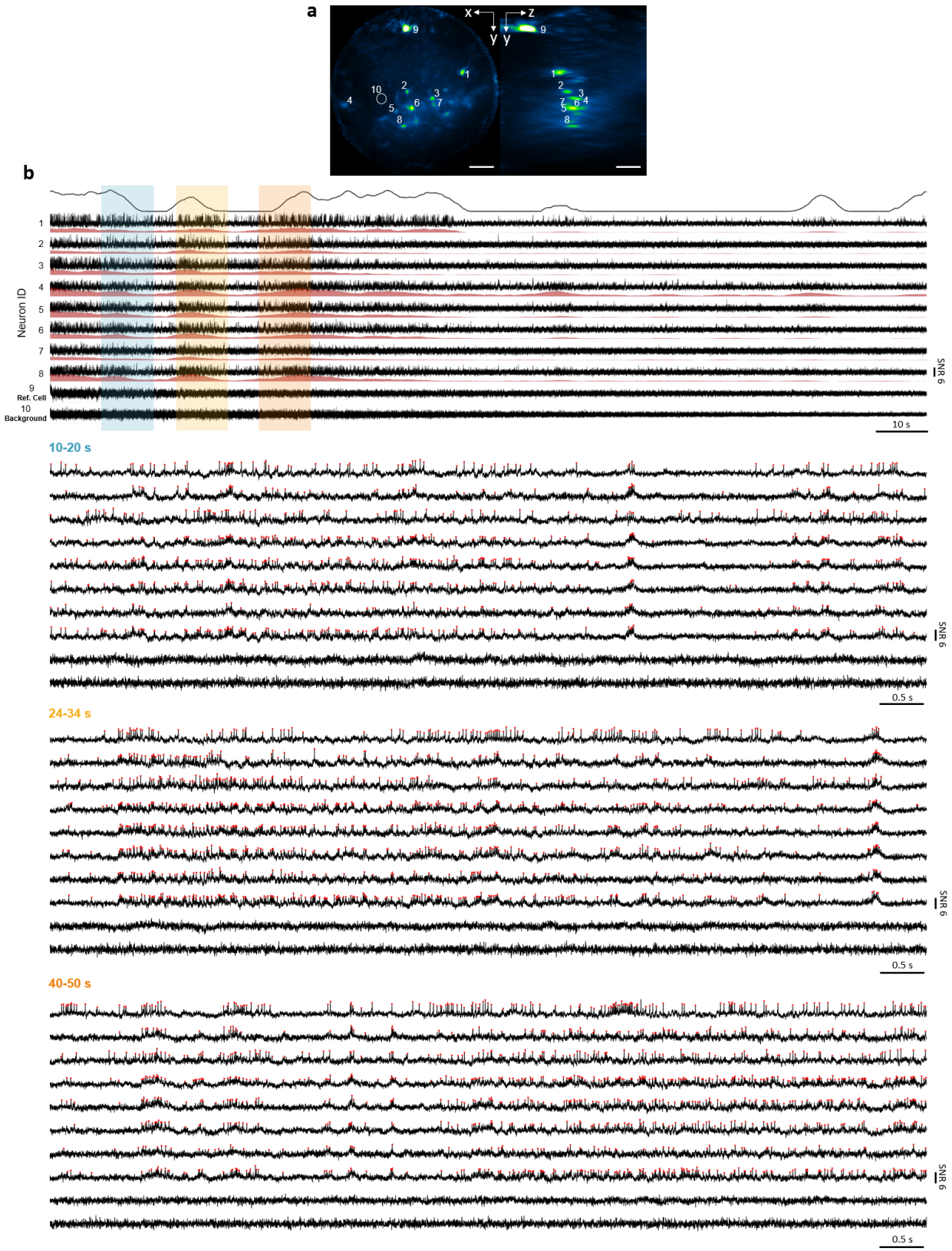

Supplementary Figure 13. Zoom-in views of different time windows of data presented in Fig. 4. Traces 9 and 10 are an inactive neuron and a background measurement, respectively, to confirm the fidelity of other traces.

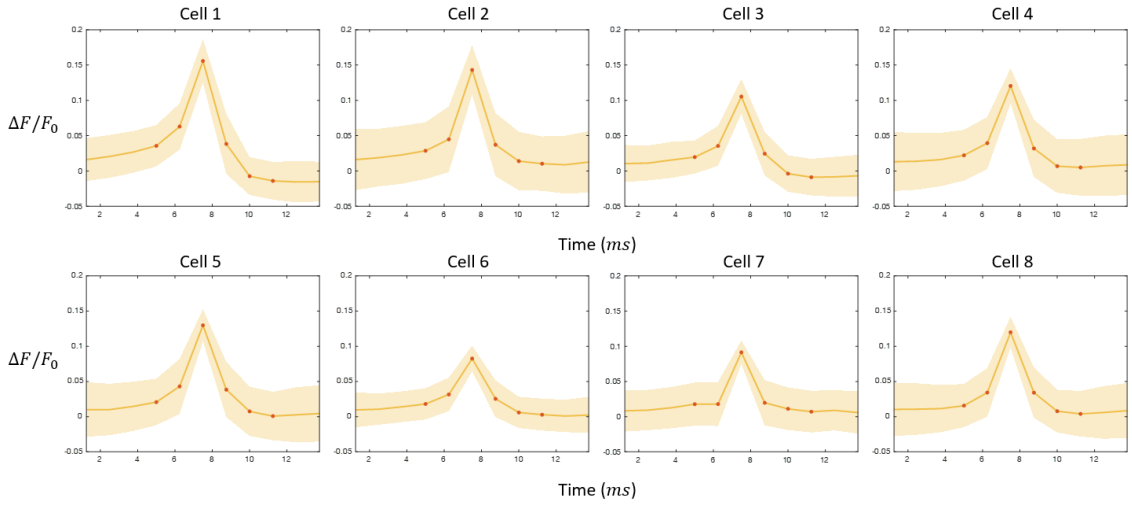

Supplementary Figure 14. Average spike waveforms for neurons demonstrated in Fig. 4. Interval between sampling points (orange) is 1.25 ms.

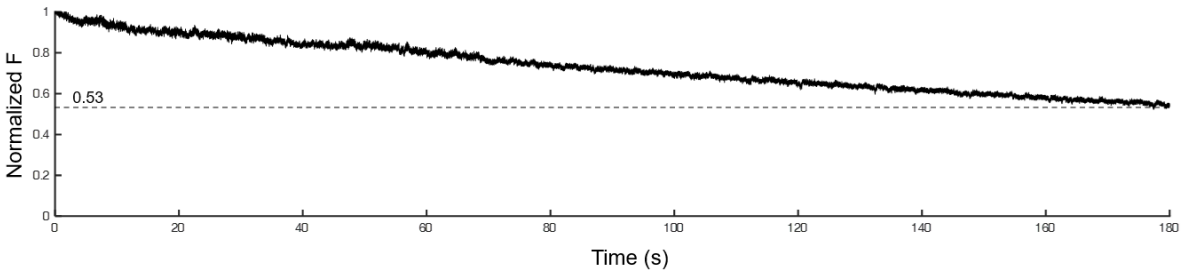

Supplementary Figure 15. Representative pAce fluorescence photobleaching during 180s continuous SLIM imaging. The illumination power on sample is measured to be 36mW/mm^2.

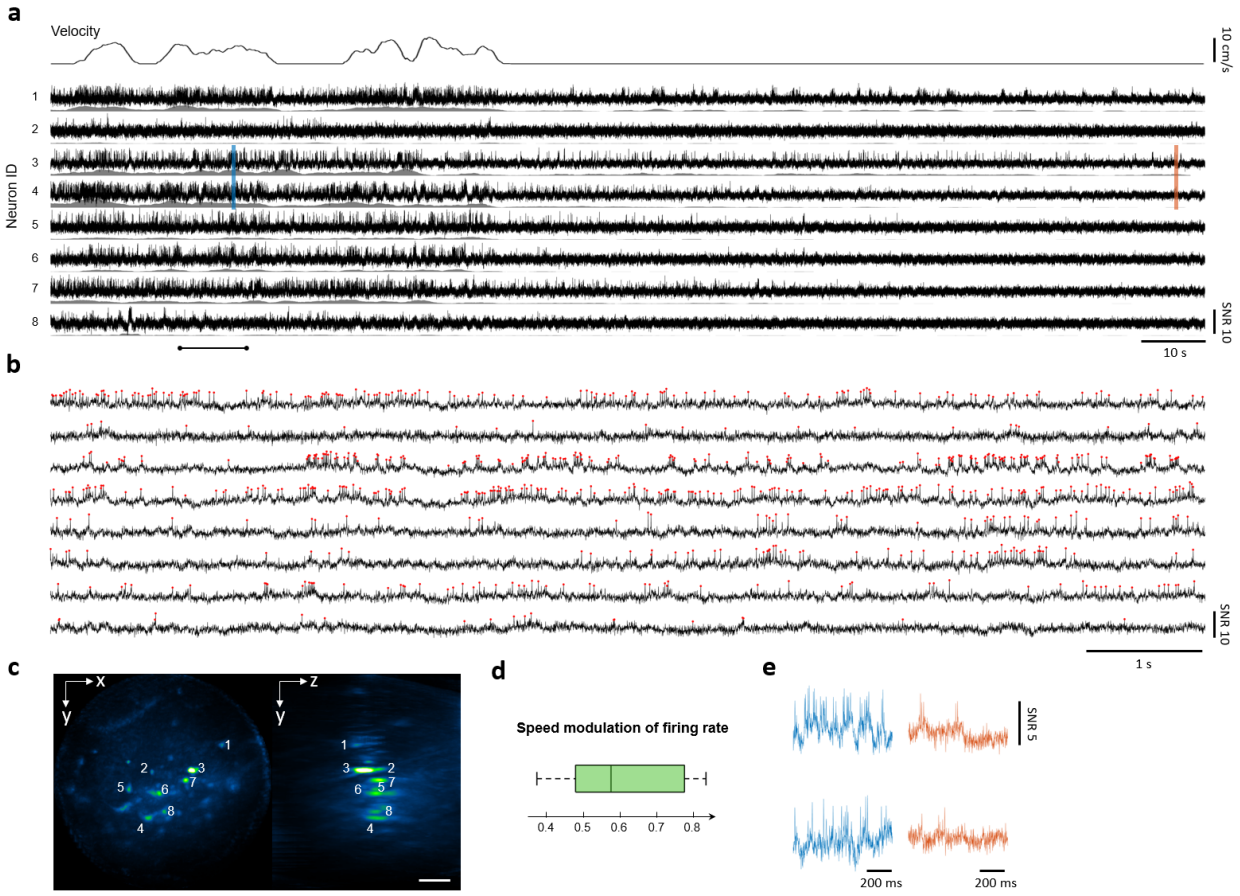

Supplementary Figure 16. 3D voltage imaging of hippocampus in behaving mice at 800 vps. Another trial of continuous imaging across 180s while animal runs on treadmill, verifying the findings on speed modulation of neuron firing rate in Fig. 4. **a.** Detrended fluorescent signal traces with firing rate. **b.** The zooms in on the window (20 – 30s) in **a**.The red dots denote the detected spikes. **c.** 3D MIP of SLIM reconstruction. Scale bar, 100 μm. **d.** Pearson correlation coefficients between animal velocity and firing rate of neurons shown in panel a (n=8). **e.** Representative signal traces in the blue and orange windows in **a.** Box plots display the median (center line) with upper and lower quartiles (box limits); whiskers represent 1.5× interquartile range, and individual data points represent one sample.

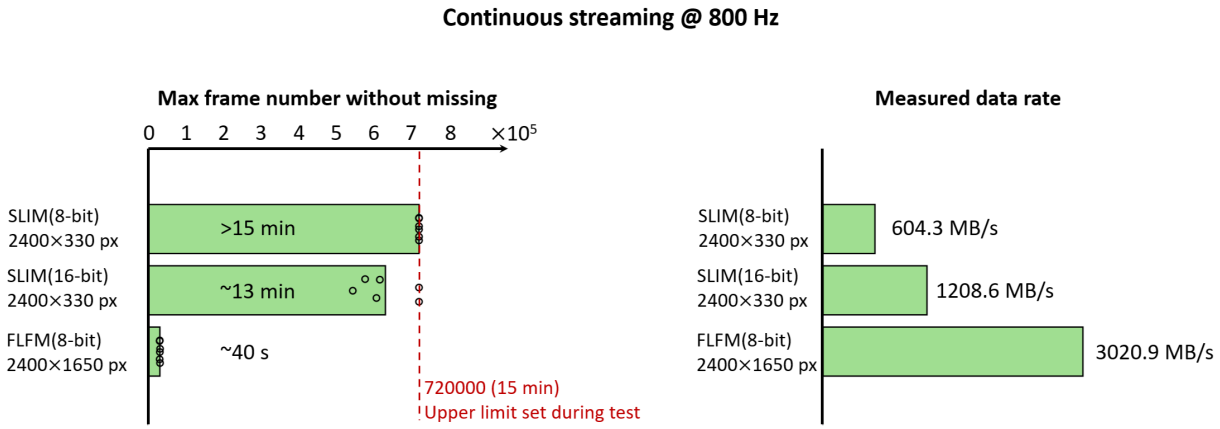

Supplementary Figure 17. SLIM reduces data bandwidth required for continuous high-speed volumetric imaging. Continuous streaming at 800 Hz under different camera modes (6 trials for each) have been performed. Bar graphs plot the mean values of maximal frame numbers without missing for each mode, while black dots denote the individual data points of each trial. Recording with unsqueezed frame (2400×1650 px) at 16-bit cannot achieve 800 Hz and thus has not been included. Smaller camera frame and lower bitdepth both contribute to a longer recording duration without frame missing. Note that an upper limit (720,000 frames, 15 min) was set during experiments due to disk storage space. Since the data rate of squeezed frame (2400×330 px) at 8-bit is below the maximal disk writing speed, it has not filled up the RAM buffer at all and can theoretically stream for longer than 15 min. Data rates required for continuous streaming for each mode were measured from camera software. The benchmark above has been performed on a workstation with 96 GB RAM and four SSDs (Samsung 970 Pro 1TB) in RAID-0 configuration via a controller (HighPoint SSD7101A-1).

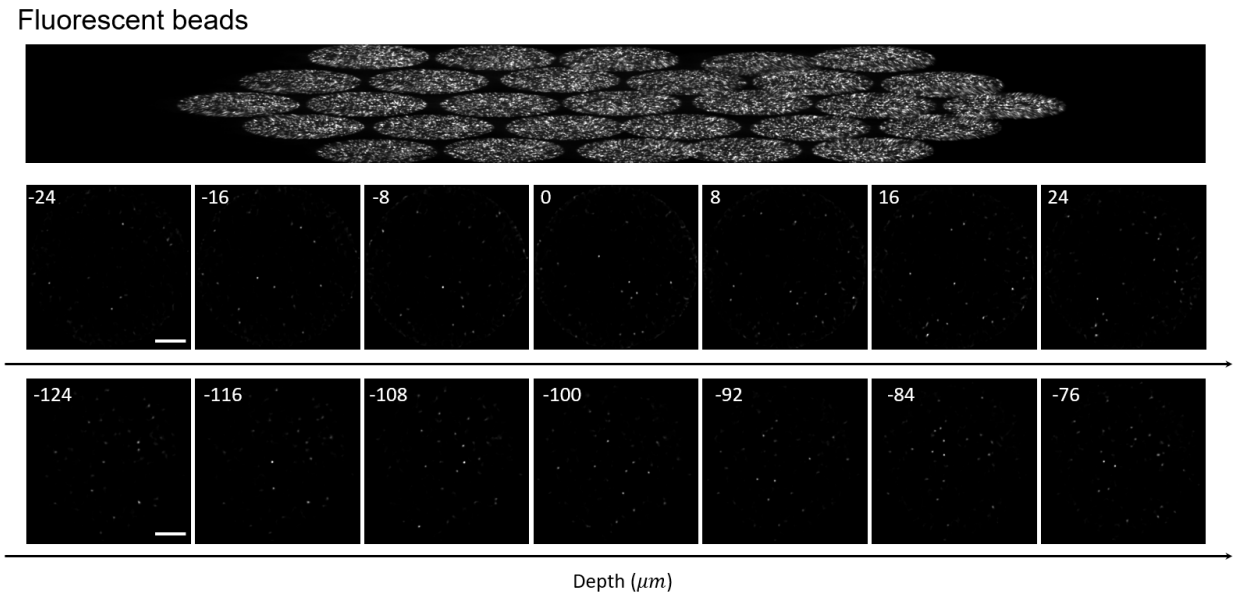

Supplementary Figure 18. Raw and reconstruction slices of representative samples.

Supplementary Note 1

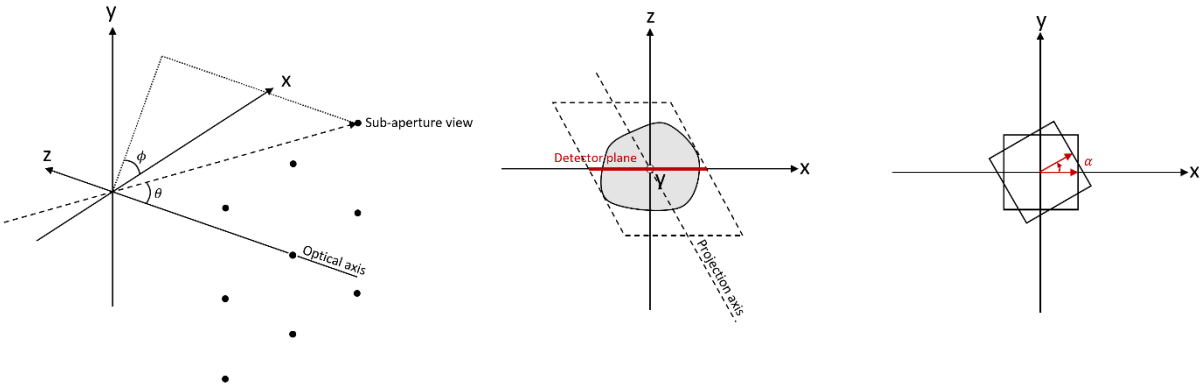

In this note, we model each sub-aperture image in SLIM/Fourier LFM as a parallel projection along the line of sight at the sub-aperture's view angle θ and ϕ. However, in contrast to classical tomographic system where detector rotates with scanner, there's an oblique angle between projection axis and detector plane. Following Fourier slice theorem, we attempt to find the mapping between the spectrum of 2D SLIM image and the 3D spectrum of the object.

For a 3D distributed signal $f(x, y, z)$, the 2D sub-aperture view $I(x, y)$ is:

$$I(x, y) = \int_z f(x - z\ tan\theta\ cos\phi, y - z\ tan\theta\ sin\phi, z)\, dz$$

Meanwhile, the coordinate transformation introduced by the in-plane rotation is:

$$\begin{bmatrix} x' \\ y' \end{bmatrix} = \begin{bmatrix} cos\alpha & -sin\alpha \\ sin\alpha & cos\alpha \end{bmatrix} \begin{bmatrix} x \\ y \end{bmatrix}$$

$$f'(x', y', z') = f(x, y, z) = f(x'\ cos\alpha + y'\ sin\alpha, -x'\ sin\alpha + y'\ cos\alpha, z')$$

The 2D Fourier transformation of the in-plane rotated projection $I'(x', y')$ is:

$$\begin{aligned} \mathcal{F}\{I'(x', y')\} &= \iint_{x', y'} I'(x', y')\, e^{-i2\pi(u'x' + v'y')}\, dx'\, dy' \\ &= \iint_{x', y'} \int_{z'} f'(x' - z'\ tan\theta\ cos\phi, y' - z'\ tan\theta\ sin\phi, z')\, dz'\, e^{-i2\pi(u'x' + v'y')}\, dx'\, dy' \\ &= \iint_{x', y'} \int_{z} f(x'\ cos\alpha + y'\ sin\alpha - z'\ tan\theta\ cos\phi, -x'\ sin\alpha + y'\ cos\alpha - z'\ tan\theta\ sin\phi, z')\, dz' \\ &\qquad e^{-i2\pi(u'x' + v'y')}\, dx'\, dy' \end{aligned}$$

Let

$$x = x'\,cos\alpha + y'\,sin\alpha - z'\,tan\theta\,cos\phi$$
$$y = -x'\,sin\alpha + y'\,cos\alpha - z'\,tan\theta\,sin\phi$$
$$z = z'$$

Then

$$x' = xcos\alpha - ysin\alpha + ztan\theta cos(\alpha + \phi)$$
$$y' = xsin\alpha + ycos\alpha + ztan\theta sin(\alpha + \phi)$$
$$z' = z$$

The Jacobian of the x, y coordinate transformation is:

$$J(x,y) = \begin{vmatrix} \frac{\partial x'}{\partial x} & \frac{\partial x'}{\partial y} \\ \frac{\partial y'}{\partial x} & \frac{\partial y'}{\partial y} \end{vmatrix} = \begin{vmatrix} cos\alpha & -sin\alpha \\ sin\alpha & cos\alpha \end{vmatrix} = 1$$

Therefore, we can rewrite the 2D Fourier transformation as:

$$\begin{aligned} \mathcal{F}\{I'(x',y')\} &= \iint_{x,y} \int_{z} f(x,y,z)\,dz \\ &\quad e^{-i2\pi\{u'xcos\alpha - u'ysin\alpha + u'ztan\theta cos(\alpha+\phi) + v'xsin\alpha + v'ycos\alpha + v'ztan\theta sin(\alpha+\phi)\}} J(x,y)\,dx\,dy \\ &= \iiint_{x,y,z} f(x,y,z) e^{-i2\pi\{u'xcos\alpha - u'ysin\alpha + u'ztan\theta cos(\alpha+\phi) + v'xsin\alpha + v'ycos\alpha + v'ztan\theta sin(\alpha+\phi)\}}\,dx\,dy\,dz \\ &= \iiint_{x,y,z} f(x,y,z) e^{-i2\pi\{ux+vy+wz\}}\,dx\,dy\,dz \end{aligned}$$

where

$$u = u'cos\alpha + v'sin\alpha$$
$$v = -u'sin\alpha + v'cos\alpha$$
$$w = u'tan\theta cos(\alpha + \phi) + v'tan\theta sin(\alpha + \phi)$$

Note that it has the same form of 3D Fourier transformation of $f(x,y,z)$:

$$\mathcal{F}\{f(x,y,z)\} = \iiint_{x,y,z} f(x,y,z) e^{-i2\pi\{ux+vy+wz\}}\,dx\,dy\,dz$$

With the coordinate transformation between u, v, w and u', v', w' we can map the 2D spectrum of projection $I'(x', y')$ to the 3D Fourier space of $f(x, y, z)$ and reveal the 3D frequency components that are retrievable from the 2D measurement. We assume that the squeezed measurement undersamples the sub-aperture image in one dimension and thus delivers an elliptical transfer function (with long axis in u' and short axis in v' direction). According to the coordinate transformation, we would pursue $\alpha + \phi$ to be zero in order to maximize the axial cutoff frequency, which indicates that the in-plane rotation angle should be chosen in attempt to align the disparity shift horizontally (x' axis, camera rows). For example, the following figure shows how the aforementioned coordinate transformation applies to a sub-aperture view in our design ($\theta = 24.35°, \phi = -60°, \alpha = 58.97°$). The 2D elliptical spectrum pursues the w direction in the 3D Fourier space with its long axis.

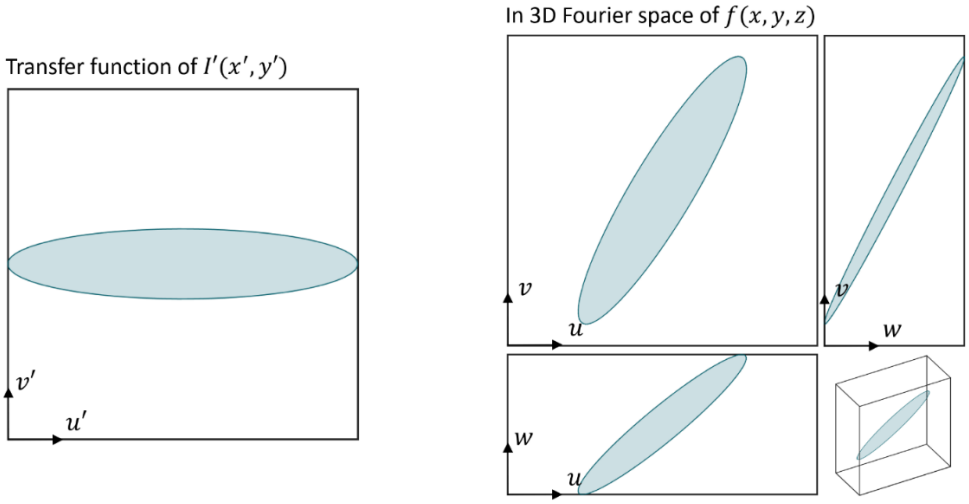

The effect of different strategies in angle selection can also be visualized in space domain. The figure below shows x-y MIP of simulated SLIM PSF. By examining the lateral shift induced by axial translation, we can infer the axial resolving capability. Strategy 1 allows the lateral shift to align with camera rows where we have full digital sampling power, in contrast to strategy 2 that does the opposite. We should note that these selection strategies cannot be exactly achieved since the entire angle set is uniformly distributed in 180 degrees.

Strategy 1: Pursue $\alpha + \phi = 0$

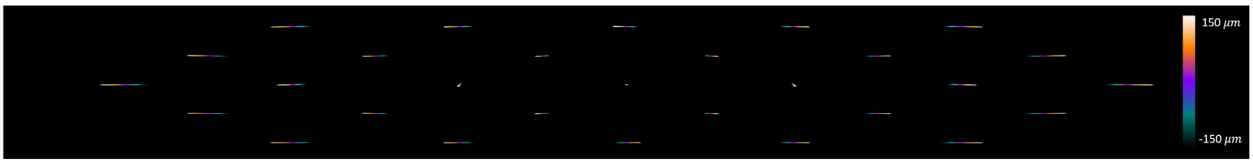

Strategy 2: Pursue $\alpha + \phi = \pi/2$

Supplementary Note 2 Pseudocode of SLIM reconstruction algorithm

Algorithm SLIM reconstruction using Richardson Lucy deconvolution

$s,\ \theta(N_v),\ PSF(N_x, sN_y, N_z, N_v),\ im(N_x, sN_y, N_v)$

▷ Input squeezing factor s, rotation angle θ , normalized PSF, and measured light field views im

$vol^0(N_x, N_y, N_z) = vol_{init}$ ▷ Initialize volume

for iterations **do**

  $\overline{im} =$ FP(vol^k) ▷ Forward project the current volume estimation

  vol^{k+1}=$vol^k \cdot$ BP$(im/\overline{im})$ ▷ Backward project the error and update volume

end for

function FP(vol) ▷ Forward project the volume of dimensions N_x, N_y, N_z

  Initialize $im = zeros(N_x, s \cdot N_y, N_v)$

  for each v in N_v **do**

    Apply in-plane rotation ($\theta(v)$) to entire vol

    Resize image at scale s in direction y for entire vol

    Slice-by-slice convolution between resized vol and $PSF(:,:,:,v)$

    $im(:,:,v) =$ Sum along depth of the convolution result

  end for

  return im

end function

function BP(im) ▷ Backward project the light field views of dimensions $N_x, s \cdot N_y, N_v$

  Initialize $vol = zeros(N_x, N_y, N_z)$

  for each v and d in N_v and N_z **do**

    $PSF^T(:,:,d,v) =$ rotate $PSF(:,:,d,v)$ at 180 degrees

  end for

  for each d in N_z **do**

    View-by-view convolution between im and $PSF^T(:,:,d,:)$

    Resize convoluted views at scale $1/s$ in direction y

    Apply in-plane rotation to each view at corresponding angle $-\theta(v)$

    $vol(:,:,d)$ = Sum along view of rotated results

  end for

  return vol

end function

Supplementary Note 3

In this note, we present a series of simulations designed to evaluate the limitation and trade-off of our proposed SLIM system. It examines the quality of reconstruction and the assumption on sample signal sparsity. It also compares SLIMs against Fourier LFM (FLFM) and between various design parameters including number of sub-aperture images and vertical scaling ratios.

The 3D PSF of FLFM was first simulated following the method presented in Guo, C, et al.[1]. It was then cropped based on the lenslet position, with each patch being the 3D PSF of the sub-aperture. After calculating and assigning optimal angles (**Supplementary Note 1**), we applied in-plane rotation and then vertical scaling to obtain SLIM sub-aperture PSFs.

To synthesize corresponding SLIM measurement, we first collected ground truth (GT) 3D images. For synthetic zebrafish brain neurons, high-resolution image stack and neuron segmentation were acquired from Vladimirov N, et al. [2]. And following Cong, L, et al.[3], we randomly sampled a portion of neurons. From about 80,000 neurons we sampled 5%, 10%, 15% and 20%, which gave us n=3,585, 7,052, 10,565 and 21,358 number of neurons in our FOV. For real biological samples, we directly downloaded dataset for embryonic zebrafish vascular structure[4] and mouse brain neurons[5,6] and cropped/zero-padded it to fit our FOV. Next, for each SLIM sub-aperture PSF, the ground truth 3D image went through the corresponding rotation and vertical scaling. A depth-by-depth 2D convolution was performed between the transformed ground truth image and PSF. A depth-wise summation and adding Poisson noise gave the sub-aperture measurement. After repeating for every SLIM sub-aperture, the synthetic measurement was in form of a stack of sub-aperture images. We used Richardson-Lucy deconvolution for reconstruction.

1.Sample sparsity and reconstruction quality

SLIM is a compressive detection strategy for light field microscopy and its successful reconstruction relies on the sparseness of the sample, which we assume applies to a wide range of high-speed biological dynamics. As shown in **Supplementary Note 3 Fig. 1**, SLIM's performance can approximate FLFM when neurons are sparsely distributed (n=3,585, 7,052). However, it will degrade with higher density (e.g. n=21,358) and reconstructed neurons can no longer be clearly separated as density continues to increase. It's worth noting that SLIM holds up well in the sparseness settings used in FLFM literatures, where only 10% of neurons are assumed to be active at a given time[3,7].

A similar trend is expected when dealing with real sample datasets. From **Supplementary Note 3 Fig. 2**, SLIM shows comparable spatial resolution to FLFM on sparse zebrafish vasculature and mouse neurons. However, as shown in 5th row, when sample density and structural complexity increase substantially, SLIM's reconstruction quality begins to degrade. We note that SLIM is not intended for high-resolution structural imaging of highly complex samples, but these simulations underscore its robustness in scenarios where spatiotemporal sparsity is present.

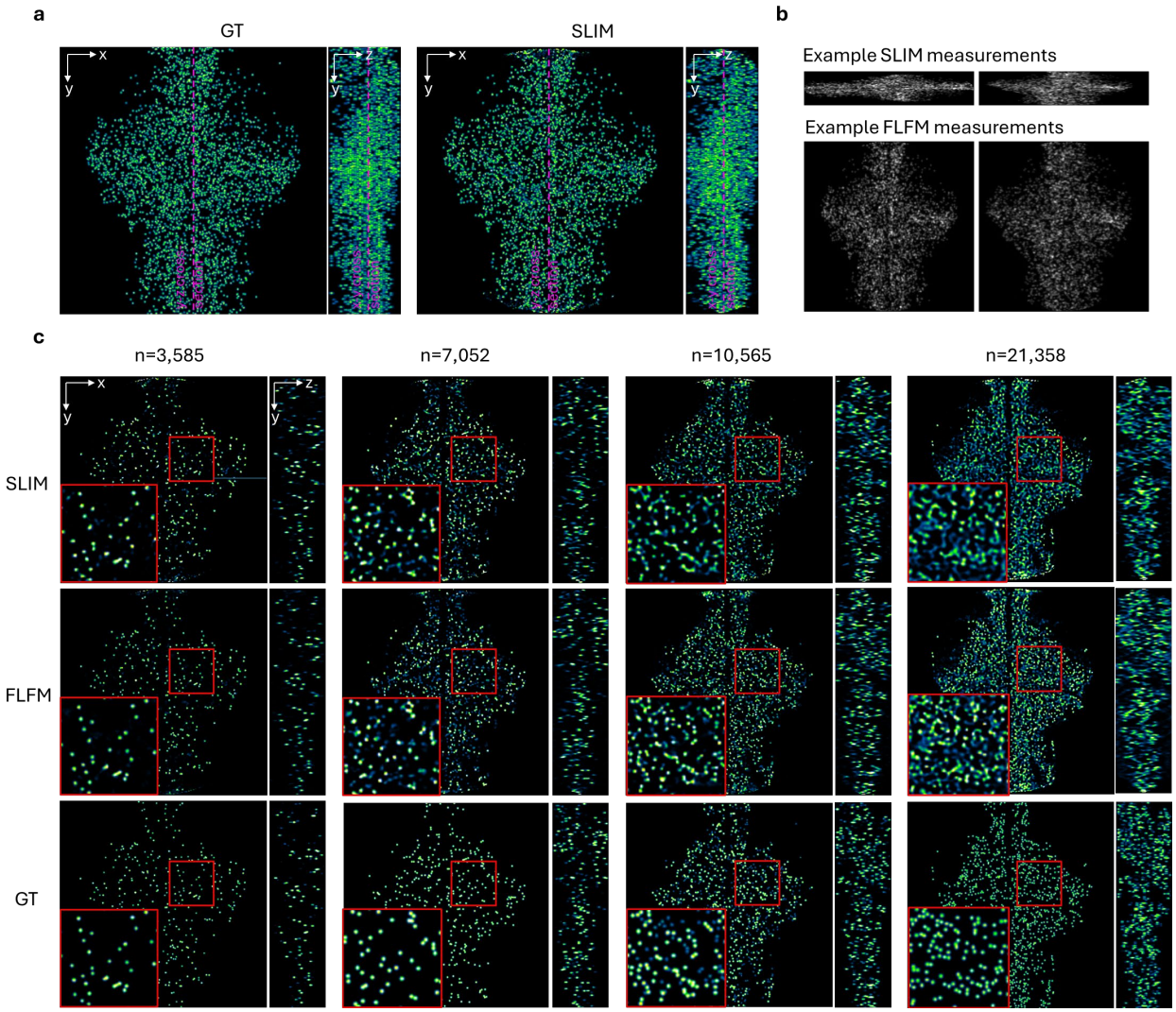

Supplementary Note 3 Fig. 1. Simulation results of synthetic neurons in zebrafish with different density of neurons. a. 3D MIP of synthetic neurons (GT) and corresponding SLIM reconstruction. **b.** Synthesized measurements of SLIM (top) and FLFM (bottom). Simulation adds Poison noise. **c.** Comparison between SLIM and FLFM reconstruction results with different density of neurons. Cross-sectioning slices are sampled at the position indicated by purple dotted line in **a**. From left to right, the ratio of randomly sampled neurons (83,890 in total) increases from 5%, 10%, 15% to 20%. The corresponding neuron number in our FOV is 3,585, 7,052, 10,565 and 21,358. The red box provides the zoom in view.

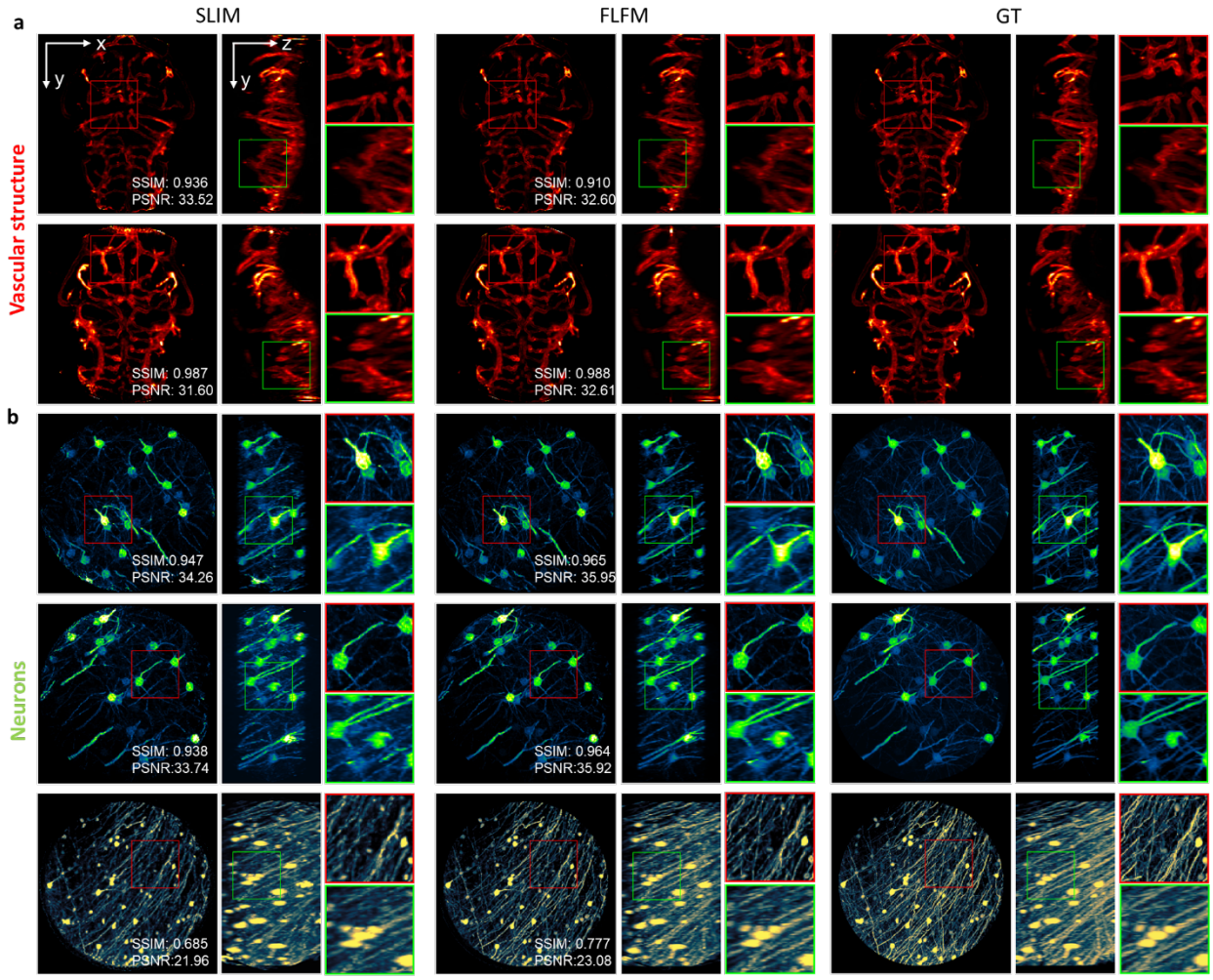

Supplementary Note 3 Fig. 2. Comparisons of image quality between SLIM and FLFM in real biological sample simulations. a.3D Maximum intensity projection (MIP) of the vascular structure in the brain of a transgenic zebrafish, *Tg(kdrl:HRAS-mCherry)*. **b.** 3D MIP of *Thy1-eGFP* (1st and 2nd rows) and *Thy1-eYFP* (3rd row) mouse neurons. The red (green) box highlights a zoomed-in view of the x-y (y-z) plane. Simulation adds Poisson noise to raw measurements. Sample sparseness is chosen to increase from top to bottom. Image reconstruction quality for SLIM and FLFM was compared across these samples using PSNR (Peak Signal-to-Noise Ratio) and SSIM (Structural Similarity Index Measure) as evaluation metrics.

2.**Number of sub-apertures and vertical scaling ratio**

In FLFM, the number of sub-apertures is associated with first-order parameters such as the NA of each sub-aperture, the FOV, the fill factor of the lenslet array (light efficiency), etc. In addition to these parameters, it determines the illness of reconstruction in SLIM, since fewer sub-aperture images make a higher compression ratio. Meanwhile, the vertical scaling ratio is defined by the demagnification of anamorphic relay. A smaller ratio allows a smaller sensor ROI and higher framerate but imposes higher vulnerability to noise and signal complexity.

The simulation in **Supplementary Note 3 Fig. 3** performs various scaling ratios with fixed number of sub-apertures (29). The ratio ranged from 0.04 to 1 and we tested on real zebrafish vascular

structures and mouse brain neuron datasets. As the scaling ratio was reduced to extremely low values (e.g., 0.04 or 0.1), SLIM can still reconstruct signals across the entire FOV, but we observed image degradation, including increased artifacts and loss of fine details.

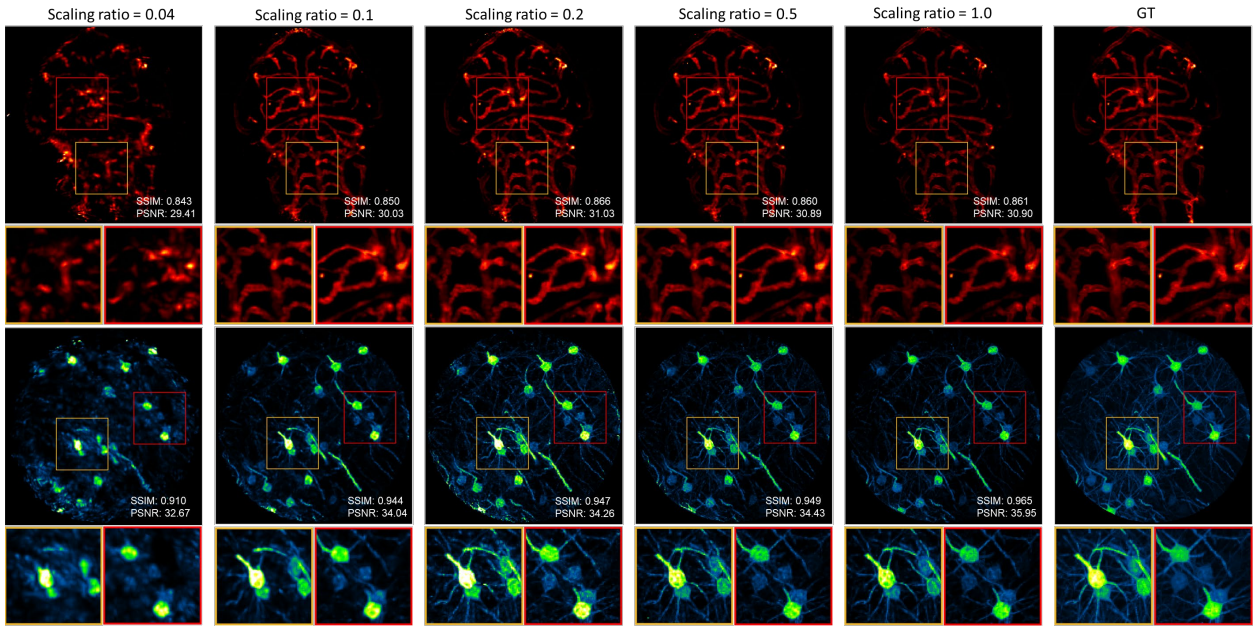

Supplementary Note 3 Fig. 3. Comparisons of image quality of SLIM under different scaling ratio configurations. Simulation adds Poisson noise. x-y MIPs are shown with zoom-in regions in red and yellow boxes. The reconstruction quality of SLIM and FLFM across different samples was compared using PSNR (Peak Signal-to-Noise Ratio) and SSIM (Structural Similarity Index Measure) as evaluation metrics.

Similarly, we controlled the number of sub-apertures (7, 19 and 29) but fixed the scaling ratio to 0.2. Simulations were performed on real zebrafish vascular structures and mouse brain neuron datasets (**Supplementary Note 3 Fig. 4**). As the number of sub-apertures decreased, we observed a degradation in image quality, manifesting as increased artifacts and a loss of detail. This decline occurs because fewer pixels are available for reconstruction, making the inverse problem more ill-posed. Here we changed the number of sub-apertures without adjusting lenslet size accordingly. Therefore, fewer sub-apertures also reduce light efficiency, compounding the negative effects on image quality.

Both the number of aperture and scaling ratio simulations reflect the inherent trade-off in the SLIM system. We experimentally demonstrated a scaling ratio of 0.2 and 29 apertures, enables kilohertz volumetric rate while maintaining reasonable robustness in various biological applications. However, the optimal SLIM configuration should consider specific sample structure, the targeted optical performance and framerate.

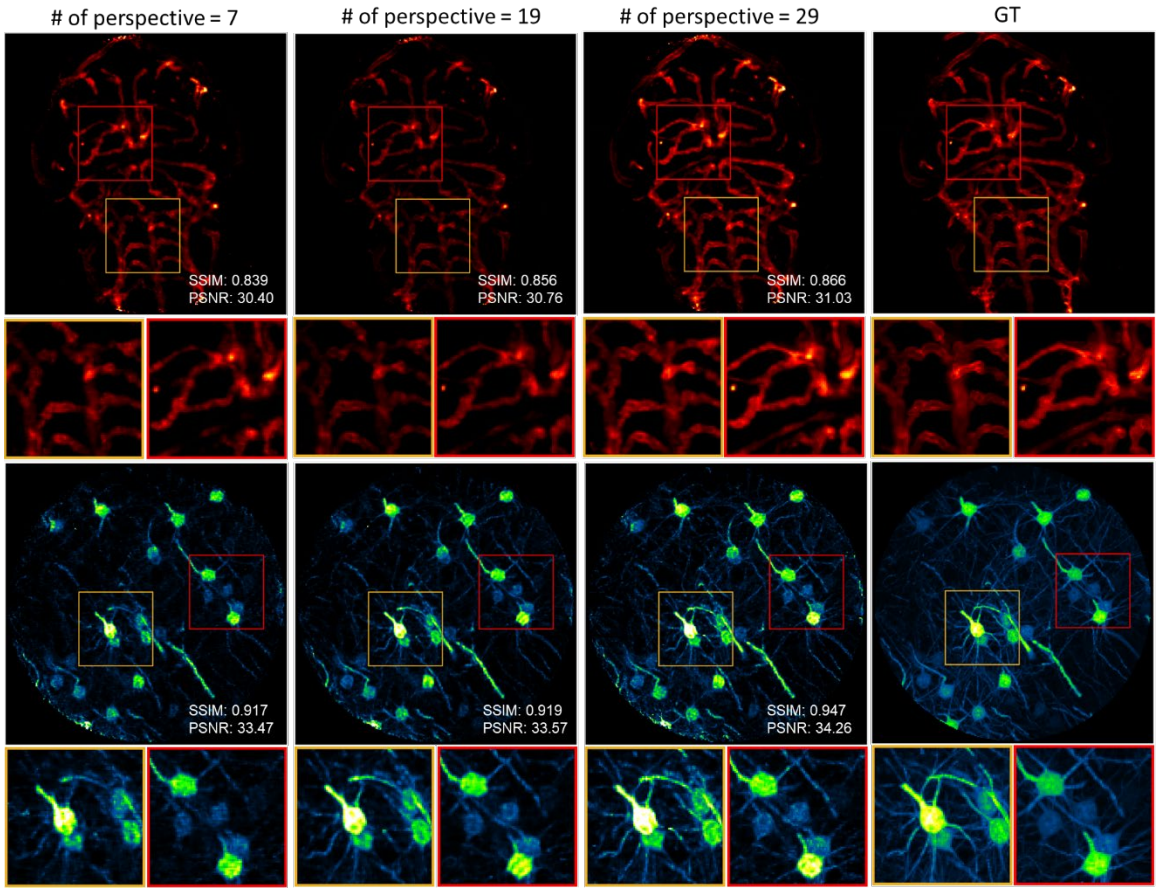

Supplementary Note 3 Fig. 4. Comparisons of image quality of SLIM under different numbers of sub-apertures configurations. Simulations add Poisson noise. x-y MIPs are shown with zoom-in regions in red and yellow boxes. The reconstruction quality of SLIM under different numbers of sub-apertures was compared using PSNR (Peak Signal-to-Noise Ratio) and SSIM (Structural Similarity Index Measure) as evaluation metrics.

Supplementary Note 4 Imaging and Analysis of Free-Swimming Vibrio cholerae

Overview of Imaging Challenges

Bacterial chemotaxis is a behavior in which cells sense and respond to chemical gradients in order to swim using their flagellar appendages towards favorable chemoattractants and avoid harmful substances.[17,18] Chemotaxis and flagellar swimming motility are important components of virulence pathways and bacterial pathogenicity.[19] Fully capturing this behavior in 3D, however, is difficult due to the high swimming speeds of the cells and the 3D nature of their trajectories. The current standard for imaging bacterial swimming involves a computational approach by matching diffraction patterns in a 2D image to a reference library in order to reconstruct the 3D positional information of the cell for tracking.[20] A major limitation of this technique is the imaging rate, which is typically around 10-30 Hz. For a swimming bacterium (*Vibrio cholerae* average swim speeds are around 100 μm/s), this imaging rate will result in about 5-10 μm of displacement between sequential images. Since this displacement is several cell body lengths long, much of the detailed behavior will not be captured.

Enhanced Imaging Using SLIM

To demonstrate SLIM's capability in addressing this challenge, we imaged the dynamic behaviors of swimming *Vibrio cholerae*. Our setup involved capturing 29 sub-aperture images at a rate of 200 frames per second, facilitated by light-sheet-synthesized volumetric illumination (**Supplementary Note 4 Fig. 1a**). This allows us to track each individual bacterium within imaging space simultaneously (**Supplementary Note 4 Fig. 1b**) and obtain information about its swimming trajectory (**Supplementary Note 4 Fig. 1c**) by MIP throughout all frames. This higher imaging volume rate reduces the spatial displacement in a cell's trajectory between sequential images allowing for observation of finer details in swimming behaviors, such as reversal events occurring during the "run-reverse-flick" behavior in *Vibrio cholerae* (first picture of **Supplementary Note 4 Fig. 1d,** also shown in **Supplementary Videos 6**), where a change in flagellar rotation direction causes a buckling of the hook protein and subsequent reorientation of the swimming direction out of the conventional 2D plane of imaging.[21] The high volumetric imaging speed also allows us to quantify the diffusivity of swimming cells by calculating the Mean Squared Displacement (MSD) slope and Radius of Gyration of their trajectories, as labeled in **Supplementary Note 4 Fig. 1d**[22], a task that is typically challenging with conventional 3D microscopy techniques.

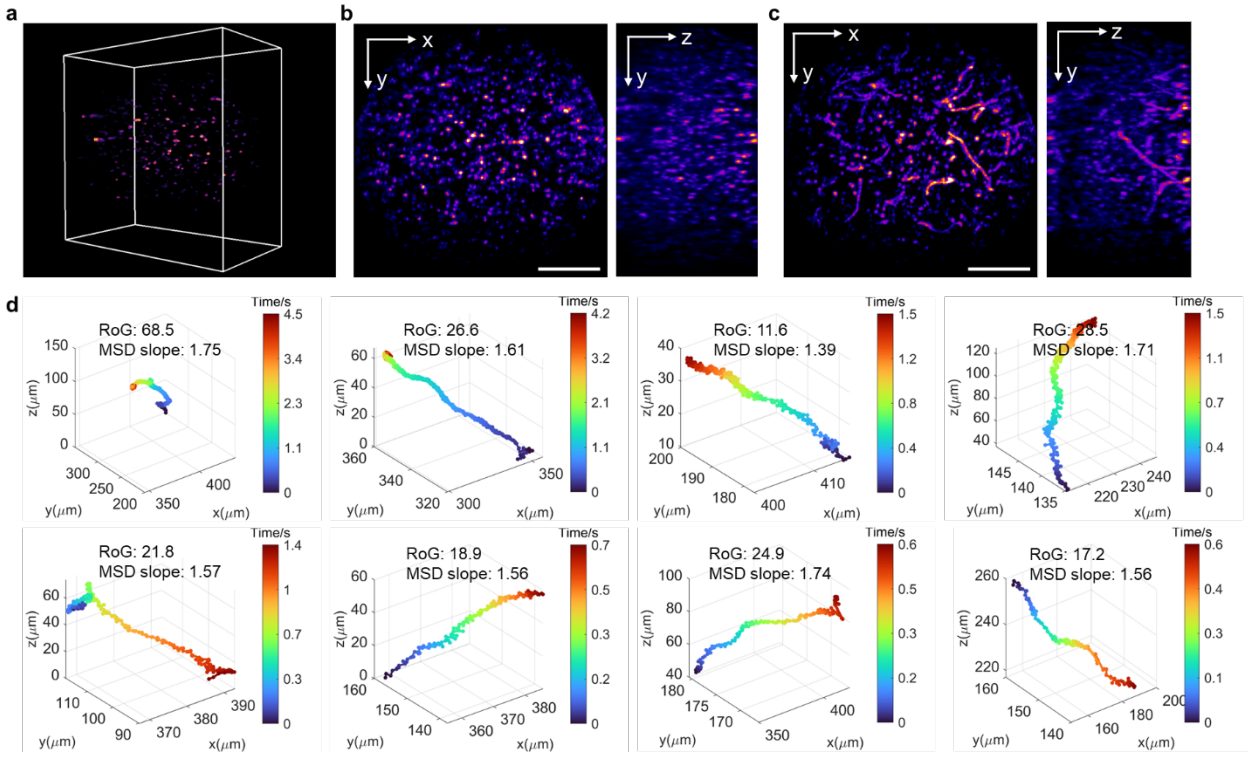

Supplementary Note 4 Fig. 1. 3D imaging of free-swimming *Vibrio cholerae* bacteria at 200 vps. a. 3D rendering volume of *Vibrio cholerae* bacteria. **b.** MIP from x-y and y-z slices of *Vibrio cholerae* bacteria. *Vibrio cholerae* are stained with an external membrane stain. The total recording time was 5s. **c.** MIPs of the swimming bacteria trajectory obtained by combining frames over time. **d.** Representative trajectories of swimming bacteria with their respective Radius of Gyration (RoG) and Mean Squared Displacement (MSD) slope measurements labeled. Scale bar, 120 μm.

Vibrio cholerae strain and preparation conditions

Wild Type Vibrio cholerae O1 El Tor strain A1552 were grown in lysogeny broth (LB) at 30°C with 200rpm shaking for 22 hours to stationary phase. Cell cultures were then diluted 1:1000 in 1mL of 2% LB media pre-mixed with 0.1ug/mL FM1-43FX membrane stain (Life Technologies F35355). 50uL of the stained cell culture was then loaded into a transparent FEP tube and sealed for imaging.

Quantitative Analysis of Swimming Metrics

Cell trajectories were analyzed for their Radius of Gyration (RoG) and Mean Squared Displacement (MSD) slope parameters. The Radius of Gyration(RoG) quantifies the average movement of a trajectory over time which is defined as: $RoG = \sqrt{\sum_{k=1}^{N} |r_k - r_{mean}|^2 / N}$, where r_k is the k^{th} position of the cell, r_{mean} is the mean position and N is the total number of tracking point. The MSD slope is a commonly used metric in colloidal studies and biophysics to determine the mode of displacement of particles followed over time. Actively swimming cells will have an MSD slope value in the super-diffusive regime (MSD slope > 1.4) while non-swimming cells will exhibit diffusive or sub-diffusive behavior (MSD slope ≤ 1). We used Msdanalyzer[23] for MSD slope calculation for all trajectories (https://github.com/tinevez/msdanalyzer).

Supplementary Table 1. Degraded performance in ultra-fast cameras/camera modes

Camera	Quantum efficiency	Readout noise(e^-)	Full well capacity(e^-)	Bitdepth (bit)	Frame format (px)	FPS	On-board RAM (Max. recording time)
Hamamatsu ORCA Flash4.0 V3	82%	1.6	30000	16	2048×2048	100	
Teledyne Kinetix (Dynamic range mode)	**96%**	**1.6**	**15000**	16	3200×3200	83	
Teledyne Kinetix (Speed mode)	96%	2.0	200	8	3200×3200	500	
Lambert HiCAM Fluo 2000[8,9]	50%	24		8	1920×1080	2,000	
Gpixel GSPRINT4502 (cropped FOV)[9]	60%	7	7400	10	1280×512	3,900	
Phantom TMX 7510	77.6%	24.18	8736	12	1280×800	76,000	512 GB (4.4s)

Supplementary Table 2. Space-bandwidth product (SBP) and volume rate of representative 3D microscopes

	Method	FOV(μm)	Resolution (x,y,z, μm)	Measurement (px)	Volume rate (vps)	SBP×volume rate*	Detector	Voltage imaging
Compressive Fourier light field microscopy	**SLIM (this work)**	Ø550×300	3.6×3.6×6	3200×200	1000**	**7.3×10^9**	Teledyne Kinetix (16-bit dynamic range mode), sCMOS	Leech ganglion ex *vivo*, Mouse brain *in vivo*
	Fourier DiffuserScope[10]	1000×1000 ×280	3×3×4	4.2×10^6	25	1.56×10^9	Andor Zyla 4.2, sCMOS	N.A.
	Miniscope-3D[11]	900×700 ×390	2.76×2.76 ×15	0.3×10^6	40	6.88×10^8	Ximea MU9PM-MH, CMOS	N.A.
Event camera	**Event LFM**[12]	130×130 ×200	3.9×3.9×21	1280×720	1000	8.5×10^7	EVK4, Prophesee, IMX636 sensor, Event Camera	N.A.
Deep learning enhancement	**Virtual Scanning LFM**[13]	210×210×18	0.23×0.23 ×0.42	2048×2048	12 (63×/1.4 Oil)	3.43×10^9	Andor Zyla 4.2 Plus PCIE, sCMOS	N.A.
		260×260 ×100		2000×2000	500 (25×/1.05 Water)		Teledyne Kinetix (8-bit speed mode), sCMOS	*Drosophila* brain, *in vivo*
Multiple cameras	**CALM**[14]	2650×2650 ×300	7.68×7.68 ×8.8	25×1024×768	30	9.74×10^8	***25×PointGray Flea2-08S2C-C RGB, CMOS	N.A.
	Wang et al.[9]	930×370 ×170	1.46×1.46 ×11.7	2×1280×256×30	200.8	3.77×10^9	***2×Gpixel GSPRINT4521/10/02	Zebrafish brain *in vivo*
Multi-plane scanning	**MuZIC**[15]	150×150×45 (4 planes)	2.6×1.9×12 (interplane spacing)		916	6.68×10^7	Hamamatsu S14420-1550MG (SiPM)	Mouse brain *ex vivo* and *in vivo*
Axially swept light sheet	**SIFT**[16]	4200 ×3300×5500	0.97×0.97 ×0.97		5.63×10^{-5} (4.93h acquisition time)	3.76×10^7	Hamamatsu Orca Flash 4.0, sCMOS	N.A.

*SBP is defined by $SBP = FOV/(d_x d_y d_z) * 8$, where FOV is three-dimensional, d is the spatial resolution, 8 accounts for the Nyquist sampling theorem. This definition refers to Lin et al.[14]

**The camera supports 1326 vps in 16-bit and 7476 vps in 8-bit. We only experimentally demonstrated 1000 vps in 16-bit and 4800 vps in 8-bit in accommodation to sample signal SNR.

***The number of detectors in the array.

Supplementary Table 3. List of components used in SLIM

		Component	Description	Manufacturer	Part number	Material
Selective volume illumination setup	SLIM	O1	20X Olympus XLUMPLFLN Objective, 1.00 NA	Olympus	N20X-PFH	
		L1	180 mm focal length achromatic doublet	Thorlabs	AC508-180-A	
		L2	200 mm focal length achromatic doublet	Thorlabs	AC508-200-A	
		L3	250 mm focal length achromatic doublet	Thorlabs	ACT508-250-A	
		CL1	250 mm focal length cylindrical achromatic doublet	Thorlabs	ACY254-250-A	
		CL2	50 mm focal length cylindrical achromatic doublet	Thorlabs	ACY254-50-A	
		Dove prism	1.3mm aperture size customized dove prism	Changchun Sunday Optics		H-K9L glass
		Dove prism holder	Customized 3D printing holder	Protolabs		Accura 7820 3D Printing Material
		MLA	36 mm focal length plano-convex lenslet array	fabricated in-house		PMMA
		Camera	sCMOS camera	Teledyne	Kinetix	
		F1(GFP)	525nm center wavelength bandpass filter	Chroma	ET525/50m	
		F1(RFP)	585nm center wavelength bandpass filter	Chroma	ET585/65m	
	Dual Scanning light sheet	473nm laser	500mW 473nm diode laser	CNI laser	MBL-FN-473-500mW	
		532nm laser	300mW 532nm diode laser	CNI laser	MGL-III-532-300mW	
		Beam splitter	50:50 Non-Polarizing Beamsplitter Cube	Thorlabs	BS013	
		CL3	50 mm focal length cylindrical lens	Thorlabs	LJ1695RM-A	
		CL4	50 mm focal length cylindrical lens	Thorlabs	LJ1695RM-A	
		Knife-edge mirror	Knife-edge right-angle prism	Thorlabs	MRAK25-G01	
		L4	150 mm focal length achromatic doublet	Thorlabs	AC254-150-A	
		Galvo mirror	single axis scanning Galvo mirror	Thorlabs	GVS011	
		L5	150 mm focal length achromatic doublet	Thorlabs	AC508-150-A	
		L6	180 mm focal length achromatic doublet	Thorlabs	AC508-150-A	
		O2	4X Olympus Plan Fluorite Objective, 0.13 NA	Olympus	RMS4X-PF	
	LED	Blue LED	ultra-low-noise blue LED	Prizmatix	UHP-T-470SR	
		Excitation filter	470nm center wavelength bandpass filter	Chroma	ET470/40X	
		L7	50 mm focal length achromatic doublet	Thorlabs	AC254-050-A	
		Slit	adjustable mechanical slit	Thorlabs	VA100	
		L8	80 mm focal length achromatic doublet	Thorlabs	AC508-080-A	
		O2	4X Olympus Plan Fluorite Objective, 0.13 NA	Olympus	RMS4X-PF	
Widefield illumination setup	SLIM	O3	16X Nikon CFI LWD Plan Fluorite Objective, 0.80 NA	Nikon	N16XLWD-PF	
		L9	150 mm focal length achromatic doublet	Thorlabs	AC508-150-A	
		L10	150 mm focal length achromatic doublet	Thorlabs	AC508-150-A	
		L11	250 mm focal length achromatic doublet	Thorlabs	ACT508-250-A	
		CL5	250 mm focal length cylindrical achromatic doublet	Thorlabs	ACY254-250-A	
		CL6	50 mm focal length cylindrical achromatic doublet	Thorlabs	ACY254-50-A	
		Dove prism	1.3mm aperture size customized dove prism	Changchun Sunday Optics		H-K9L glass
		Dove prism holder	Customized 3D printing holder	Protolabs		Accura 7820 3D Printing Material
		MLA	36 mm focal length plano-convex lenslet array	fabricated in-house		PMMA
		Camera	sCMOS camera	Teledyne	Kinetix	
		F2	525nm center wavelength bandpass filter	Chroma	ET525/50m	
	LED	Blue LED	Ultra-low-noise blue LED	Prizmatix	UHP-T-470SR	
		F3	470nm center wavelength bandpass filter	Chroma	ET470/40X	
		F4	GFP Dichroic Filter	Thorlabs	MD498	
		L12	150 mm focal length achromatic doublet	Thorlabs	AC254-150-A	

Supplementary Table 4. Acquisition parameters for imaging experiments

	Figure Number	Sample	Illumination Source	Galvo Mirror Frequency (Hz)	Sensor ROI Size (px)	Sensor Readout Mode	Sensor Exposure Time (μs)	Sensor Frame Rate (fps)	Volume Rate (vps)	Recording Time (s)	Number of sub-apertures	Reconstruction Resolution (px)	Reconstruction Pixel Size (μm)	FOV(μm)	Illumination Power (mW/mm2)
Selective volume illumination setup	Fig. 1e,f	Fluorescent beads (F13081, ThermoFisher)	LED (470 nm)	Not applicable	320×3200	16-bit (Dynamic range mode)	100000	Not applicable	Not applicable	Not applicable	29	305×305×101	1.81×1.81×4	Ø550×400	
	Fig. 2a-c	Embryonic zebrafish *Tg(gata1a:dsRed)* @ 3dpf	Scanning light sheet (532 nm)	1000	200×3200	16-bit (Dynamic range mode)	990	1000	1000	4	19	305×305×51	1.81×1.81×6.16	Ø550×308	
	Fig. 2d-e	Embryonic zebrafish *Tg(gata1a:dsRed)* @ 3dpf	Scanning light sheet (532 nm)	1000	200×3200	16-bit (Dynamic range mode)	990	1000	1000	4	19	305×305×151	1.81×1.81×4	Ø550×600	
	Fig. 3c,f, S10, S11	Medicinal leech	LED (470 nm)	Not applicable	320×3200	16-bit (Dynamic range mode)	1200	800	800	12	29	295×295×76	1.81×1.81×4	Ø532×300	
	Fig. 5b	Fluorescent beads (F13082, ThermoFisher)	Scanning dual-light sheet (532 nm)	100	320×3200	8-bit (Speed mode)	240	4000	100	Not applicable	29	295×295×78	1.81×1.81×3.9	Ø532×300	
	Fig. 5c	Embryonic zebrafish *Tg* (fli1:nCherry) @ 3dpf	Scanning dual-light sheet (532 nm)	100	320×3200	8-bit (Speed mode)	240	4000	100	3	29	295×295×78	1.81×1.81×3.9	Ø532×300	
	Fig. 5d,e,f	Embryonic zebrafish *Tg* (cmlc:GFP) @ 3dpf	Scanning dual-light sheet (473 nm)	300	200×3200	8-bit (Speed mode)	200	4800	300	3	19	150×150×30	1.81×1.81×6	Ø270×174	
	SI Note 4 Fig. 1	Vibrio cholerae bacteria	Scanning light sheet (473nm)	200	320×3200	16-bit (Dynamic range mode)	4800	200	200	5	29	295×295×76	1.81×1.81×4	Ø532×300	
Widefield illumination setup	Fig. 4, Ext. Fig. 2, Fig. S13, S14	Wild type mice with genetically encoded voltage indicator (GEVI) pAce (interneurons)	LED (470 nm)	Not applicable	330×2400	16-bit (Dynamic range mode)	1230	800	800	180	29	305×305×75	2.26×2.26×8	Ø686×592	40
	Fig. S15, S16	Wild type mice with genetically encoded voltage indicator (GEVI) pAce (interneurons)	LED (470 nm)	Not applicable	330×2400	16-bit (Dynamic range mode)	1230	800	800	180	29	305×305×75	2.26×2.26×8	Ø686×592	36
	Ext. Fig 1	Wild type mice with genetically encoded voltage indicator (GEVI) pAce (pyramidal neurons)	LED (470 nm)	Not applicable	330×2400	16-bit (Dynamic range mode)	1230	800	800	180	29	305×305×75	2.26×2.26×8	Ø686×592	25
	Fig. S12	Fluorescent beads (F13081, ThermoFisher)	LED (470 nm)	Not applicable	330×2400	16-bit (Dynamic range mode)	1230	Not applicable	Not applicable	Not applicable	29	305×305×151	2.26×2.26×8	Ø686×1200	

References

1. Guo, C. *et al.* Fourier light-field microscopy. *Opt. Express, OE* **27**, 25573–25594 (2019).
2. Vladimirov, N. *et al.* Light-sheet functional imaging in fictively behaving zebrafish. *Nat Methods* **11**, 883–884 (2014).
3. Cong, L. *et al.* Rapid whole brain imaging of neural activity in freely behaving larval zebrafish (Danio rerio). *eLife* **6**, e28158 (2017).
4. Kugler, E. C. *et al.* Zebrafish vascular quantification: a tool for quantification of three-dimensional zebrafish cerebrovascular architecture by automated image analysis. *Development* **149**, dev199720 (2022).
5. Dean, K. M. *et al.* Isotropic Imaging Across Spatial Scales with Axially Swept Light-Sheet Microscopy. *Nat Protoc* **17**, 2025–2053 (2022).
6. Park, H. *et al.* Deep learning enables reference-free isotropic super-resolution for volumetric fluorescence microscopy. *Nat Commun* **13**, 3297 (2022).
7. Yoon, Y.-G. *et al.* Sparse decomposition light-field microscopy for high speed imaging of neuronal activity. *Optica, OPTICA* **7**, 1457–1468 (2020).
8. Mandracchia, B. *et al.* High-speed optical imaging with sCMOS pixel reassignment. *Nat Commun* **15**, 4598 (2024).
9. Wang, Z. *et al.* Imaging the voltage of neurons distributed across entire brains of larval zebrafish. 2023.12.15.571964 Preprint at https://doi.org/10.1101/2023.12.15.571964 (2023).
10. Liu, F. L., Kuo, G., Antipa, N., Yanny, K. & Waller, L. Fourier DiffuserScope: single-shot 3D Fourier light field microscopy with a diffuser. *Opt. Express, OE* **28**, 28969–28986 (2020).

11. Yanny, K. *et al.* Miniscope3D: optimized single-shot miniature 3D fluorescence microscopy. *Light Sci Appl* **9**, 171 (2020).
12. Guo, R. *et al.* EventLFM: event camera integrated Fourier light field microscopy for ultrafast 3D imaging. *Light Sci Appl* **13**, 144 (2024).
13. Lu, Z. *et al.* Virtual-scanning light-field microscopy for robust snapshot high-resolution volumetric imaging. *Nat Methods* **20**, 735–746 (2023).
14. Lin, X., Wu, J., Zheng, G. & Dai, Q. Camera array based light field microscopy. *Biomed. Opt. Express, BOE* **6**, 3179–3189 (2015).
15. Weber, T. D., Moya, M. V., Kılıç, K., Mertz, J. & Economo, M. N. High-speed multiplane confocal microscopy for voltage imaging in densely labeled neuronal populations. *Nat Neurosci* **26**, 1642–1650 (2023).
16. Prince, M. N. H. *et al.* Signal improved ultra-fast light-sheet microscope for large tissue imaging. *Commun Eng* **3**, 1–13 (2024).
17. Berg, H. C. Chemotaxis in Bacteria. Annual Review of Biophysics 4, 119–136 (1975).
18. Keegstra, J. M., Carrara, F. & Stocker, R. The ecological roles of bacterial chemotaxis. Nat Rev Microbiol 20, 491–504 (2022).
19. Butler, S. M. & Camilli, A. Going against the grain: chemotaxis and infection in Vibrio cholerae. Nat Rev Microbiol 3, 611–620 (2005).
20. Grognot, M., Mittal, A., Mah'moud, M. & Taute, K. M. Vibrio cholerae Motility in Aquatic and Mucus-Mimicking Environments. Applied and Environmental Microbiology 87, e01293- 21 (2021).
21. Son, K., Guasto, J. S. & Stocker, R. Bacteria can exploit a flagellar buckling instability to change direction. Nature Phys 9, 494–498 (2013).

22. Conrad, J. C. et al. Flagella and Pili-Mediated Near-Surface Single-Cell Motility Mechanisms in P. aeruginosa. Biophysical Journal 100, 1608–1616 (2011).

23. Tarantino, N. et al. TNF and IL-1 exhibit distinct ubiquitin requirements for inducing NEMO–IKK supramolecular structures. Journal of Cell Biology 204, 231–245 (2014).